Vertical Planar Liquid-Vapour Thermal Diodes (PLVTD) and their application in building façade energy systems

Adrian Pugsley (a.pugsley@ulster.ac.uk, +44(0)28 90366264 (corresponding author)
Aggelos Zacharopoulos (a.zacharopoulos@ulster.ac.uk) +44(0)28 90368227
Jayanta Deb Mondol (jd.mondol@ulster.ac.uk) +44(0)28 90368037
Mervyn Smyth (m.smyth1@ulster.ac.uk) +44(0)28 90368119

Centre for Sustainable Technologies (www.cst.ulster.ac.uk), School of the Built Environment, Ulster University, Newtownabbey, BT37 0QB, Northern Ireland, UK

Keywords

Thermal diode; one-way heat transfer; switchable insulation; net zero energy buildings; building facade; solar collector;

Highlights

- Vertical planar thermal diodes realised & tested at realistic scales (0.15 & 0.98m^2)
- Reverse mode insulation (1.7<U_r<12 W·m^{-2}K^{-1}) depends primarily on depth (22<x<70mm)
- Forward mode heat transfer depends on temperature & heat flux (50<U_f<900 W·m^{-2}K^{-1})
- One-dimensional lumped parameter heat transfer model augmented & validated
- Applications in solar collectors and climate control building envelopes discussed

Abstract

Buildings represent one-third of global energy consumption and corresponding CO_2 emissions which can be reduced through enhanced insulation and building integrated renewables. Thermal diodes can potentially revolutionise passive heat collection/rejection devices such as Integrated Collector-Storage Solar Water Heaters (ICSSWH) and Climate-Control Building Envelopes (CCBE) employed for decarbonisation. We present novel theoretical and experimental validation work on a lumped parameter heat transfer model of Planar Liquid-Vapour Thermal Diodes (PLVTD) to support development of ICSSWH and CCBE components for building facades. This study augments our previous work on a passive horizontal PLVTD model, by introducing falling film evaporation, vapour convection in vertical rectangular enclosures, condensation on vertical plates, and a methodology for evaluating working fluid temperatures. Experimental validations are presented for vertical aluminium (A_p=0.15m^2, x=22mm) and stainless steel (A_p=0.98m^2, x=70mm) prototypes using two different laboratory test methodologies where temperature setpoints were controlled and measured. The model predicts measured steady state thermal conductances in reverse mode ($U_r \approx 12$ W·m^{-2}K^{-1} and $U_r \approx 1.7$W·m^{-2}K^{-1} for x=22mm and x=70mm PLVTDs respectively) and forward mode ($175<U_f<730$W·m^{-2}K^{-1} and $50<U_{LvL}<900$W·m^{-2}K^{-1} respectively) with reasonable accuracy across investigated ranges ($15<T_2<65$°C condenser temperatures, $5<-\Delta T_{12}<25$°C reverse mode plate-to-plate temperature differences, $50<q/A<1000$ W·m^{-2} forward mode heat fluxes). Forward mode behaviour is determined by working fluid vapour mass flow driven by heat flux and influenced by temperature dependent vapour viscosity. Reverse mode behaviour is determined by vapour convection, plate-to-plate radiation, and envelope/structure conduction. Parametric design influences are theoretically examined and $\varsigma>99\%$ diodicity relevant to CCBE and ICSSWH applications is demonstrated experimentally. Study findings contribute towards global efforts tackling the climate crisis by enabling commercial R&D for new Net Zero Energy Building components.

1 Introduction

1.1 Study context

Approximately one-third of global final energy consumption (125 of 400EJ annually) can be attributed to residential and service sector buildings (IEA, 2018; IEA/UN, 2018) where it is primarily used for space heating & cooling (40%) and domestic hot water production (20%). Buildings are correspondingly responsible for ~39% of global CO_2 emissions which need to be radically and rapidly cut in order to mitigate the climate crisis. Net-Zero Energy Building (NZEB) and Near-Zero Energy Building (nZEB) concepts aim to reduce CO_2 emissions by minimising thermal energy demands through measures such as Climate Control Building Envelopes (CCBE), Building Integrated PhotoVoltaics (BIPV), Building Integrated Solar Thermal Systems (BISTS) and other renewable energy technologies such as heat pumps. We introduce the concept of thermal diodes (Section 1.1) and discuss how they offer significant potential to improve the efficacy of CCBE, BIPV and BISTS components (Sections 1.2 and 1.3). The growing body of literature is briefly reviewed, including work undertaken by Ulster University Centre for Sustainable Technologies regarding Liquid-Vapour Thermal Diodes (LVTD) and their application in Integrated Collector-Storage Solar Water Heaters (ICSSWH). Sections 2 and 3 build directly upon the theoretical and experimental work of Pugsley et al. (2019) by augmenting the proposed model of PLVTD behaviour and providing new validating experimental data for vertically oriented devices. The original work considered a simple PLVTD with a passively wetted evaporator which restricted operation to the horizontal orientation only, whereas the present study examines a pumped falling film evaporator which enables operation in vertical and tilted orientations. Section 4 explores the parametric design of a PLVTD by using the model to examine the influence of temperatures, heat flux, dimensions, orientation and other factors upon its behaviour. Section 5 re-examines experimental data from tests on a large vertical falling film PLVTD incorporated into a flat ICSSWH prototype (Pugsley et al., 2016 & 2017; Smyth et al., 2019) to provide further validation of the proposed theoretical model and to identify areas for further research.

1.2 Thermal diodes

A thermal diode is a unidirectional heat transfer device that operates in a manner analogous to an electrical semiconductor diode by offering low resistance (thermal conductance) in one direction and high resistance (thermal insulation) in the other. Whilst there are many different mechanisms for realising thermal rectification (Go & Sen, 2010; Roberts & Walker, 2011; Boreyko & Chen et al., 2011 & 2013; Chen et al., 2012; Ben-Abdallah & Biehs, 2013; Dos Santos Bernardes, 2014; Bairi et al., 2014; Pei et al., 2017; Blet et al., 2017; Avanessian and Hwang, 2018; Traipattanakul et al., 2019; Wong et al., 2019) in a variety of different geometric forms and orientations, the present study is concerned with PLVTDs. These devices (see Figures 1 and 2) essentially consist of two parallel plates of area A=yz separated by a cavity of depth x which contains a quantity of working fluid maintained in a thermodynamic state close to saturation. During forward mode operation, wetting of the hottest plate (evaporator) through contact with the liquid working fluid generates vapour, which then migrates to the colder plate (condenser) where it releases its latent heat and generates condensate to complete the cycle. During reverse mode operation, the hottest plate is kept dry so that no vapour can be generated, no latent heat transfer occurs, and the partially evacuated cavity acts as an insulator. Forward mode evaporator wetting can be achieved by a variety of active (eg pumped falling film or spray) or passive (eg capillary wick or pockets) techniques. Careful control over plate wetting mechanisms could feasibly enable the operating direction of a thermal diode to be reversed or for forward mode operation to be initiated or supressed on demand, thereby creating components with switchable thermal insulation characteristics.

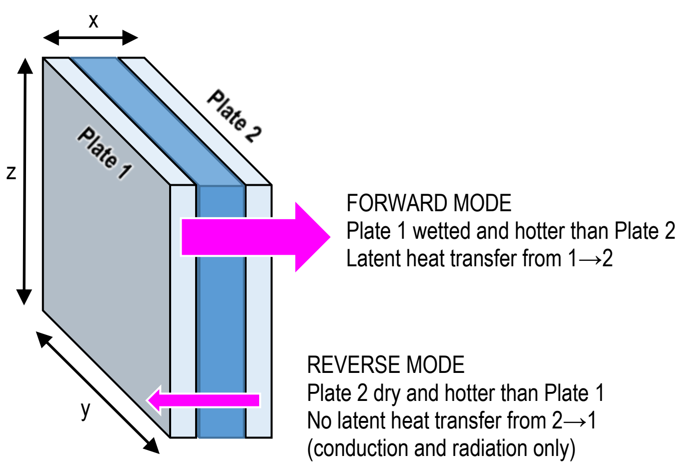

Figure 1 – Schematic diagram of a PLVTD

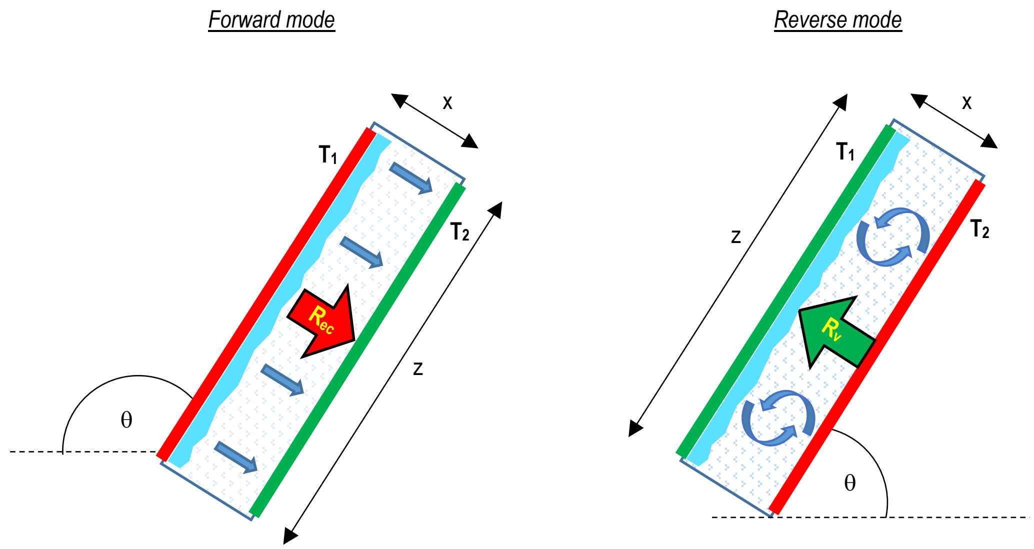

The wetted evaporator plate (T_1) generates vapour during forward mode operation when T_1>T_2 resulting in latent heat being transferred to the condenser plate (T_2) due to the mass flow of vapour induced by the saturation pressure differential. In reverse mode when T_2>T_1 there is no latent heat transfer because the hotter plate is kept dry (no vapour generation) but some degree of sensible heat transfer occurs owing to gaseous conduction and convection through the residual vapour.

The vapour mass transfer (R_{ec}) and vapour convection (R_v) thermal resistances are dependent upon the height (z) and characteristic dimension (L≈x) of the enclosure, the hot plate external tilt angle with respect to horizontal (θ), and the working fluid thermodynamic properties which are dependent upon plate temperatures T_1 and T_2.

Figure 2 – Arrangement and working principles of a PLVTD

1.3 Climate Control Building Envelopes

Climate Control Building Envelopes (CCBE) can massively reduce space heating & cooling energy demands and are an essential part of NZEBs (Ascione et al. 2016; Charisi, 2017; Li et al., 2019). In cold climates, a CCBE must be well-insulated to prevent fabric heat losses; use heat recovery ventilation to prevent airflow related heat losses; and should incorporate mechanisms to enable collection of solar and ambient heat. The latter can be achieved through either passive means such as Trombe walls or double-skin facades (Kilaire & Stacey, 2017; Hu et al., 2017; Yu et al., 2018; Inan & Basaran, 2019; Agathokleous et al., 2019) or by using active systems such as ground-source, air-source, or solar assisted heat pumps (Good et al., 2015; He et al., 2015; Buonomano et al., 2016; Aguilar et al., 2016; Calise et al., 2016; Poppi et al., 2016; Qu et al., 2016; Kilaire & Stacey, 2017). In hot climates, a CCBE must incorporate shading devices to prevent solar heat gains; have appropriate insulation and ventilation which prevents ambient heat gains (eg infiltration of hot outdoor air); and include design features which facilitate free-cooling during night-time periods. Thermal insulation in hot climate CCBEs can be important for preventing unwanted fabric heat gains but conversely acts as “anti-insulation” (Masoso & Grobler, 2008; Idris & Mae, 2017) owing to the inherent reduction in potential for passive heat rejection. Climates in many regions of the world are characterised by significant diurnal and seasonal temperature differences which necessitate thermally adaptive CCBEs that combine all the abovementioned features into a multifunctional façade and/or roofing system. In addition to reducing the amount of energy required for space heating and cooling, CCBEs are increasingly being designed with BIPV to generate electricity; BISTS to supply domestic hot water and additional heat for space heating; or Building Integrated PhotoVolatic-Thermal (BIPVT) elements which simultaneously produce both thermal and electrical energy. Thermal diodicity, dynamic insulation, adaptive insulation and switchable insulation concepts (Stazi et al., 2012; Kimber et al., 2014; Berge et al., 2015; Menyhart & Krarti, 2017; Jin et al. 2017; Koenders et al., 2018; Pflug et al., 2018; Rupp & Krarti, 2019; Cui & Overend, 2019) have significant potential to improve the efficacy of CCBEs in respect of their ability to collect solar and ambient heat in cold climates (Figure 3a); reject excess heat in hot climates (Figure 3b); and potentially improve the efficiency of BIPV elements by regulating cell temperatures. The use of thermal diodes in building façade elements has been proposed and investigated by a handful of authors (Kolodziej & Jaroszynski, 1997; Chen et al., 1998; Varga et al. 2002; Fang & Xia, 2010; Reay et al., 2014; Villeneuve et al., 2017) but the use of Planar Liquid-Vapour Thermal Diodes (PLVTDs) in CCBEs has yet to be described in detail anywhere in the literature. In Cui & Overend’s (2019) high level study examining possible mechanisms for achieving switchable insulation in thermally adaptive building envelopes they conclude that “*Among the five technologies reviewed,* *the most thermally efficient one, in terms of switching ratio and the range of controllable heat transfer . . . alternates its heat transfer mechanisms between highly conductive evaporation-condensation circulation to insulated single-phase gaseous conduction*" and that "*controllable flat-plate heat pipes are a promising direction*". These statements align perfectly with the PLVTD concept as described in Section 1.2 and provide strong justification for the present study.

1.4 Integrated Collector-Storage Solar Water Heaters

Solar thermal systems offer significant potential to contribute towards meeting both domestic hot water and space heating energy demands. When combined with sufficient energy storage, BISTS have been shown to provide between 10% and 90% of residential and commercial building space heating and domestic hot water energy demands in a variety of climates (Smyth et al., 2006; Li et al., 2013; Drosou et al., 2014; O'Hegarty et al., 2014; Good et al., 2015; Mehdaoui et al., 2019; Beausoleil-Morrison et al., 2019; Billardo et al., 2019). Solar water heating systems typically have three main components: the collector, the heat transfer system, and the storage vessel. Storage vessels in conventional pumped solar water heating systems tend to be bulky and consume valuable floor space. In hot climates, thermosiphonic solar water heaters with close-coupled storage tanks are popular owing to their passive operation, simple installation, externally located storage tank, and relatively low cost. Integrated Collector-Storage Solar Water Heaters (ICSSWH) are passive systems which combine the collector and storage vessel into one unit by using part of the storage tank envelope as a solar absorber (Smyth et al., 2006; Garnier et al., 2009; Borello et al., 2012; Ziapour et al., 2014; Singh et al., 2016; Billardo et al., 2019). This concept minimises system size and quantity of material required for manufacturing, leading to lower unit costs (Tripanagnostopoulos & Souliotis, 2006), less embodied energy, and greater space efficiency. The greatest drawback of ICSSWHs and close-coupled thermiosiphon solar water heaters is that a large area of storage vessel surface is inherently exposed to the outdoor environment and thus susceptible to heat loss in cold and windy climates. Several authors have explored the use of thermal diodes to control heat loss in thermosiphonic solar water heaters. In particular, Mohamad (1997), Faiman et al. (2001) and Sopian et al. (2004) realised thermal diodes by fitting one-way valves which allow water to flow from the hot solar collector outlet to a cooler storage vessel but prevent reverse flow when the collector is cooler than the store. Some authors (Smyth et al., 1999 and Rhee et al., 2010) incorporated thermal diodes in hot water storage vessels to promote stratification and reduce heat loss. A growing body of work on the use of liquid-vapour thermal diodes to reduce heat loss from ICSSWH collectors has developed in recent years (De Beijer, 1998; Quinlan, 2010; Souliotis et al., 2011&2017; Smyth et al., 2015a&b, 2017, 2018, 2019; Pugsley et al., 2016 & 2019; Pugsley, 2017; Muhumuza et al., 2019a & b). Smyth et al. (2017) designed, fabricated and tested cylindrical ICSSWHs featuring annular thermal diodes which minimised overnight heat loss to <1 $W{\cdot}m^{-2}K^{-1}$. Smyth et al. (2019) demonstrated that an uncovered ICSSWH featuring a vertically oriented PLVTD (see Figure 3c) can achieve a significantly better heat loss coefficient (5.4 $W{\cdot}m^{-2}K^{-1}$) during solar collection periods than an equivalent uncovered ICSSWH without a thermal diode (12.9 $W{\cdot}m^{-2}K^{-1}$).

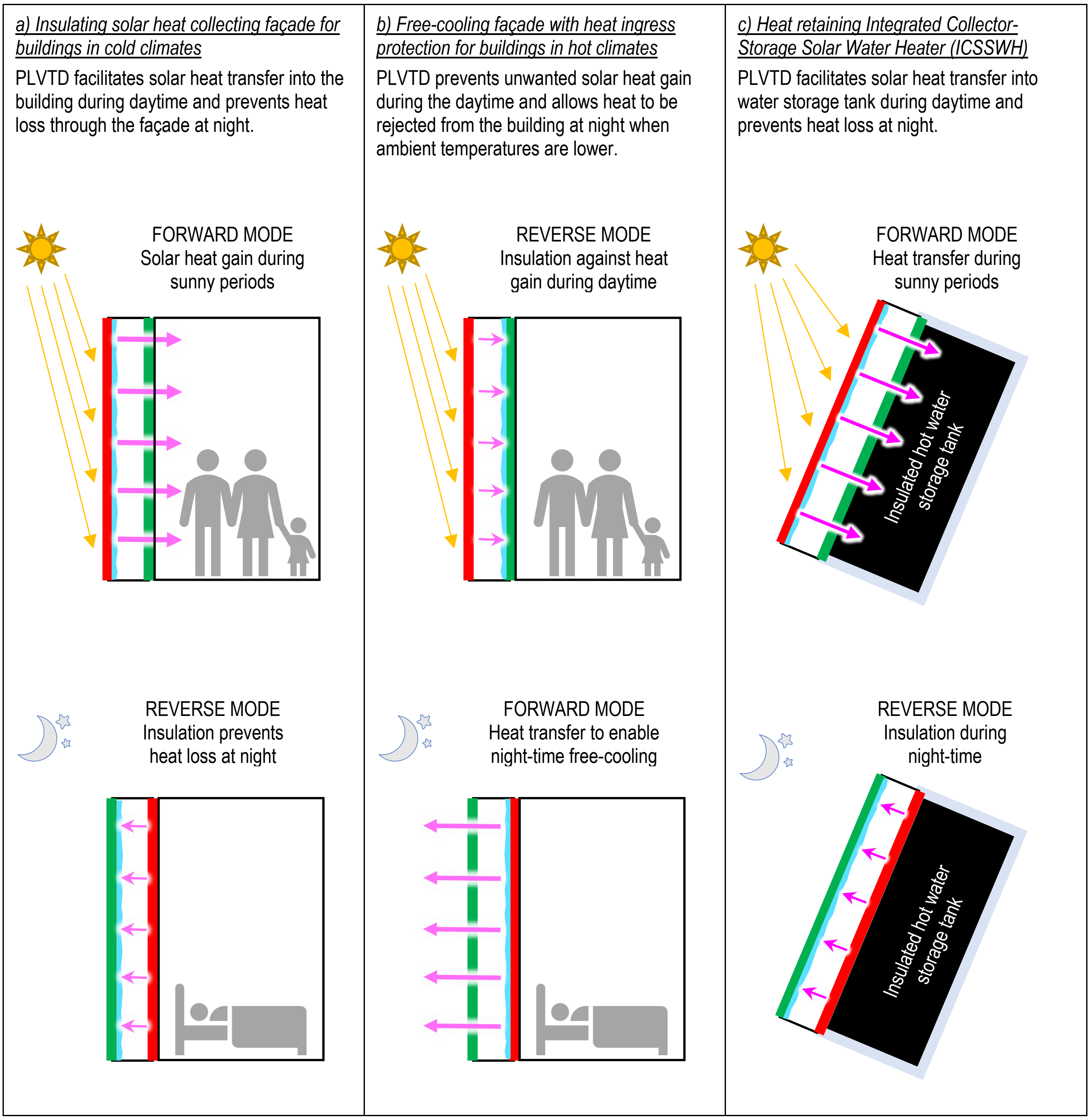

Figure 3 – Practical applications for PLVTDs in Climate Control Building Facades and Integrated Collector-Storage Solar Water Heaters

2 Theory

2.1 Heat flux, temperature and pressure

Heat transfer through a PLVTD is driven by the difference in temperature between the two plates ($\Delta T_{12} = |T_1 - T_2|$). The transferred thermal power (q_{12}), the transferred heat flux (q_{12}/A_p), overall thermal resistance (R_{fr}), and the overall thermal conductance (U_{fr}) through the PLVTD are related according to Equation 1 (Pugsley et al., 2019). Figure 4 shows the main heat transfer paths and corresponding thermal resistances through a PLVTD in both forward and reverse modes.

$$U_{fr} = \frac{q_{12}}{yz(T_1 - T_2)} = \frac{q_{12}}{A_p \Delta T_{12}} = \frac{1}{A_p R_{fr}} \qquad \text{Equation 1}$$

In forward mode, the dominant thermal transmission mechanism is latent heat transfer associated with working fluid liquid-vapour-liquid phase changes and the net transfer of working fluid vapour mass across the cavity between the two plates. In reverse mode, thermal transmission occurs via several different mechanisms including working fluid convection and gaseous conduction; radiation between the plates; and conduction through the external envelope and internal supporting structural elements.

In order to transfer heat in forward mode, the working fluid must exist in vapour phase at the evaporator temperature (T_1) and in liquid phase at the condenser temperature (T_2). If all non-condensable gases are removed, then the resulting pressure inside the PLVTD will be approximately equal to the saturation pressure (P_{Lv}) of the working fluid at the saturation temperature T_{Lv}. This internal pressure will usually be different from the atmospheric pressure outside necessitating internal structures to ensure that the PLVTD envelope can withstand the pressure differential.

2.2 Diodicity

Diodicity coefficient (ς) is a dimensionless measure of thermal rectification and is a useful performance measure for thermal diodes and switchable insulation devices. It is commonly defined according to Equation 2 as a scalar (between zero and unity) based on the performance of the device in forward (f) heat transfer mode and reverse (r) insulation mode. For convenience, we have chosen to express heat transfer and insulation performances in terms of thermal conductance (U_f and U_r) but Equation 2 can alternatively be written (Boryeko and Chen, 2013) in terms of thermal conductivity (k=Ux), thermal power (q), heat flux (q/A), or reciprocal thermal resistance (1/R=U/A) where the dimensional quantities x and A relate to the cavity depth and surface area of the diode with A=yz applying in the case of a flat plate diode of the form shown in Figure 1. A reasonable target for diodicity of PLVTDs in CCBE applications would be ς > 97% based on replicating thermal conductivities of typical building materials such as k≈0.025 $W{\cdot}m^{-1}K^{-1}$ for polyurethane insulation and k≈1.6 $W{\cdot}m^{-1}K^{-1}$ for concrete (Twidell & Weir, 2006). Applications in solar collectors would ideally require ς > 99% to replicate absorber transparent cover arrangements in ICSSWH devices where the insulation of high quality double glazing is U≈1.2$W{\cdot}m^{-2}K^{-1}$ and heat transfer across the absorber should be U>200$W{\cdot}m^{-2}K^{-1}$ (Dupeyrat et al., 2011, Deng et al., 2019). For reference, Cui and Overend (2019) suggest that switchable insulation devices based on phase change technologies should be capable of achieving Order Of Magnitude (OOM) performance ratios of 10^2<OOM<10^4 which correspond broadly to diodicity of 98.02 < ς < 99.98%.

$$\boldsymbol{\varsigma} = \frac{\boldsymbol{U_f - U_r}}{\boldsymbol{U_f + U_r}} \qquad (0 \geq \varsigma \geq 1) \qquad \text{Equation 2}$$

2.3 Thermal resistance lumped parameter model

The thermal resistances associated with working fluid latent heat transport ($R_{LvL} = R_e + R_{ec} + R_c$) are inherently much lower than those associated with sensible heat transport ($R_v + R_L$ when horizontal or $1/[1/R_v + 1/R_L]$ when vertical). Inspection of the thermal resistance network in Figure 4c suggests that the overall thermal resistance through the PLVTD during forward mode operation (R_f) can be approximated by Equation 3 (Pugsley et al., 2017 and 2019):

$$R_f = 1/\left(\frac{1}{R_e+R_{ec}+R_c} + \frac{1}{R_w} + \frac{1}{R_s} + \frac{1}{R_R}\right) + 2R_p \qquad \text{Equation 3}$$

No latent heat transfer occurs in reverse mode because the evaporator plate is dry. The evaporation and condensation resistances therefore tend towards infinity so that

$1/(R_e+R_{ec}+R_c)\rightarrow 0$. Inspection of the thermal resistance network in Figure 4c suggests that overall thermal resistance through the PLVTD during reverse mode can be approximated (Pugsley, 2017) by Equation 4a when horizontal ($R_{r,h}$) or by Equation 4b when vertical ($R_{r,V}$):

$$R_{r,h} = 1/\left(\frac{1}{R_w} + \frac{1}{R_s} + \frac{1}{R_R} + \frac{1}{R_{L,h}+R_v}\right) + R_{pe} + R_{pc} \quad \textbf{Equation 4a}$$

$$R_{r,V} = 1/\left(\frac{1}{R_w} + \frac{1}{R_v} + \frac{1}{R_s} + \frac{1}{R_R} + \frac{1}{R_{L,V}}\right) + R_{pe} + R_{pc} \quad \textbf{Equation 4b}$$

a) Forward mode thermal resistance *b) Reverse mode thermal resistances*

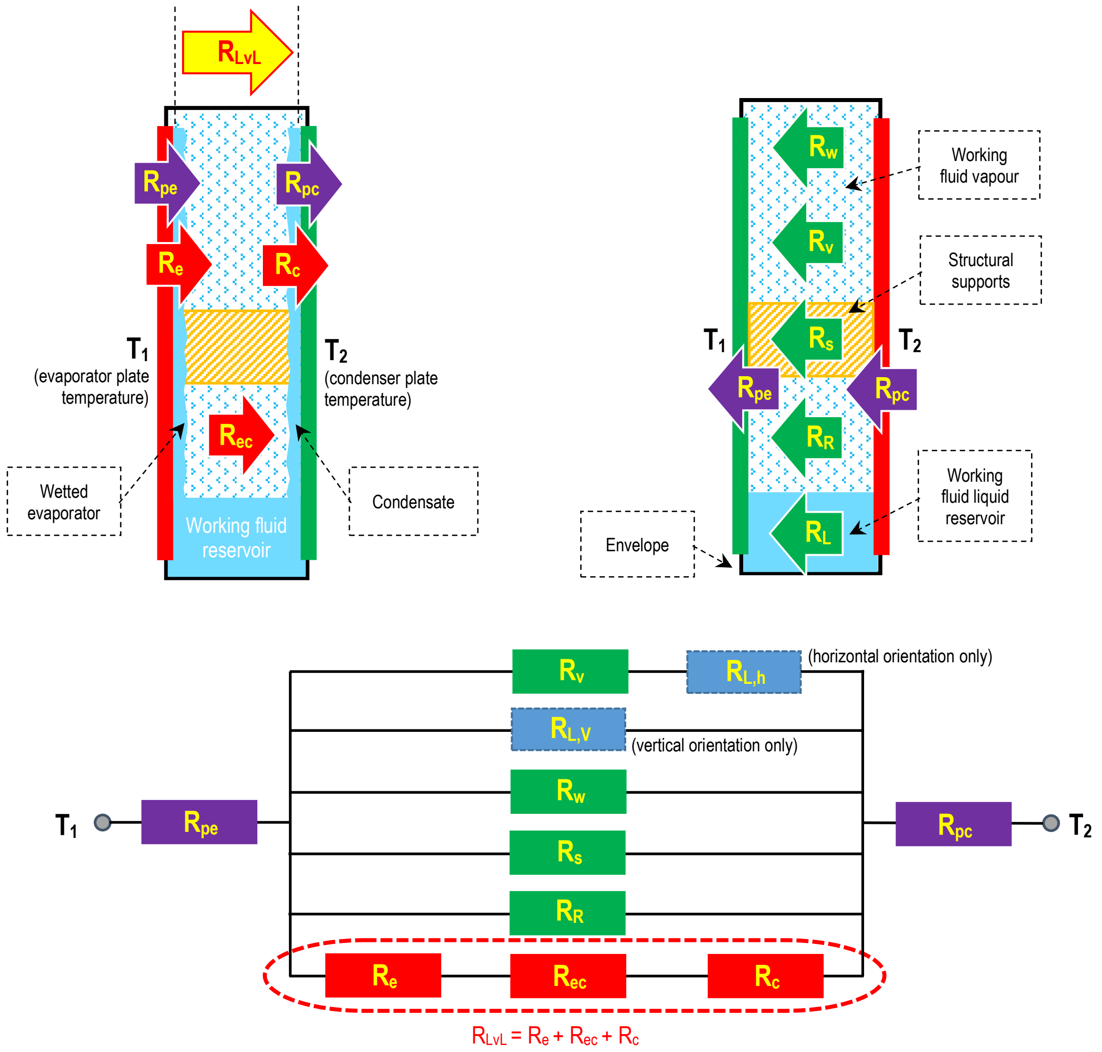

c) Thermal resistance network describing heat transfer behaviour

Descriptions of thermal resistances used in the model

R_{pe}	Conductive thermal resistance through the plate which acts as the evaporator in forward mode	R_w	Conductive thermal resistance through four sidewalls of the PLVTD envelope
R_{pc}	Conductive thermal resistance through the plate which acts as the condenser in forward mode	R_s	Conductive thermal resistance through the structural members which support the PLVTD envelope
R_e	Resistance associated with working fluid evaporation occurring at the evaporator surface	R_v	Resistance associated with vapour phase natural convection of the working fluid
R_c	Resistance associated with working fluid condensation occurring at the condenser surface	R_L	Resistance associated with Liquid phase natural convection of the working fluid
R_{ec}	Mass transfer resistance associated with the flow of vapour from the evaporator to the condenser	R_R	Resistance associated with heat transfer via long wave electromagnetic radiation between the two plates
R_{LvL}	Overall Liquid-vapour-Liquid phase change heat transfer resistance		

Figure 4 – Forward and reverse mode heat transfer paths with corresponding thermal resistance network

2.4 Heat transfer via the envelope, structure, and radiation

The PLVTD envelope and structure conductive thermal resistances can be evaluated using conventional Fourier methods. Assuming a basic rectangular box form (as per Figure 1) and an internal supporting structure formed of an array of cylindrical struts similar to that used in vacuum glazing panels (Collins and Fischer-Cripps, 1991; Fang et al., 2014) the thermal conductances and corresponding resistances of the evaporator and condenser plates ($U_{pe} \approx U_{pc}$), the envelope sidewalls (U_w), and the internal structure (U_s), can be evaluated according to Equations 5 to 9 (Pugsley et al., 2017 and 2019).

The various dimensional terms are defined in full in the Nomenclature section. The symbols U, R, k, A and d refer to thermal conductance, thermal resistance, thermal conductivity, area and distance respectively. The symbols and subscripts x, y, z refer to dimensions in the respective axes defined on Figure 1. The subscripts p, w, and s relate to the plate, wall and struts respectively. The term N_s refers to the number of struts in the internal supporting structural array where each strut is assumed to be a cylindrical tube with diameter d_s, wall thickness d_{sw}, and length x. The term d_{ss} describes the centre-to-centre spacing between adjacent struts and terms d_{sxy} and d_{sxz} refer to spacings between struts and adjacent sidewalls.

$$U_p = \frac{1}{A_p R_p} = \frac{k_p}{x_p} \qquad \text{Equation 5}$$

$$U_w = \frac{1}{A_p R_w} = \frac{2z_w(y+z-2z_w)k_w}{xyz} \qquad \text{Equation 6}$$

$$U_s = \frac{1}{A_p R_s} = \frac{N_s A_s k_s}{xyz} \qquad \text{Equation 7}$$

$$A_s = \pi\left(\frac{d_s}{2}\right)^2 - \pi\left(\frac{d_s-2d_{sw}}{2}\right)^2 \qquad \text{Equation 8}$$

$$N_s = \left(\frac{y-2d_{sxy}}{d_{ss}}+1\right)\left(\frac{z-2d_{sxz}}{d_{ss}}+1\right) = \left(\frac{y-x}{d_{ss}}+1\right)\left(\frac{z-x}{d_{ss}}+1\right) \qquad \text{Equation 9}$$

Radiative heat transfer resistance between the two parallel plates can be determined using Equation 10 (Twidell & Weir, 2006) based on the PLVTD absolute operating temperatures in Kelvin degrees ($T_{12}=0.5T_1+0.5T_2$), emissivities of the wet or dry plates (ε_1 and ε_2), the Stefan-Boltzmann constant (χ = 5.67 x 10^{-8} $W{\cdot}m^{-2}K^{-4}$) and the area over which radiative heat exchange occurs A_p.

$$R_R = \frac{1/\varepsilon_1 + 1/\varepsilon_2 - 1}{4\,\chi\,A\,(T_{12})^3} \qquad \text{Equation 10}$$

2.5 *Heat transfer via the working fluid*

Heat transfer through the PLVTD via the working fluid is dependent upon a number of different mechanisms:

- Working fluid evaporation (R_e) in forward mode.
- Latent heat transfer due to net vapour mass flow between the plates in forward mode (R_{ec}). Fluid motion is primarily driven by the vapour pressure differential (ΔP_{12} arising from ΔT_{12}) and to a lesser extent by corresponding buoyancy forces.
- Working fluid condensation (R_c) in forward mode.
- Sensible heat transfer via buoyancy driven natural convection of the working fluid, in both vapour (R_v) and liquid (R_L) states, in reverse mode due to plate-to-plate temperature differential ΔT_{12}.

Working fluid thermal resistances and corresponding conductances can be evaluated from Equation 11 (Cengel & Boles, 2006) using relevant Nusselt number correlations (Nu), characteristic dimensions (L) and working fluid thermal conductivities (k).

$$R = \frac{1}{A_p U} = \frac{L}{A_p k \cdot Nu} \qquad \text{Equation 11}$$

The evaporation thermal resistance (R_e) can be evaluated using the composite evaporation Nusselt number described by Equation 12 which accounts for conduction (Nu_{dL}) across the liquid layer thickness (d_{Le}); natural convection (Nu_{Ra}) within the liquid layer; forced convection (Nu_{Re}) in cases where the liquid is flowing; and nucleate boiling (Nu_{Nu}) if the evaporator is significantly hotter than the liquid. Equation 12 combines the natural and forced convection Nusselt numbers using the method offered by Cengel & Boles (2006). Whilst thermal conductance through the liquid layer can simply be calculated by dividing its thermal conductivity (k_L) by its thickness (d_{Le}), it is mathematically convenient to express this quantity in the form of a Nusselt number (Nu_{dLe}) which has the same characteristic dimension as that used for the convection and nucleate boiling Nusselt numbers (Nu_{Ra}, Nu_{Re} and Nu_{Nu}). Suitable Nusselt number correlations are given in Table 1 (Equations 15a-i based on expressions offered by Cengel & Boles, 2006) which are dependent upon the Rayleigh number (Ra), Reynolds number (Re), Prandtl number (Pr), hot plate tilt angle relative to horizontal (θ), and the plate dimensions (y and z). Rayleigh number quantifies the magnitude of natural convection resulting from buoyancy and frictional effects within the liquid layer in contact with the evaporator plate and is calculated in the conventional way using Equation 13 based on gravitational acceleration ($g=9.81$ m/s^2 at sea level) and the plate-to-liquid temperature difference ($\Delta T_{L1}=T_1-T_{L1}$). Reynolds number quantifies the magnitude of forced convection and is calculated using Equation 14 (after Zhou et al., 2009) based on the liquid film mass flow rate (M_L) which spreads across the evaporator plate width (y). All thermodynamic properties (k, ν, Pr, β, ρ) of evaporating working fluid involved in evaluation of R_e relate to liquid state at temperature T_{L1}, the value of which can be evaluated according to the iterative procedure proposed in Section 2.6.

In vertical and tilted PLVTDs featuring flowing film evaporators, the liquid layer thickness (d_{Le} according to Equation 15h) is largely dependent upon the same parameters as the Reynolds number but is additionally affected by gravity. In horizontal PLVTDs where the evaporator is covered by a non-flowing pool of liquid, the liquid layer thickness (d_{Le} according to Equation 15i) is primarily determined by the mass of working fluid (m_L) and the evaporator plate area (yz) but also by the PLVTD volume (xyz) and the relative densities of working fluid in both liquid (ρ_L) and vapour (ρ_v) states. Given the low heat fluxes (typically q/A<1000 W·m^{-2}) associated with PLVTDs used for CCBE and ICSSWH applications the temperature difference between the evaporator plate surface and the liquid working fluid is usually too low (T_1-T_L≤5°C) for nucleate boiling to occur which means that free-surface evaporation mechanisms typically prevail and Nu_{Nu} can usually be ignored. A correlation for Nu_{Nu} is however provided in Equation 19j (Table 3) for completeness.

$$Nu_e = \left({Nu_{dL}}^3 + {Nu_{Ra}}^3 + {Nu_{Re}}^3 + {Nu_{Nu}}^3\right)^{1/3}$$ **Equation 12**

$$Ra = \frac{g\ \beta\ \Delta T\ L^3}{v^2} Pr$$ **Equation 13**

$$Re = \frac{4M_L}{y\ v_L\ \rho_L}$$ **Equation 14**

The vapour mass transfer thermal resistance (R_{ec}) can be evaluated using the Nusselt number correlations given in Table 2 (Equations 15j-q) which describe fluid convection in rectangular enclosures of the form illustrated in Figure 2 (dimensions x, y, z and tilt angle θ). These correlations are conventionally used in sensible heat transfer scenarios where the thermal conductivity (k) is a temperature dependent property of the working fluid in a fully saturated liquid or vapour state and gravity (g) is the driving force determining the natural convection Rayleigh number (Ra). However, given that R_{ec} is associated with a liquid-vapour-liquid phase change, modified definitions of Rayleigh number (Ra*) and thermal conductivity (k*) are required. The familiar forcing term (g) typically used for determining Ra (Equation 13) is supplemented when calculating Ra* (Equation 16) by an additional forcing term (P_{Lv}/ρL) which accounts for the dominant effect of the vapour pressure differential $\Delta P_{12}=|P_1-P_2|$ associated with the plate-to-plate temperature difference. Equation 17 reflects the fact that the effective thermal conductivity (k*) of the vapour flowing during forward mode operation of the PLVTD has both sensible and latent components.

Table 1 – Nusselt number correlations for natural and forced convection of fluid heated by plates

<table>
<tr><th>Geometry and convection type</th><th>Nusselt number (Nu) correlation and characteristic dimension (L)</th></tr>
<tr><td rowspan="2">Natural convection heating of fluid above a horizontal plate (or cooling of fluid below a horizontal plate)
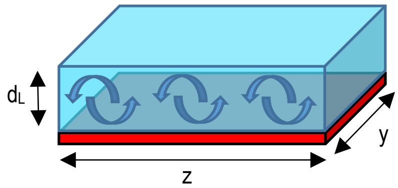
</td><td>Equation 15a $Nu_{Ra} = 0.54Ra^{0.25}$
Where: $10^4 \leq Ra < 10^7$
and: $L = \frac{yz}{2(y+z)}$</td></tr>
<tr><td>Equation 15b $Nu_{Ra} = 0.15Ra^{1/3}$
Where: $10^7 \leq Ra \leq 10^{11}$
and: $L = \frac{yz}{2(y+z)}$</td></tr>
<tr><td>Natural convection cooling of fluid above a horizontal plate (or heating of fluid below a horizontal plate)</td><td>Equation 15c $Nu_{Ra} = 0.27Ra^{0.25}$
Where: $10^5 \leq Ra < 10^{11}$
and: $L = \frac{yz}{2(y+z)}$</td></tr>
<tr><td>Natural convection heating or cooling of fluid adjacent to a vertical plate or above a tilted plate
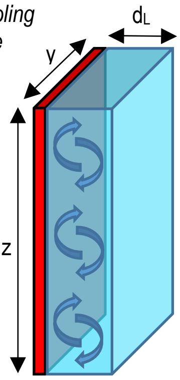
</td><td>Equation 15d
$$Nu_{Ra} = \left[0.825 + \frac{0.387Ra^{0.167}}{\left[1 + \left(^{0.492}/_{Pr}\right)^{0.563}\right]^{0.296}}\right]^2$$
Where: $L = z$</td></tr>
<tr><td rowspan="2">Forced convection heating of fluid flowing over a tilted or vertical plate
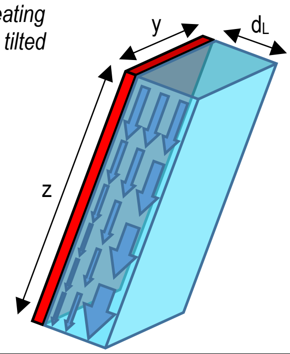
</td><td>Equation 15e
$$Nu_{Re} = 0.644Re^{0.5}Pr^{1/3}$$
Where: $Re < 5 \times 10^5$
and: $L = z$</td></tr>
<tr><td>Equation 15f
$$Nu_{Re} = (0.037Re^{0.8} - 871)Pr^{1/3}$$
Where: $5 \times 10^5 \leq Re \leq 10^7$
and: $0.6 \leq Pr \leq 60$
and: $L = z$</td></tr>
<tr><td>Pure conduction through a layer of stagnant fluid</td><td>Equation 15g
$$Nu_{dL} = \frac{L}{d_L}$$</td></tr>
<tr><td>Thickness of the liquid layer in cases where the plate is covered by a flowing film</td><td>Equation 15h
$$d_L = \left(\frac{3v_L M_L}{y\rho_L g sin(\theta)}\right)^{1/3}$$</td></tr>
<tr><td>Total thickness of the liquid layer(s) in an enclosure filled with working fluid existing in two phase states</td><td>Equation 15i
$$d_L = \frac{m_{Lv} - xyz\rho_v}{yz\rho_L}$$</td></tr>
<tr><td colspan="2"><u>Notes</u>
Nucleate boiling correlation (Nu_{Nu}) is given in Table 3 and is only relevant when evaporator plate is >5°C hotter than the liquid.
If the PLVTD is tilted by 30°≤θ≤90° from the horizontal (see Figure 2) then gravity term (g) used for determination of Rayleigh number (Ra) should be replaced by g.cos(90- θ) as suggested by Cengel & Boles (2006).
Equations 15a-f are based on those offered by Cengel & Boles (2006) whereas Equations 15g-i are based on work by Zaitsev et al. (2003), Zhou et al. (2009) and Pugsley (2017).
Flowing film liquid layer thickness estimates may become unreliable for plate tilt angles outside the range of known validity of Equations 15f and 15h which are intended to be used for cases where 90°≤θ≤175°</td></tr>
</table>

Table 2 – Nusselt number correlations for fluid filled rectangular enclosures

Orientation	*Nusselt number correlation*	*Limits*
Horizontal with cold plate at top (θ=0)	$Nu_{\theta=0} = 1 + 1.44\left[1 - \frac{1708}{Ra}\right]^{+} + \left[\frac{Ra^{1/3}}{18} - 1\right]^{+}$ **(Equation 15j)**	$0.1<Pr<10$ $Ra<10^8$
Tilted with cold plate at top (0<θ<90°)	$Nu = 1 + 1.44\left[1 - \frac{1708}{Ra.cos(\theta)}\right]^{+}\left(1 - \frac{1708[sin(1.8\theta)]^{1.6}}{Ra.cos(\theta)}\right) + \left[\frac{[Ra.cos(\theta)]^{1/3}}{18} - 1\right]^{+}$ **(Equation 15k)**	$z/x \geq 12$ $Ra<10^5$ $\theta < 70$
	$Nu = Nu_{\theta=0}\left(\frac{Nu_{\theta=90}}{Nu_{\theta=0}}\right)^{\left(\frac{\theta}{\theta_{cr}}\right)}[\sin(\theta_{cr})]^{\left(\frac{\theta}{4\theta_{cr}}\right)}$ **(Equation 15l)**	$z/x < 12$ $Ra<10^5$ $0 < \theta < \theta_{cr}$
	$Nu = Nu_{\theta=90}[\sin(\theta)]^{0.25}$ **(Equation 15m)**	$z/x < 14$ $\theta_{cr} < \theta < 90$
Vertical (θ=90)	$Nu_{\theta=90} = 0.18\left(\frac{Pr}{0.2 + Pr}Ra\right)^{0.29}$ **(Equation 15n)**	$1 < z/x < 2$ $RaPr/(0.2+Pr)>10^3$
	$Nu_{\theta=90} = 0.22\left(\frac{Pr}{0.2 + Pr}Ra\right)^{0.28}\left(\frac{z}{x}\right)^{-0.25}$ **(Equation 15o)**	$2 < z/x < 10$ $Ra < 10^{10}$
	$Nu_{\theta=90} = 0.42Ra^{0.25}Pr^{0.012}\left(\frac{z}{x}\right)^{-0.3}$ **(Equation 15p)**	$10 < z/x < 40$ $1 < Pr < 20k$ $10^4<Ra<10^7$
	$Nu_{\theta=90} = 0.46Ra^{1/3}$ **(Equation 15q)**	$1 < z/x < 40$ $1 < Pr < 20$ $10^6<Ra<10^9$
	$Nu_{\theta=90} = \frac{\left[\left[\left(\frac{Ra_{trans}}{Ra}\right)0.42Ra^{0.25}Pr^{0.012}\left(\frac{z}{x}\right)^{-0.3}\right]^3 + \left[\left(\frac{Ra}{Ra_{trans}}\right)0.46Ra^{1/3}\right]^3\right]^{\frac{1}{3}}}{\frac{Ra_{trans}}{Ra} + \frac{Ra}{Ra_{trans}}}$ **(Equation 15r)**	$1 < z/x < 40$ $1 < Pr < 20$ $10^5 < Ra < 10^8$
	$Nu_{\theta=90} = 0.171Ra^{0.265}\left(\frac{z}{x}\right)^{-0.205}$ **(Equation 15s)**	$4 < z/x < 200$ $10^2 < Ra < 10^5$
Tilted with cold plate at bottom (90<θ<180°)	$Nu = 1 + (Nu_{\theta=90} - 1)\sin(\theta)$ **(Equation 15t)**	$90 < \theta < 180$
Horizontal with cold plate at bottom (θ=180)	$Nu \approx 1$ **(Equation 15u)**	No limits

Notes

- All of the Nusselt number correlation equations are based on those offered by Cengel & Boles (2006) with the exception of Equations 15r and 15s which are respectively based upon the work of Ganguli et al. (2009) and Pugsley (2017).
- The notation [ ]$^{+}$ indicates that if the quantity in brackets is negative, it should be set to zero.
- Characteristic dimension (L) of the Nusselt number refers to the enclosure cavity width in all cases (L=x)
- According to Cengel & Boles (2006) the critical angle can be estimated as $\theta_{cr} \approx 15\ln(z/x)+30$
- Allowing for the limits of validity for Equations 15p and 15q, a suitable value for the transition Rayleigh number is $Ra_{trans}=5\times10^6$

The latent component (k_{Lv}) is determined using Equation 18 based upon the latent heat of phase change (h_{Lv}), thermal diffusivity (ϑ), working fluid molar mass ($\mathcal{M}$), and universal gas constant ($\mathcal{R}$). Equations 16 to 18 are based upon expressions proposed by Pugsley (2017) drawing upon the work of Stein et al. (1985) and Peterson (1996) and can be used in cases where all non-condensable gases have been removed from the PLVTD cavity to enable the working fluid to exist in a mixed phase state close to the saturation pressure (P_{Lv}) corresponding to the saturation temperature (T_{Lv}) which can be evaluated using the iterative procedure proposed in Section 2.6. All working fluid thermodynamic properties (k, v, Pr, ϑ, β, ρ) relate to vapour state at temperatures close to T_{Lv}. An alternative set of equations enabling evaluation of R_{ec} in cases where non-condensable gases are present is given in Appendix 1.

$$Ra^* = \frac{\left[\frac{P_{Lv}}{\rho \cdot L} + g\right] \beta \cdot \Delta T_{12} \cdot L^3}{v^2} Pr \qquad \text{Equation 16}$$

$$k^* = k_v + k_{Lv} \qquad \text{Equation 17}$$

$$k_{Lv} = \frac{{h_{Lv}}^2 \cdot P_{Lv} \cdot \mathcal{M}^2 \cdot \vartheta}{\mathcal{R}^2 \cdot {T_{12}}^3} \qquad \text{Equation 18}$$

The condensation thermal conductance (U_c), corresponding thermal resistance (R_c) and associated condensate film thickness (d_{Lc}) for PLVTDs oriented in a variety of tilt angles can be evaluated using the expressions given in Table 3 (Equations 19a-i). Condensation occurring on the surface of a flat plate will create a downward flowing film of condensate. Equations describing condensate flows across vertical and tilted plates are based on expressions given by Cengel & Boles (2006) whereas equations relevant to droplet flows from downwards-facing horizontal surfaces are based on expressions given by Stein et al. (1985) and Gerstmann & Griffith (1967). Key parameters include the saturated fluid-to-plate temperature difference (T_{Lv}-T_2), gravitational acceleration (g), plate tilt angle (θ), plate height dimension (z), condensate film Rayleigh and Reynolds numbers (Ra_c and Re_c), and various temperature dependent working fluid thermodynamic properties including latent heat of evaporation (h_{Lv}) and saturated vapour pressure (P_{Lv}). The difference in the liquid and vapour densities (ρ_L and ρ_v) plays an important role in these expressions alongside the liquid kinematic viscosity (v_L), dynamic viscosity (μ_L), surface tension (σ_L), thermal conductivity (k_L), specific heat capacity (c_{pL}) and Prandtl number (Pr_L). Liquid thermodynamic properties (subscript "L") are evaluated at the condensate film temperature T_{L2}. Vapour thermodynamic properties (subscript "v") and saturation condition thermodynamic properties (subscript "Lv") are evaluated at estimated saturation temperature (T_{Lv}). Section 2.6 describes methods for evaluating the fluid temperatures T_{L1}, T_{Lv} and T_{L2}.

Table 3 – Expressions describing phase change heat transfer mechanisms

Equations	*Orientation and liquid condition*	*Equation number*
$U_c = \frac{1}{A_p\,R_c} = 0.943\left[\frac{g\cdot cos(90-\theta)\,\rho_L\,(\rho_L-\rho_v)\,k_L^3\,(h_{Lv}+0.68\,c_{pL}[T_{Lv}-T_2])}{\mu_L(T_{Lv}-T_2)z}\right]^{0.25}$	Vertical or tilted 0<θ<135° Laminar flow condensation where Re_c<30	**Equation 19a**
$Re_c = \left[4.81+\frac{3.7\,z\cdot k_L(T_{Lv}-T_2)}{\mu_L\left(h_{Lv}+0.68c_{pL}[T_{Lv}-T_2]\right)}\left(\frac{g\cdot cos(90-\theta)}{v_L{}^2}\right)^{1/3}\right]^{0.82}$	Vertical or tilted 0<θ<135° Wavy flow condensation where 30≤ Re_c ≤1800	**Equation 19b**
$U_c = \frac{1}{A_p\,R_c} = \left[\frac{Re_c\,k_L}{1.08\,Re_c{}^{1.22}-5.2}\left(\frac{g\cdot cos(90-\theta)}{v_L{}^2}\right)^{1/3}\right]$		**Equation 19c**
$Re_c = \left[\frac{0.069\,z\cdot k_L\,Pr_L{}^{0.5}\,(T_{Lv}-T_2)}{\mu_L\left(h_{Lv}+0.68\,c_{pL}\,[T_{Lv}-T_2]\right)}\left(\frac{g\cdot cos(90-\theta)}{v_L{}^2}\right)^{1/3}-151\,Pr_L{}^{0.5}+253\right]^{4/3}$	Vertical or tilted 0<θ<150° Turbulent flow condensation where Re_c >1800	**Equation 19d**
$U_c = \frac{1}{A_p\,R_c} = \left[\frac{Re_c\,k_L}{8750+58\,Pr_L{}^{-0.5}\left(Re_c{}^{0.75}-253\right)}\left(\frac{g\cdot cos(90-\theta)}{v_L{}^2}\right)^{1/3}\right]$		**Equation 19e**
$Ra_c = \frac{g\,(\rho_L-\rho_v)\,h_{Lv}\,d_{Lc}{}^3}{k_L\,v_L\,(T_{Lv}-T_2)}$	Horizontal or tilted θ>150° Condensation on the underside of a plate where condensate flows as an array of sporadic droplet flows	**Equation 19f**
$d_{Lc} = \left(\frac{\sigma_L}{g\,(\rho_L-\rho_v)}\right)^{0.5}$		**Equation 19g**
$U_c = \frac{1}{A_pR_c} = \frac{A_c\,k_L\,0.69\,Ra_c{}^{0.2}}{A_p\,d_{Lc}}$		**Equation 19h**
$U_c = \frac{1}{A_pR_c} = \frac{A_c\,k_L\,0.787\left(\frac{P_{Lv}}{1000}\right)^{0.464}Ra_c{}^{0.2}}{A_p\,d_{Lc}}$	Horizontal or tilted θ>150° 10^6<Ra_c<10^8 300<P_{Lv}<1240kPa	**Equation 19i**
$Nu_{Nu} = \frac{L\cdot\mu_L\,h_{Lv}}{k_L}\left[\frac{g\,(\rho_L-\rho_v)}{\sigma_L}\right]^{0.5}\left[\frac{c_{pL}}{K_{sf}\,h_{Lv}\,(Pr_L)^{n_{sf}}}\right]^3[T_1-T_{Lv}]^2$	Nucleate boiling Only when T_1-T_{Lv}>5°C	**Equation 19j**

Notes

- Equations 19a-e are based on those offered by Cengel & Boles (2006). Equations 19f-i are based on work by Stein et al. (1985) citing Gerstmann & Griffith (1967). Equation 19j is a form of Rohsenow's nucleate boiling equation offered by Schmidt et al. (1993).
- Equations for vertical and tilted condenser plates are nominally valid for 0<θ≤90° but become inaccurate for θ<30° and are of unknown validity for 90<θ≤180°. Increased condensate layer thicknesses associated with orientations of θ«90° and θ»90° are likely to cause the equations to underestimate thermal resistance and overestimate the thermal conductance.
- Equations 19b-e assume that ρ_v « ρ_L which is valid for water or ethanol at temperatures in the range 0<T_L< 200°C.
- Nucleate boiling and turbulent condensate flow are generally only relevant to PLVTDs operating under high heat fluxes and are unlikely to be relevant for PLVTDs in building envelope and non-concentrating solar collector applications.
- Values for nucleate boiling constants are suggested by Cengel & Boles (2006) but can typically be taken as K_{sf} = 0.01 and n_{sf} = 1.

The liquid and vapour thermal resistances $R_{L,h}$, $R_{L,V}$ and R_v which describe heat transfer through the working fluid in reverse mode are evaluated using the general form of Equations 11 and 13 together with the Nusselt number correlations given in Tables 1 and 2. The aim is for these resistances to be as large as possible to avoid unwanted heat transfer in reverse mode when the PLVTD is intended to operate as an insulator. In a horizontal PLVTD the liquid thermal resistance ($R_{L,h}$) is usually insignificant because it acts in series with a much larger vapour thermal resistance (R_v) and can usually be ignored. In a vertical or tilted PLVTD it is preferable for $R_{L,V}$ to be made insignificant by locating the working fluid reservoir completely outside of the PLVTD (as per Pugsley, 2017 and the device discussed in Section 3 of this study) or by adding a suitable thermal break to separate the working fluid reservoir from the condenser plate (as per Pugsley et al., 2017 and the device discussed in Section 5 of this study).

2.6 Determination of working fluid temperatures

Convection and radiation within the PLVTD are driven by the overall temperature differential (ΔT_{12}). Evaluation of Equations 10 to 19 requires knowledge of the absolute and relative temperatures of the evaporator surface (T_1), condenser surface (T_2), liquid in the working fluid reservoir (T_L), evaporating liquid (T_{L1}), condensate (T_{L2}), and saturated vapour (T_{Lv}). The proposed one-dimensional model (refer to Figure 4) essentially assumes that these temperatures form a gradient T(d) across the depth of the PLVTD ($0<d<x$). The form of this temperature gradient is determined by the relative magnitudes of the thermal resistances (R_e, R_{ec}, R_c, R_w, R_s, R_R, R_p, R_L and R_v) which are in turn dependent upon the various properties of the working fluid (c_p, h_{Lv}, k, m_{Lv}, M_L, P_{Lv}, Pr, v, ϑ, $\mathcal{M}$, β, ρ, μ, and σ in liquid, gaseous and saturated states); plate surfaces and orientation (x_p, y, z, θ, g, k_p, ε_1, ε_2, n_{sf} and K_{sf}); and materials forming the envelope and structure (x, z_w, k_w, k_s, N_s and A_s). The temperature gradient can be expressed using Equation 20a in cases where T_1 and T_2 are both known, or

using Equation 20b in cases where the heat flux (q_{12}/A) and either of the driving temperatures is known (T_1 is often unknown in CCBE, BIPV and BISTS applications).

$$T(d) = T_1, T_2, d; \left\{ \begin{matrix} c_{p,L}, c_{p,v}, h_{Lv}, k_L, k_v, m_{Lv}, M_L, P_{Lv}, Pr_L, Pr_v, v_L, v_v, \vartheta_v, \mathcal{M}, \beta_L, \beta_v, \rho_L, \rho_v, \mu_L, \sigma_L \\ x_p, y, z, \theta, g, k_p, \varepsilon_1, \varepsilon_2, n_{sf}, k_{sf} \\ x, z_w, k_w, k_S, N_S, A_S \end{matrix} \right\} \quad \textbf{Eq. 20a}$$

$$T(d) = q_{12}, T_2, d; \left\{ \begin{matrix} c_{p,L}, c_{p,v}, h_{Lv}, k_L, k_v, m_{Lv}, M_L, P_{Lv}, Pr_L, Pr_v, v_L, v_v, \vartheta_v, \mathcal{M}, \beta_L, \beta_v, \rho_L, \rho_v, \mu_L, \sigma_L \\ x_p, y, z, \theta, g, k_p, \varepsilon_1, \varepsilon_2, n_{sf}, k_{sf} \\ x, z_w, k_w, k_S, N_S, A_S \end{matrix} \right\} \quad \textbf{Eq. 20b}$$

During steady state forward mode operation, the temperature gradient is likely to be ordered such that $T_1>T_{L1}>T_L\approx T_{Lv}>T_{L2}>T_2$ and in reverse mode it will be ordered as $T_1<T_{L1}<T_L<T_{Lv}<T_2$. Coarse fluid temperature estimates can be made by interpolating between plate temperatures such that $T_L=T_{Lv}=T_{12}=(T_1+T_2)/2$ and $T_{L1}=(T_1+T_L)/2$ and $T_{L2}=(T_2+T_L)/2$. Whilst reasonably robust in cases where ΔT_{12} is small, these interpolative fluid temperature estimates could generate significant errors in R_e and R_c under high heat flux scenarios when ΔT_{12} is large. A more detailed estimate of forward mode T_{Lv} can be made by considering the balance of energy and working fluid mass flows within the PLVTD as illustrated on Figure 5 and described by Equation 21 (proposed by Pugsley, 2017) assuming that thermal power flow (q_{12}) is conserved such that the input thermal power (q_e causing evaporation) is the same as the thermal output power (q_c released by condensation). Given that q_e is transferred through U_e across T_1-T_{Lv} for nucleate boiling and across T_1-T_{L1} for free-surface evaporation, and that q_c is transferred through U_c across T_{Lv}-T_2 during condensation (as described by Equations 3, 11, 12, 15 and 19) it follows that T_{Lv} can be determined by iteration to satisfy Equation 22 (proposed by Pugsley, 2017). Ignoring minor differences in $c_{p,L}$ of working fluid flows, the steady state liquid temperature (T_L) can be evaluated using Equation 23 (from Pugsley, 2017) and the iterative routine described on Figure 6.

$$\frac{q_{12}}{h_{Lv}} = \frac{q_e}{h_{Lv}} = \frac{q_c}{h_{Lv}} = M_{vec} = M_{LcS} = M_{LSe} - M_{LeS} \quad \textbf{Equation 21}$$

$$\left[\left(\frac{k_L Nu_{Nu}}{L}(T_1-T_{Lv})\right)^3+\left(\frac{k_L Nu_{dLe}}{L}(T_1-T_L)\right)^3+\left(\frac{k_L Nu_{Ra}}{L}(T_1-T_L)\right)^3+\left(\frac{k_L Nu_{Re}}{L}(T_1-T_L)\right)^3\right]^{\frac{1}{3}} = U_c(T_{Lv}-T_2) \qquad \textbf{Equation 22}$$

$$T_L = \frac{T_{L1}\,M_{LeS}+T_{L2}\,M_{LcS}}{M_{LeS}+M_{LcS}} = \frac{T_{L1}\left(M_{LSe}-\left[\frac{q_e}{h_{Lv}}\right]\right)+T_{L2}\left[\frac{q_c}{h_{Lv}}\right]}{M_{LSe}} \qquad \textbf{Equation 23}$$

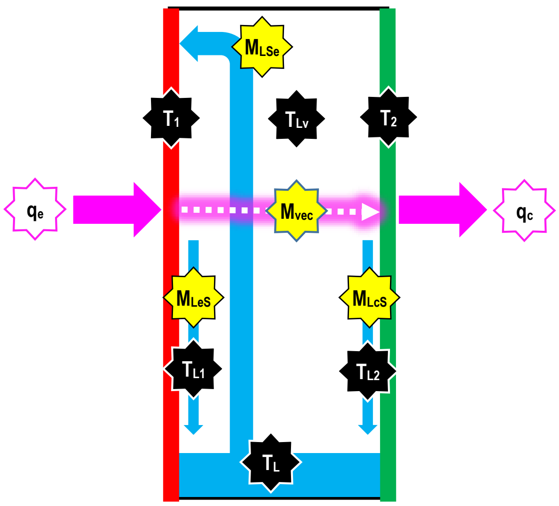

Figure 5 – Working fluid temperatures, mass flows and energy flows

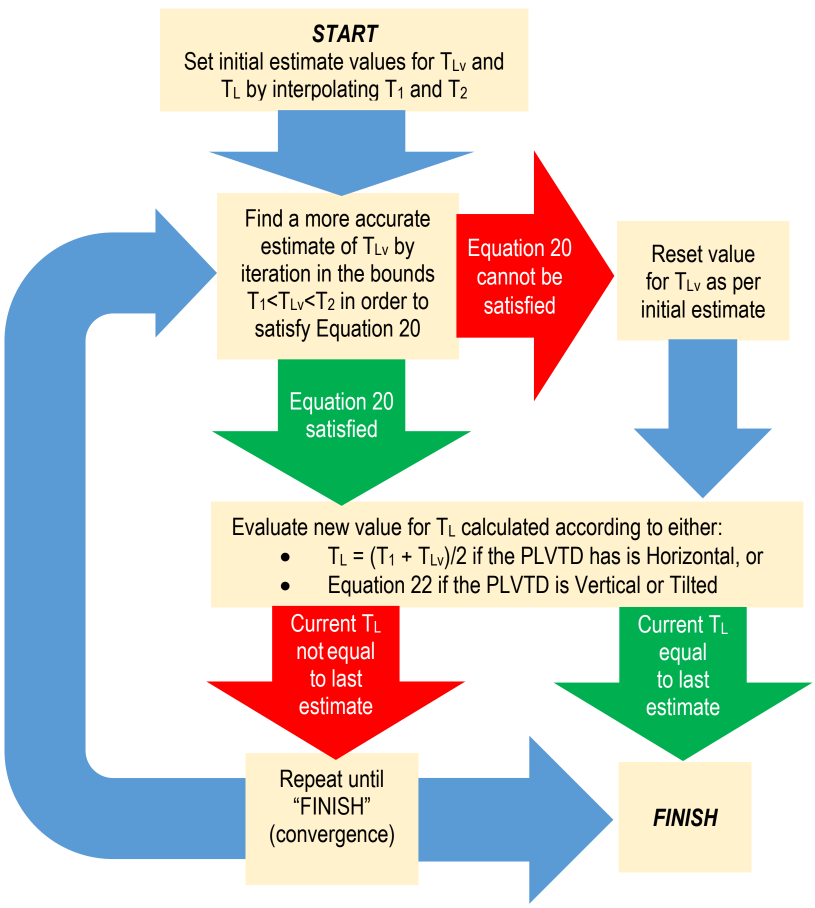

Figure 6 – Iterative process to determine saturation temperature and working fluid liquid temperature

3 Experimental validation

3.1 Methodology and apparatus

Experimental validation of the model for the case of a horizontal PLVTD was presented by Pugsley et al. (2019) using specially designed apparatus consisting of two parallel isothermal plates (A_p=0.15m^2) with integral serpentine heat exchangers and external insulation. A hermetically sealed PLVTD cavity of variable depth was formed between the plates by inserting a sidewall spacer frame. Temperature difference between the plates was controlled by connecting each heat exchanger to a separate heating-cooling fluid circuit. Fluid flow and return temperatures were measured along with flow rates to enable determination of the delivered thermal power. Small amounts of heat loss from the PLVTD were quantified and corrected for by considering the difference in thermal power supplied to the heating plate and that recovered by the cooling plate. Plate and ambient temperatures were also measured to enable determination of forward and reverse mode thermal conductances as well as heat loss coefficients under various temperature difference and heat flux operating scenarios. Experiments featured in the present study were undertaken using a modified version (see Figure 7) of the apparatus which enabled the PLVTD to operate in a vertical orientation. This was facilitated by the addition of a falling-film evaporator wetting mechanism which consisted of linear nozzle fed with working fluid pumped from an external reservoir. The general arrangement of the apparatus, instrumentation and the experimental methodology was similar to that described by Pugsley et al. (2017 and 2019). Non-condensable gases were removed from the PLVTD cavity using a vacuum pump before and after injection of the working fluid (deionised water). A brief summary description of the modified PLVTD and instrumentation is given below and in Table 4:

- **Evaporator and condenser plates:** Each constructed of 12mm thick aluminium with 6mm thick backing plates. Aluminium has high thermal conductivity enabling heat spreading to achieve broadly isothermal phase change heat transfer surfaces. Uniform heat addition/removal was achieved via serpentine flows of hot and cold water pumped through specially arranged parallel flow channels milled into the rear surface of each 12mm plate. The front surface of each plate featured a channel for an O-ring seal that formed the hermetic enclosure of the PLVTD. The evaporator and condenser plate area and thickness was selected so as to withstand implosion forces associated with vacuum pressures inside the PLVTD.

- **Cavity sidewall spacer frames**: These were detachable and reconfigurable to facilitate investigation of different cavity depths. The results presented here relate to tests undertaken with a x_w=22mm thick aluminium spacer. The intervening cavity was kept free from structural elements which might otherwise affect working fluid convection patterns and/or cause thermal bridging.
- **Evaporator wetter nozzle, working fluid reservoir, and pump**: The wetter nozzle consisted of a 10mm thick aluminium plate with trunk-and-branch fluid flow distribution channels milled into its surface. This was bolted to the front surface of the evaporator plate (see Figure 7) and acted as a diffuser to distribute a film of working fluid liquid evenly across the evaporator plate surface. The working fluid reservoir contained a total fluid mass of m_{Lv}=0.25kg. Wetter nozzle fluid flow (M_{LSe}≈0.01kg/s) was provided by a small electrically driven centrifugal pump drawing from the base of the reservoir (shown on Figure 7 with insulation omitted). Run-off flows from the evaporator (M_{LeS}) and condenser (M_{LcS}) returned to the reservoir under gravity through a hole in the base of the evaporator plate.

Table 4 – Summary details of experimental apparatus and instrumentation

Element	*Dimensions and measurement uncertainties*	*Descriptions and notes*
Evaporator and condenser plates	*Whole PLVTD:* y=0.50m, z=0.30m, A=0.15m^2 *Free evaporator surface:* d_y=0.40m, d_z=0.24m, A=0.106m^2 *Free condenser surface:* d_y=0.44m, d_z=0.24m, A=0.096m^2 *Port holes diameter:* 16mm (KF16 vacuum fitting)	Heat transfer surfaces were bare aluminium (standard smooth, dull, mill finish) cleaned using isopropyl alcohol to remove any grease. Evaporator area was smaller than condenser area owing to the evaporator wetter nozzle. Vacuum port located at top of condenser plate. Reservoir port located at bottom of evaporator plate (refer to Figure 7).
Serpentine heat exchangers	*Total length of fluid channel:* 7m (each plate) *Cross-section of fluid channel:* 4mm x 4mm *Flow & return ports:* ½" BSP (at centre of plate)	Fluid conduits for serpentine heat exchangers formed by milling a square section channel into the rear side of the heat transfer plate. Refer to Pugsley (2017) for details.
Evaporator wetting mechanism	*Reservoir capacity:* 0.8 Litre (max) *Pump-to-nozzle connection:* 550mm long, 6mm inner Ø *Nozzle trunk channel:* d_x=8mm, d_y=230mm, d_z=6mm *Nozzle branches:* 12 channels each d_x=2mm, d_y=4mm, d_z=6mm *Nozzle aperture width:* d_x=0.5mm *Nozzle aperture length:* d_y=230mm *Volume flow rate*: 0.6±0.1 Litre/second	PLVTD working fluid stored in external reservoir formed from 100mm long ISO100 vacuum fitting. Fluid flow driven by TCS M400M centrifugal pump. Nozzle formed from 10mm thick aluminium plate with trunk-and-branch fluid flow distribution channels milled into its surface. Refer to Pugsley (2017).
Temperature sensors	*Number of thermocouples on each plate:* 3 *Number of thermocouples at each flow & return port:* 1 *Thermocouple specification:* T-type (spot-welded tip) *Temperature uncertainty each thermocouple:* ±1.0°C *Temperature uncertainty thermocouple pairs:* ±0.3°C *Sampling regime:* Reading taken every 5 seconds, with average value recorded every 30 seconds	The magnitude of uncertainty in absolute temperatures recorded for each thermocouple is primarily caused by the uncertainty associated with the DeltaT DL2e datalogger's internal thermistor. Uncertainty associated with thermocouple pairs used for temperature difference measurements is therefore lower.
Heating and cooling fluid circuits and flow rate sensors	*Flow rate uncertainty:* ±9% in measured range *Flow meter signal output:* 2250 Pulse/Litre *Sampling regime:* Continuous pulse count with average value recorded every 30 seconds	Flows through each serpentine heat exchanger were monitored using a Nixon OG1 oval gear volumetric flow meter with active pulse output monitored by DeltaT DL2e datalogger. Flow rates were set by pump speed switch and manual ball valves.
Vacuum pump and pressure sensor	Pressure uncertainty (dry air at 2kPa): ±3% Pressure uncertainty (water vapour at 2kPa): ±20%	Vacuum created by an Edwards XDS5 scroll pump which was isolated by gate value during tests. Pressure measured using a Druck DPI-104 diaphragm pressure gauge.

3.2 Reverse mode performance

Figure 8 shows the measured temperature, pressure and flow rate time history for the reverse mode tests on the vertical PLVTD with 22mm aluminium spacer. For continuity, results have been presented in a similar manner to those reported previously by Pugsley et al. (2019) for the horizontal PLVTD with 11mm nylon spacer. Average temperatures of the heating and cooling plates are denoted by T_{HC} and T_{CH} respectively. Hot and cold supply temperatures are denoted by $T_{H(HC)}$ and $T_{C(CH)}$ respectively with corresponding return flow temperatures denoted by $T_{C(HC)}$ and $T_{H(CH)}$. The numbered labels show seven condenser plate temperature setpoints corresponding to approximately T_2=25, 30, 35, 38, 41, 44, 47°C with evaporator plate temperatures being maintained ΔT_{12}=20±5°C cooler. It proved difficult to control exact plate temperature setpoints as this required very fine manual adjustments to heating and cooling circuit flow control values (hence the noted ±5°C variability) but temperatures typically became very stable after allowing for initial 20-30 minute transients after each setpoint change. Measured pressures $P_{(meas)}$ increased with increasing temperature and correspond closely to estimated saturation pressures $P_{Lv(HCCH)}$ which were determined from thermodynamic tables using the average operating temperature $T_{HCCH}=(T_{HC}+T_{CH})/2$ as a lookup variable. The supply temperatures and flow rates ($M_{HC}=M_{CH}=0.3\pm0.05$L/min, slight decrease with increasing temperature) of fluids controlling the plate temperatures were kept broadly constant throughout the tests by Julabo FM33A automatically controlled heating-cooling circulators. Figure 9 shows the derived thermal powers and conductances corresponding to the raw data presented on Figure 8. Steady state thermal power of $q_{HC}=-q_{CH}=35\pm8$ W was maintained during each measurement subsequent to each setpoint change transient. Corresponding steady state reverse mode thermal conductances for the PLVTD with 22mm aluminium spacer were consistently $U_r=12$ W·m^{-2}K^{-1}, increasing slightly with increasing temperature. As indicated on Figure 10, these results are consistent with the theoretical model and, as expected, are slightly higher than those achieved for the horizontal PLVTD with 11mm nylon spacer (Pugsley et al., 2019). Interrogation of the model suggest that this is primarily due to increased conduction through the sidewalls ($U_w=10.7$ W·m^{-2}K^{-1} for 22mm aluminium spacer with rubber O-ring seals compared to $U_w=6.7$ W·m^{-2}K^{-1} for the 11mm nylon spacer). Gaseous conduction through the vapour also has an influence on overall performance ($U_v=0.9$ W·m^{-2}K^{-1} for 22mm vertical cavity compared to $U_v=1.8$ W·m^{-2}K^{-1} for the 11mm horizontal cavity). Vapour convection appears to have a very minimal role except at the highest temperatures in the vertical case. Measured results are broadly consistent with the modelled phenomenon of radiant heat transfer being greater for horizontal PLVTDs ($U_R=1.1$ W·m^{-2}K^{-1}) than for vertical PLVTDs ($U_R=0.6$ W·m^{-2}K^{-1}). This occurs because dry metal surfaces (vertical evaporator plate, wetter pump inactive in reverse mode) have lower emissivity than wet surfaces (evaporator plate is permanently wet in a horizontal PLVTD).

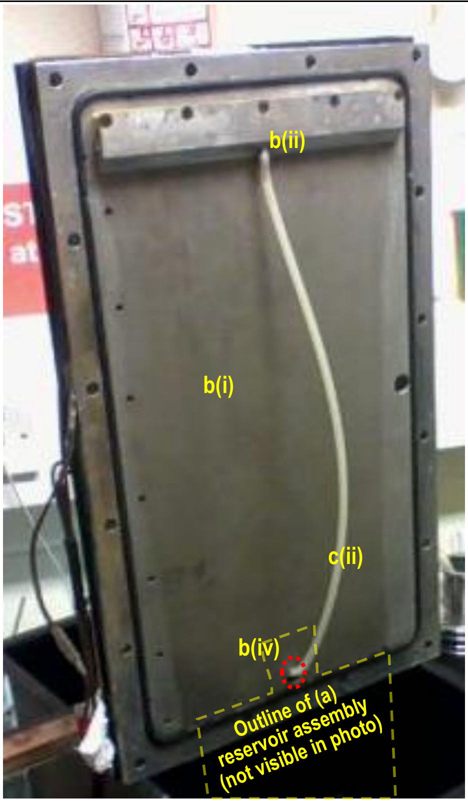

Wetter nozzle fixed on to evaporation surface, viewed with cavity sidewalls and condenser plate removed

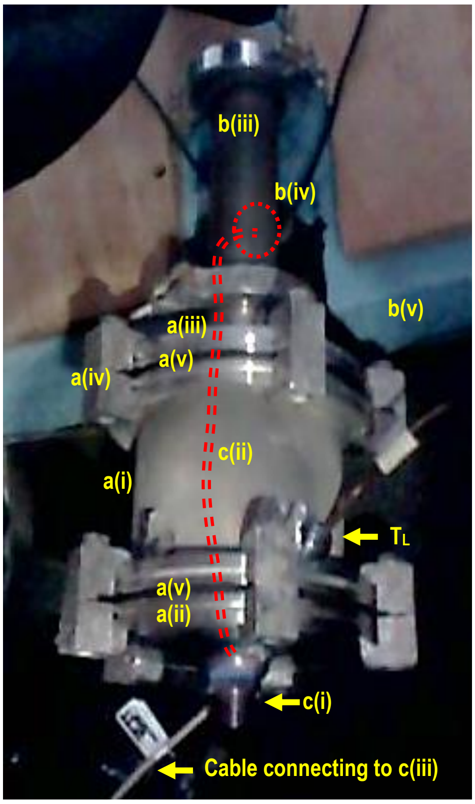

Reservoir assembly, pump and insulation on rear face of evaporator plate

Key to annotations

Working fluid reservoir:

a(i)	Working fluid reservoir main body (100 mm long ISO100 full nipple stainless steel vacuum fitting)
a(ii)	Pump manifold (ISO100 stainless steel blank flange)
a(iii)	ISO100/KF40 reducer flange
a(iv)	Clamps
a(v)	Seal (Viton o-ring)

Evaporator plate and wetter nozzle:

b(i)	Evaporator plate front surface
b(ii)	Evaporator wetter nozzle
b(iii)	KF40/16 reducing T-piece with blank flange at one end, Viton o-rings and clamps.
b(iv)	Working fluid return hole
b(v)	Thermal insulation (50 mm blue Styrofoam)

Fluid pumping and measurement:

c(i)	Centrifugal manifold mount micro pump TCS model M400M
c(ii)	6 mm internal diameter nylon tube
c(iii)	0-24V DC power supply
T_L	Thermocouple for measuring working fluid liquid reservoir temperature

Figure 7 – Photographs of vertical PLVTD prototype

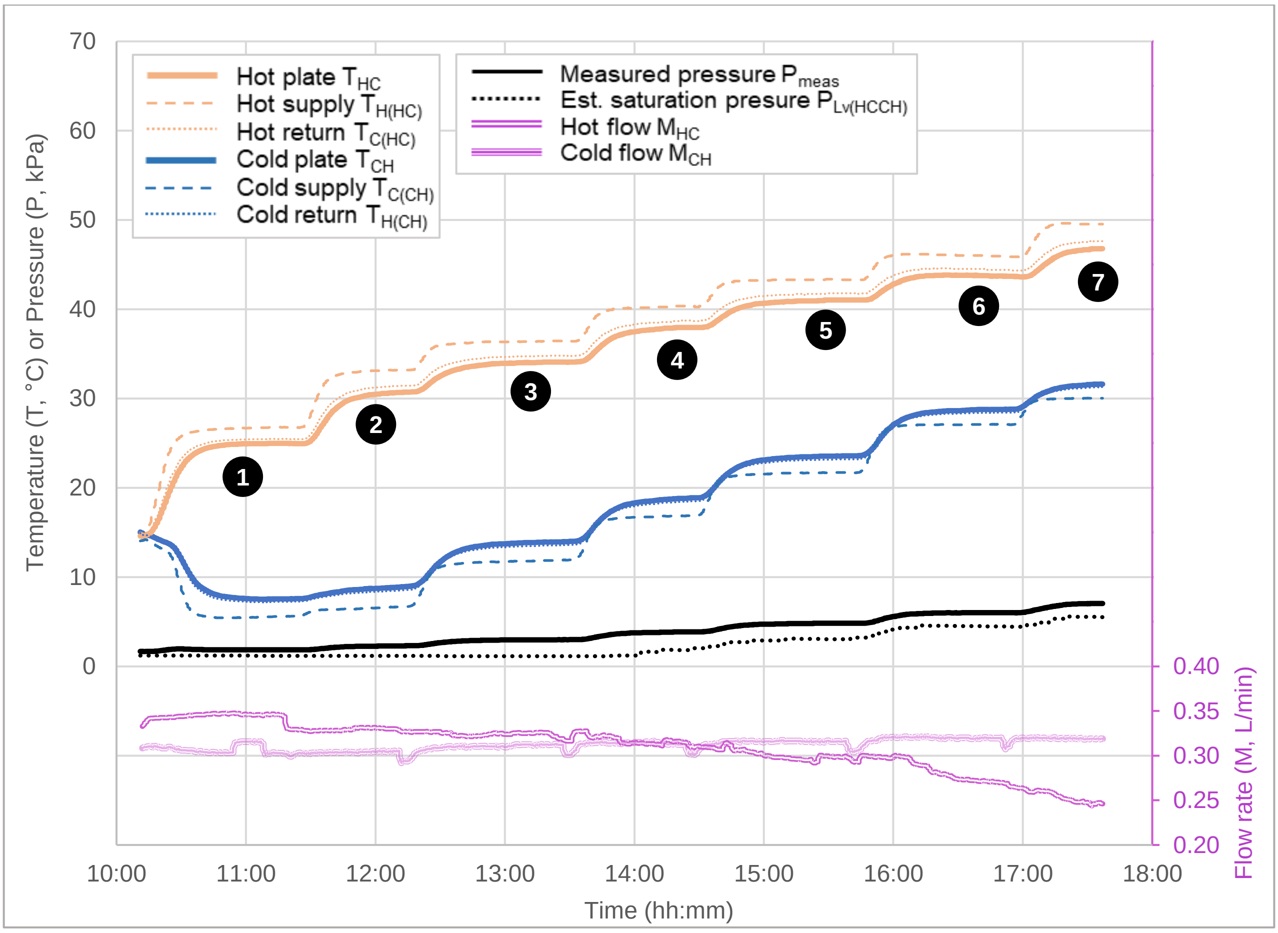

Figure 8 – Time history of measured temperatures, pressures and flow rates during reverse mode test

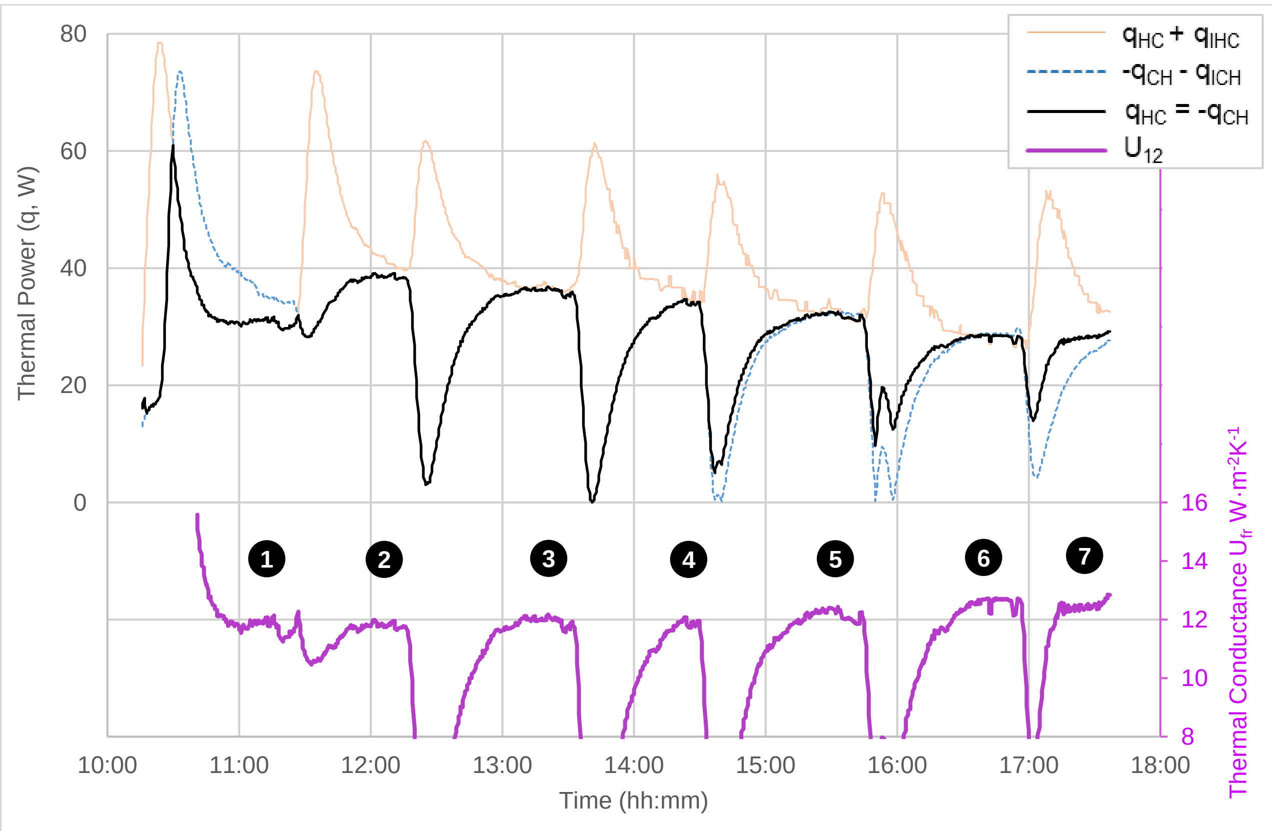

Figure 9 – Time history of derived thermal powers and conductance during reverse mode test

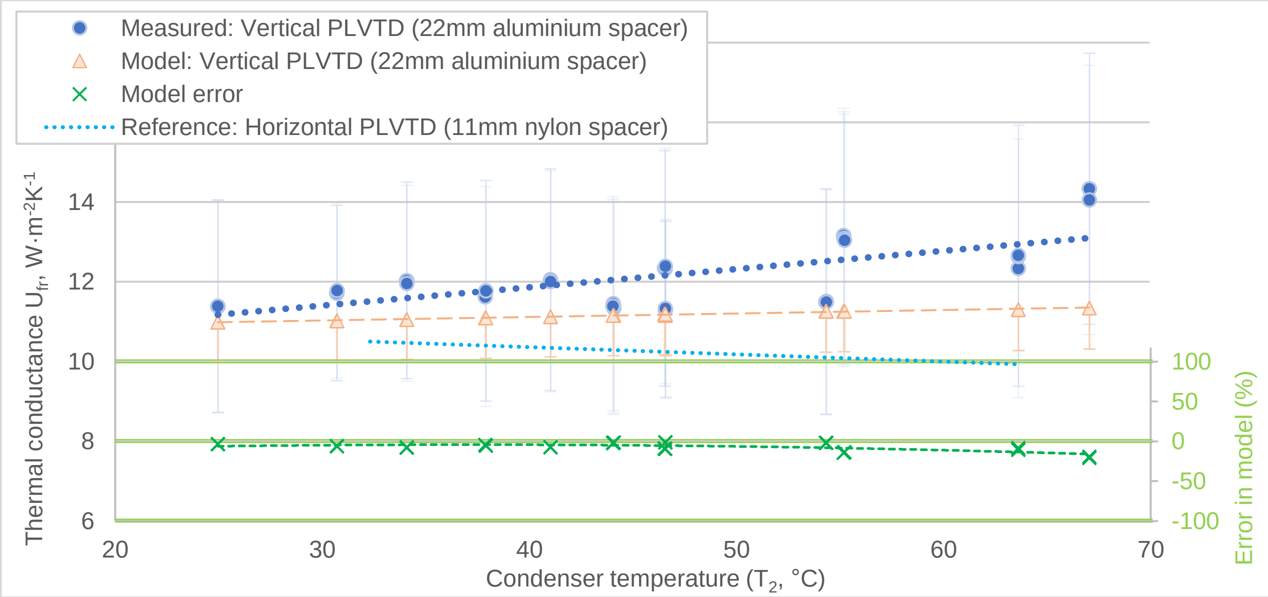

Figure 10 – Reverse mode performance of 22 mm aluminium spacer vertical PLVTD

3.3 Forward mode performance

Tests were undertaken to determine how forward mode thermal conductance varies with driving heat flux (q_{HC}/A_p by varying plate-to-plate temperature difference ΔT_{12}) and operating temperature (by varying condenser plate temperature T_2). As noted in Section 3.2, it was very difficult to establish exact plate temperature setpoints, but temperatures typically remained steady after each initial stabilisation transient. Results on Figure 11 show behaviour for constant T_2=33±4°C with setpoint steps in the range 0.5<ΔT_{12}<8°C to achieve 216<q_{HC}/A_p<4913 W·m^{-2}. Reliable measurements at lower heat fluxes were not possible owing to limitations of temperature measurement accuracy (discussed further in Section 3.4). Steady state forward mode thermal conductance remained broadly constant at U_f≈400 W·m^{-2}K^{-1} for heat fluxes in the primary range of interest for CCBE and ICSSWH applications (0.5<ΔT_{12}<2.5°C corresponding to q_{HC}/A_p<1000 W·m^{-2}). At ΔT_{12}≈5.3°C (q_{HC}/A_p≈3000 W·m^{-2}) the measured result of U_f≈560 W·m^{-2}K^{-1} corresponds to a 40% increase per of trebling of heat flux. This effect is broadly consistent with the model which suggests that increasing plate-to-plate temperature difference increases convection driving forces thereby decreasing evaporation thermal resistance (R_e) and vapour mass flow resistance (R_{ec}) to cause overall thermal conductance to increase (refer to Figure 15). Results on Figure 12 show behaviour for constant ΔT_{12}=4.5±1.5°C (corresponding to q_{HC}/A_p≈2000 W·m^{-2}) and stepped condenser temperature setpoints (13<T_2<57°C). Steady state forward mode thermal conductance increased proportionally with condenser plate temperature from U_f≈175 W·m^{-2}K^{-1} at T_2≈15°C up to U_f≈720 W·m^{-2}K^{-1} at T_2≈45°C, an increase of about 4-5% per degree. The model suggests this trend is primarily due to decreased vapour mass flow resistance (R_{ec}) caused by working fluid viscosity decreasing with increasing temperature (refer to Figure 16). The highest recorded performance was U_f≈1200 W·m^{-2}K^{-1} at T_2≈55°C with ΔT_{12}≈2.2°C corresponding to q_{HC}/A_p≈2800 W·m^{-2}.

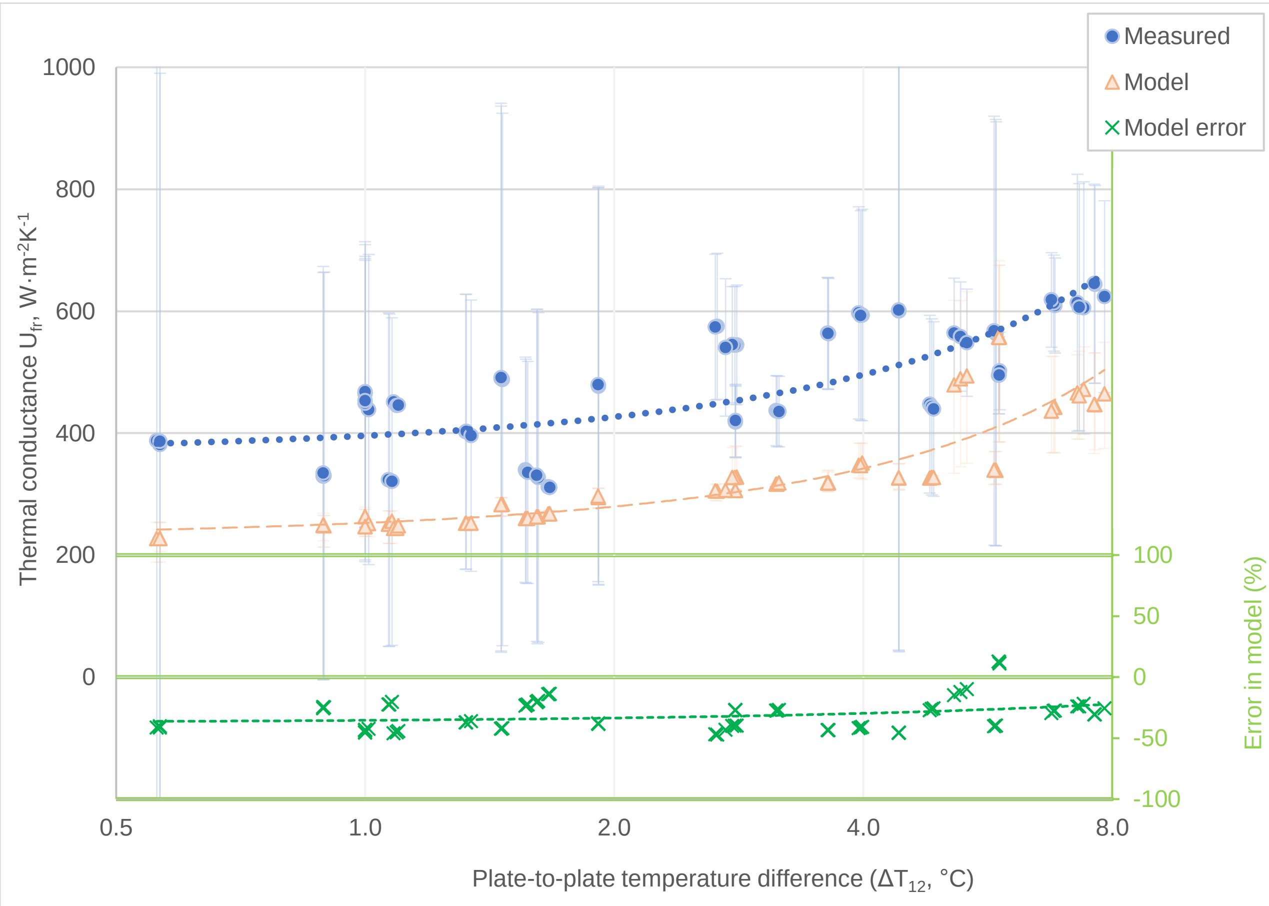

Figure 11 – Forward mode performance of 22 mm aluminium spacer vertical PLVTD (varying plate-to-plate temperature difference)

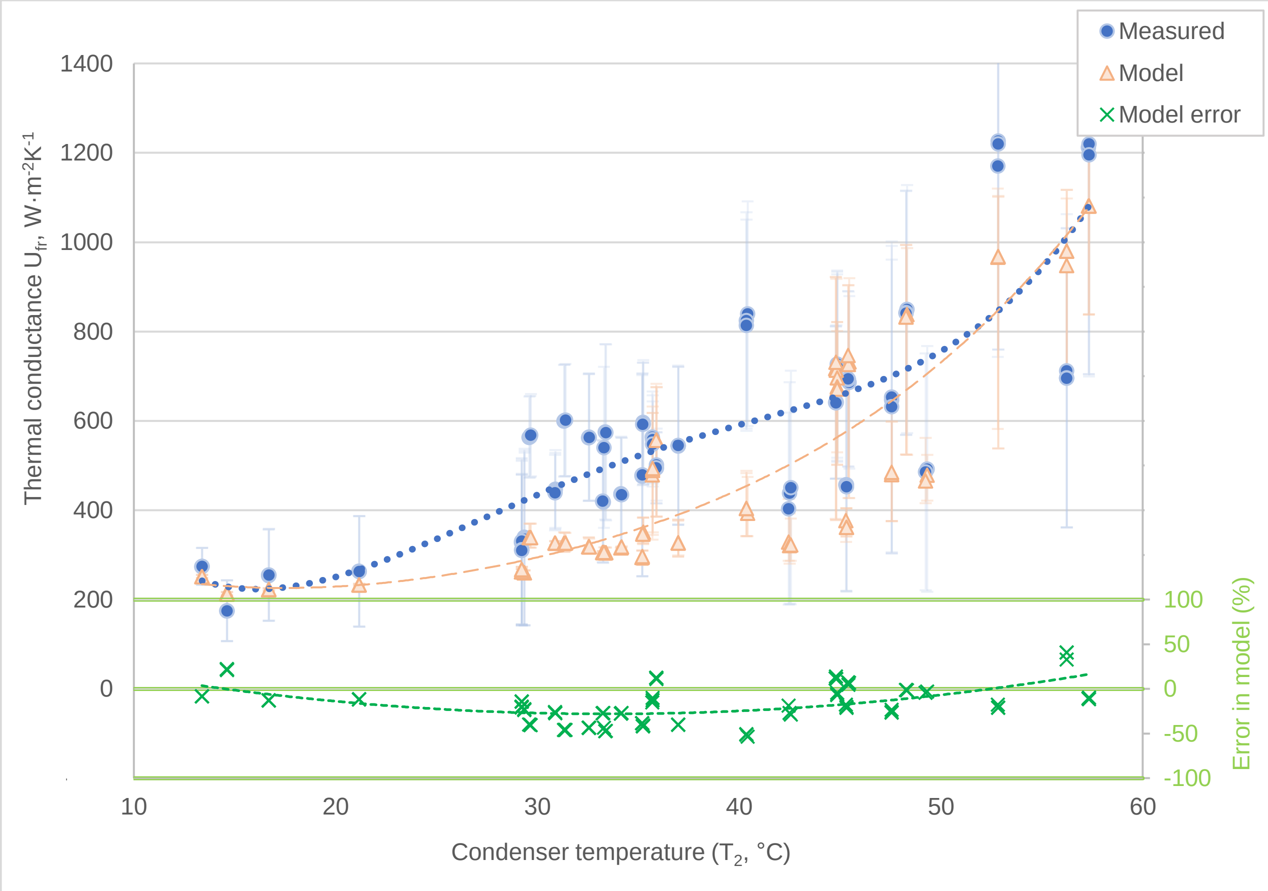

Figure 12 – Forward mode performance of 22 mm aluminium spacer vertical PLVTD (varying condenser temperature)

3.4 Uncertainty and validity

As indicated by the error bars on Figures 10, 11 and 12, measurement uncertainty in the derived thermal conductance results is typically ±25%. This uncertainty is primarily a manifestation of temperature measurement uncertainties (±0.3°C for ΔT between any two thermocouples, see Table 4) which propagate into derived results. Uncertainty becomes more significant for scenarios involving small plate-to-plate (ΔT_{12}<1°C) or flow-to-return (ΔT_{HC}<2°C) temperature differences. Whilst this is clearly significant in the context of individual results, the overall trends apparent in the data are considered robust owing to the relatively large number of data points and repeated tests undertaken. A thorough discussion and explanation concerning the treatment of uncertainty is presented by Pugsley et al. (2017 and 2019).

Comparison of measured and modelled data indicates that the reverse mode model is a good predictor, with average model error being only -8%. This represents a slight underprediction bias, which, on the basis that it worsens steadily with increasing temperature (as apparent on Figure 10) is thought to be related to sidewall effects upon vapour convection (refer to Corcione, 2003) which are not accounted for in the model. The forward mode model appears to be a less accurate predictor (average modelling error -24%) but the anticipated behavioural trends are very clearly apparent in the experimental data. One possible explanation for the "apparent" modelling error could be that the model is actually correct, but that the measured forward mode thermal conductances suffer from a +24% bias error. This explanation is consistent with the estimated ±25% uncertainty for measured thermal conductances and could feasibly occur if plate temperature measurement uncertainties manifest as biases which cause true ΔT_{12} values to be underestimated. Another possible explanation is that the vapour convection calculations become inaccurate during the laminar-to-turbulent transition ($Ra \approx 10^6$). Results on Figure 12 suggest that the model predicts reasonably accurately at the lowest and highest condenser temperature setpoints where the vapour convection Nusselt numbers are calculated using Equation 15q (low temperatures corresponding to $Ra<10^5$) and Equation 15s (high temperatures corresponding to $Ra>10^8$) respectively, but consistently underpredicts for mid-range temperature setpoints (in the transition region where Equation 15r applies). Evidence that the model predicts accurately for laminar vapour convection cases ($Ra<10^5$ for all datapoints on Figure 10) but consistently underpredicts for turbulent transition vapour convection cases ($Ra>10^6$ for all datapoints on Figure 12) supports this explanation and suggests that further refinement of Equation 15r should be sought.

Experimental work to date has focussed on validating the proposed model for the cases of horizontally (Pugsley et al., 2019) and vertically (the present study) oriented PLVTDs with all non-condensable gases removed. The validity of the model in respect of tilted orientations will need to be examined as part of further experimental work. Likewise, further work to augment early experimental validation (reported by Pugsley, 2017) is required in respect of the proposed model variant (refer to Appendix A) which accounts for non-condensable gases.

4 Parametric design considerations

The theoretical model can be used to examine the effect of key PLVTD design parameters to develop an optimised design for CCBE and ICSSWH applications. Figure 13 shows how reverse mode thermal conductance (U_v) of water vapour is dependent upon the cavity depth (x) for various aspect ratios (z/x) and orientations (θ) under nominal assumed operating conditions (T_1=10°C and T_2=60°C). Calculations consider plate-to-plate cavity depths in the range $10 \leq x \leq 200$ mm and plate height dimensions of 200<z<4000 mm. The θ=180° horizontal PLVTD offers the lowest (best) vapour convection thermal conductance because the heat source is at the top of the cavity and the resulting vapour stratification prevents convection (gaseous conduction only). Conversely, the θ=0° horizontal orientation promotes convection and results in the highest (worst) thermal conductances. Vertical and tilted PLVTDs yield conductances in the range between these extremes with high aspect ratios (z/x>12) and high tilt angles (θ>45°) giving the best reverse mode performances. Cavity depths in the range 30<x<200 mm result in $U_v<0.7$ $W \cdot m^{-2}K^{-1}$ for all orientations, irrespective of aspect ratio and heat transfer occurs via gaseous conduction only for plate-to-plate cavity depths of x<40 mm (irrespective of θ or z/x). Cavity depth of x≈50 mm yields optimal effective reverse mode thermal conductivity ($k=U \cdot x$) for tilted PLVTDs whereas x≈75 mm is more suitable for high aspect ratio vertical PLVTDs (z/x>12).

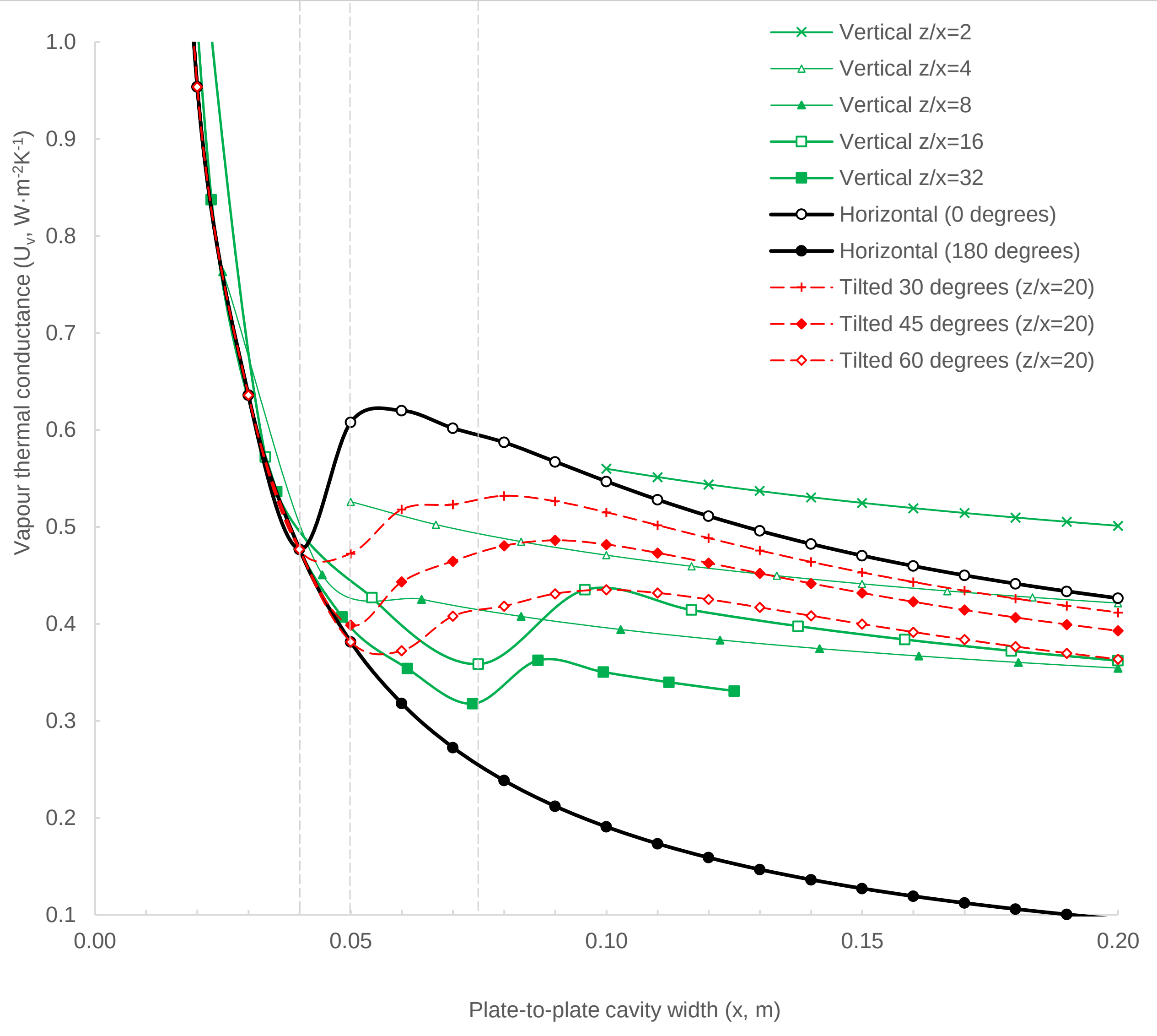

Figure 13 – Dependence of reverse mode water vapour thermal conductance on orientation and dimensions

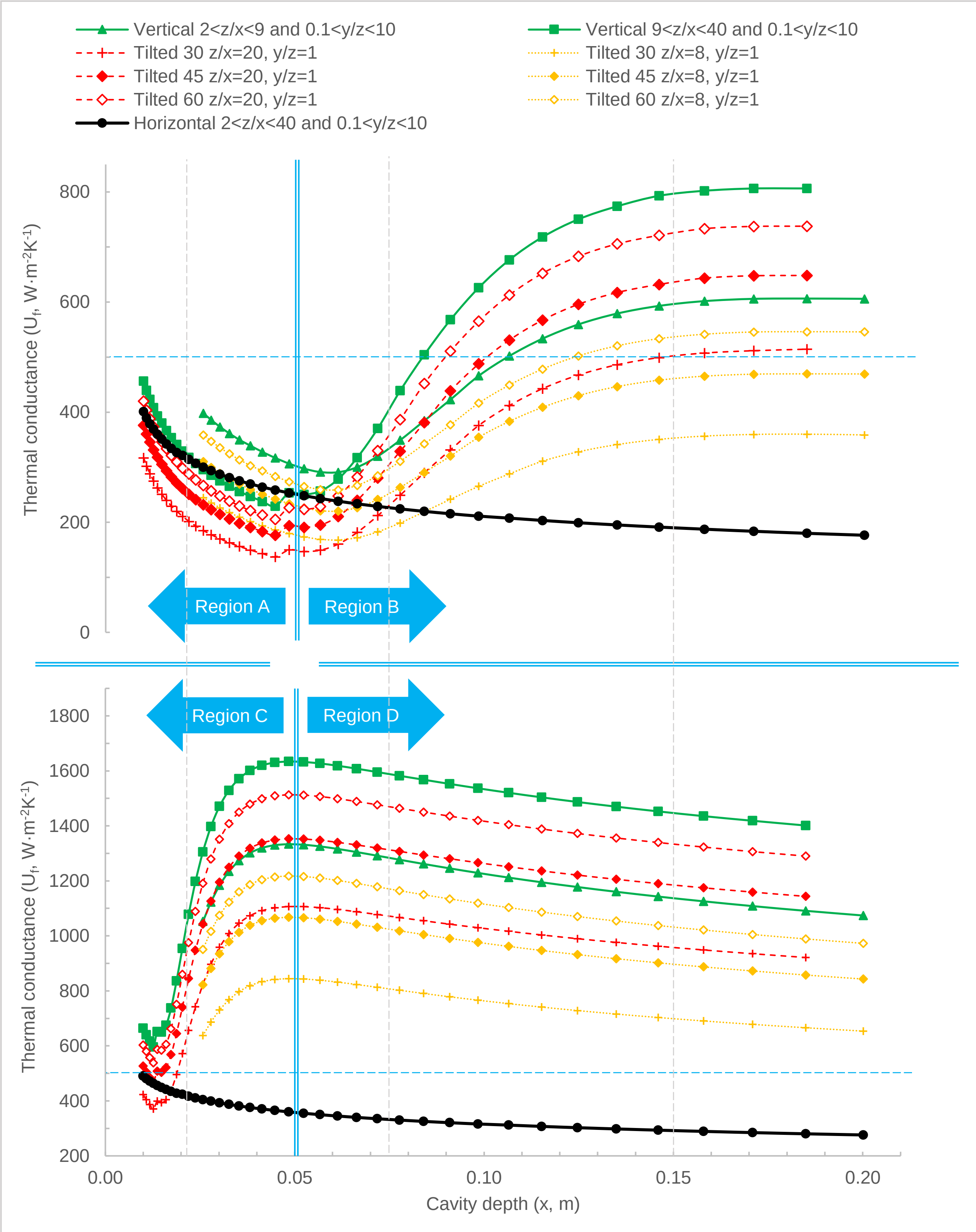

Figure 14 – Forward mode thermal conductances in PLVTDs with different orientations and dimensions (Upper graph: T_2=15°C at ΔT_{12}=5°C, Lower graph: T_2=60°C at ΔT_{12}=1°C)

Figure 14 shows how overall forward mode thermal conductance (U_f) is dependent upon cavity depth ($10<x<200$ mm) for horizontal, tilted, squat vertical, and slender vertical PLVTDs ($200< y$ & $z <4000$ mm). The upper graph describes operation with T_2=15°C condenser plate and heat fluxes corresponding to $500<q/A<2500$ W·m^{-2} in Region "A" and $750<q/A<4000$ W·m^{-2} in Region "B" whereas the lower graph (Regions "C" and "D") describe operation at T_2=60°C and $250<q/A<2000$ W·m^{-2}. Calculations assume water as working fluid ($m_{Lv}/yz=1$ kg/m^2) distributed evenly across the evaporator surface at a flow rate of $M_L/y=0.1$ kg·m^{-1} s^{-1} with all non-condensable gases removed. Cross-checking against Figures 11 and 12 confirms that the modelling predictions for a vertical PLVTD with x=22mm and z/x=20 are broadly consistent with the experimental results. The following can be concluded from Figure 14:

- Vertical PLVTDs generally achieve higher (better) forward mode thermal conductances than PLVTDs in horizontal and (most) tilted orientations.
- Conductance decreases with increasing cavity depth for horizontal PLVTDs and for vertical/tilted PLVTDs within Regions "A" & "D" but increases with increasing cavity depth for vertical/tilted PLVTDs within Regions "B" & "C".
- Vertical and tilted PLVTDs generally achieve maximum conductance when combined with relatively tall plates ($z/x>9$) giving the PLVTD a "slender" form, although "squat forms" tend to perform better within Region "A" (conditions with low temperatures and low heat fluxes).

These conclusions suggest that PLVTD dimensions can be optimised to suit expected operating conditions. Forward mode thermal conductances of $U_f>100$ W·m^{-2}K^{-1} appear achievable irrespective of orientation or operating condition and with little regard to optimising dimensions. It appears possible to achieve $U_f>500$ W·m^{-2}K^{-1} for vertical/tilted PLVTDs across the temperature range by designing them with x=150mm cavities and slender aspect ratios ($z/x\approx20$). If the cavity of a vertical PLVTD is set at

75mm (optimal for reverse mode performance, as per Figure 13) and aspect ratio is set at z/x=20 then forward mode conductances of $400<U_f<1600$ W·m^{-2}K^{-1} can be expected for $15<T_2<60$°C and $1500<q/A<2000$ W·m^{-2} operating conditions. Figures 15 and 16 illustrate how forward mode thermal conductance (overall U_f and individual components U_e, U_{ec} and U_c) of a PLVTD of dimensions x=75mm, y=750mm and z=1500mm constructed of 1mm stainless plates and sidewalls with internal supporting structure formed of stainless steel tubular struts spaced at d_{ss}=0.075m centres, would be expected to vary with heat flux and temperature. Figure 17 shows calculated temperature and heat flux dependence of the overall reverse mode thermal conductance of the same device. Results suggest that reverse mode conductances of $1.7<U_r<2.5$ W·m^{-2}K^{-1} can be expected for average operating temperatures of $5<T_{12}<50$°C (corresponding to $15<T_2<60$°C when ΔT_{12}=20°C) which implies diodicity of $\varsigma>99\%$ across the temperature range.

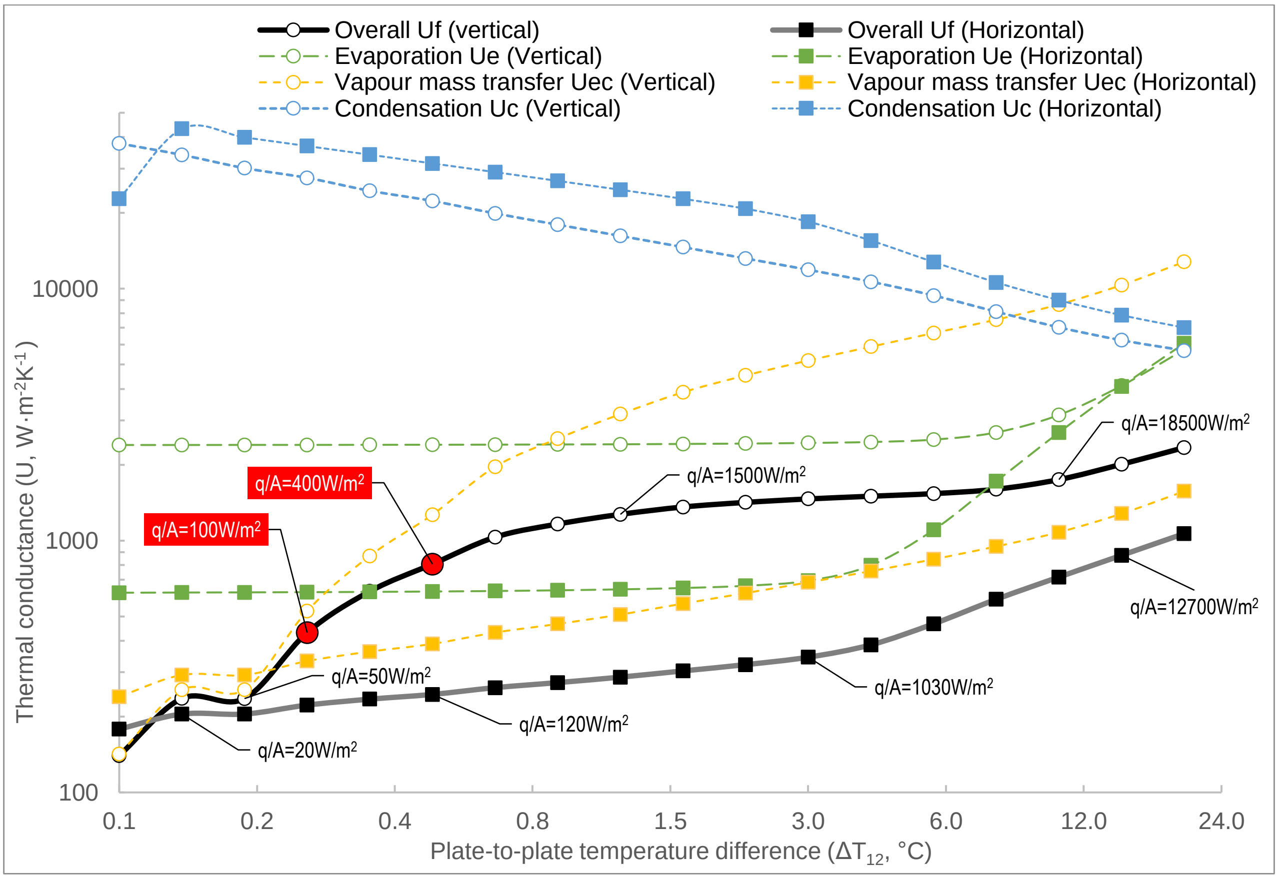

Figure 15 – Dependence of forward mode thermal conductance upon plate-to-plate temperature difference (for x = 0.075, y = 0.75, z = 1.5m stainless steel PLVTD at fixed T_2 = 45°C condenser temperature)

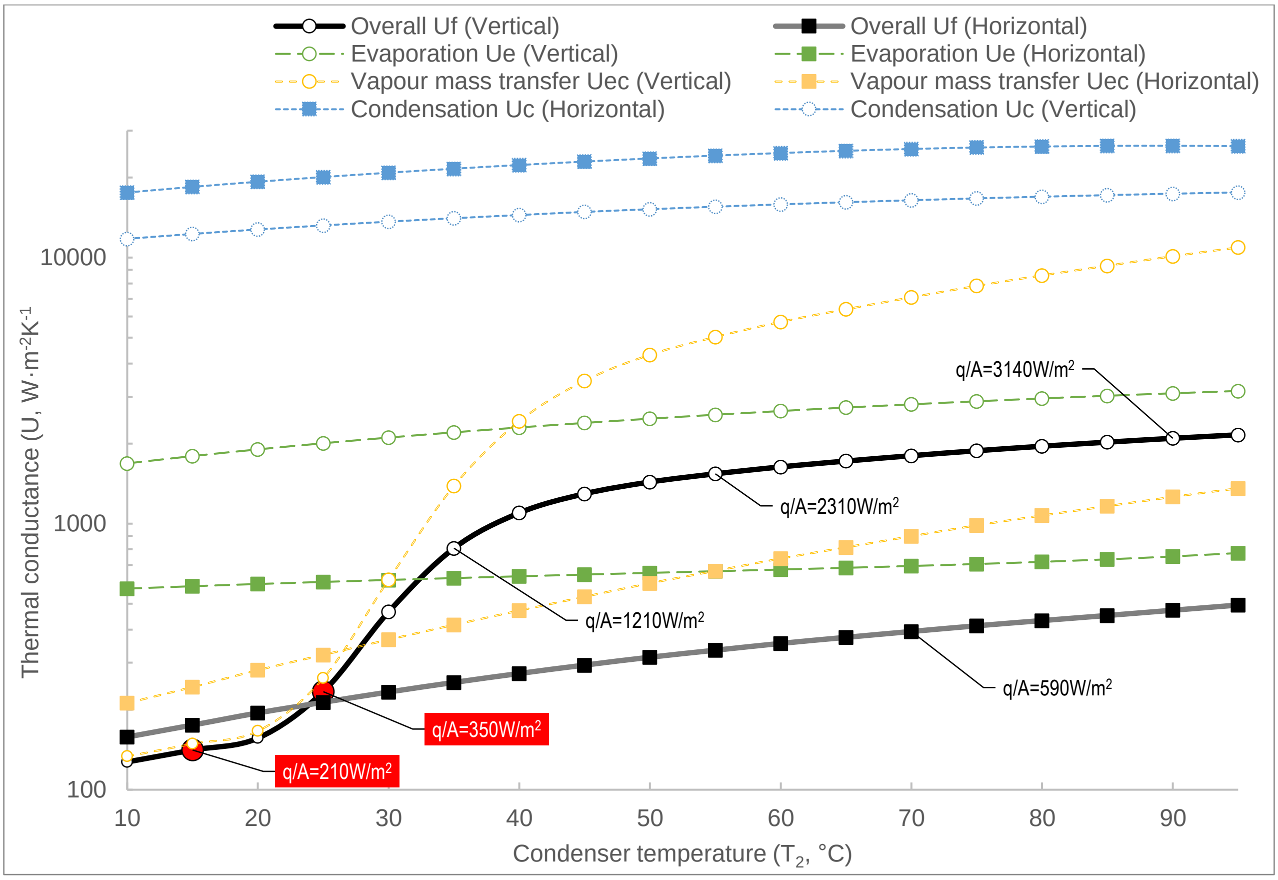

Figure 16 – Dependence of forward mode thermal conductance upon condenser temperature (for x = 0.075, y = 0.75, z = 1.5m stainless steel PLVTD at fixed ΔT_{12} = 1.5°C plate-to-plate temperature difference)

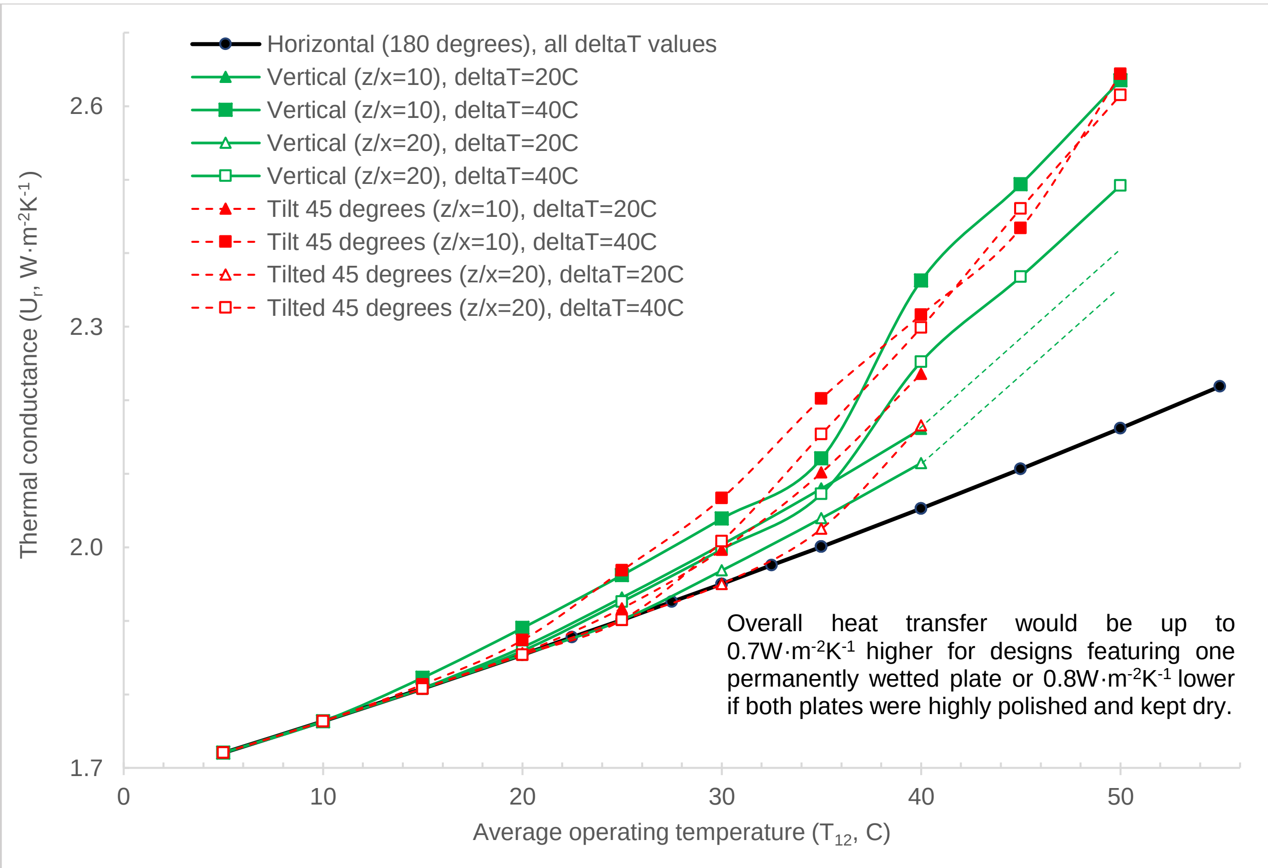

Figure 17 – Reverse mode temperature and heat flux dependence for x=0.075, y=0.75, z=1.5m stainless steel PLVTD

5 Realisation and testing of the large-scale prototype

A large-scale prototype PLVTD (x=70mm, y=700mm and z=1400mm) was designed, fabricated and tested as an integral part of a novel PVT-PLVTD-ICSSWH hybrid solar collector. Pugsley et al. (2016 & 2017) and by Smyth (2019) describe the device and present results of initial tests focused on characterization of the solar energy collection behaviour. Two further papers are currently under peer-review for anticipated publication in Solar Energy journal. The present paper provides detailed analysis concerning the forward and reverse mode behaviour of the PLVTD component.

5.1 Description of the prototype

The prototype PVT-PLVTD-ICSSWH (see Figure 18) consisted of: 1) Removable Transparent acrylic cover to minimise solar absorber heat loss; 2) Solar absorber formed of quartered crystalline silicon photovoltaic cells covered by 2mm transparent acrylic pieces bonded to the matt black painted PLVTD evaporator plate using transparent silicone resin; 3) Stainless steel PLVTD constructed of 0.9mm plates and sidewalls with tubular internal support struts and a falling film evaporator; 4) Hot water storage tank (100L capacity) formed of a 4-sided rectangular box welded to the PLVTD condenser plate and insulated externally with polystyrene foam (150mm thick). Further details of the PLVTD are shown on Figure 19 including the evaporator wetting mechanism and the arrangement of the thermal break incorporated to separate the working fluid reservoir from the condenser plate (to reduce unwanted heat transfer through $R_{L,V}$). The evaporator wetting system consisted of a small manifold-mount centrifugal pump fitted to the base of the reservoir with a stainless steel pipe supplying working fluid (M_L/y=0.08 kg·m^{-1} s^{-1} flow rate) to a linear distribution nozzle (of similar to that described in Table 4) located at the head of the evaporator plate. The internal supporting structure of the PLVTD consisted of N_s=190 tubular struts each (x=70mm long, d_s=8mm diameter and d_{sw}=0.9mm wall thickness) spaced d_{ss}=70mm from one another and $d_{sxy}=d_{sxz}=35$mm from sidewalls. After repairing minor envelope vacuum leaks at welded joints, the PLVTD enclosure was evacuated to 0.01 kPa, which removed non-condensable gases and enabled injection of $m_{Lv}=0.9$kg working fluid through an arrangement of valves. Photographs showing the fabrication and initial testing of the PLVTD and water tank are shown in Figure 20.

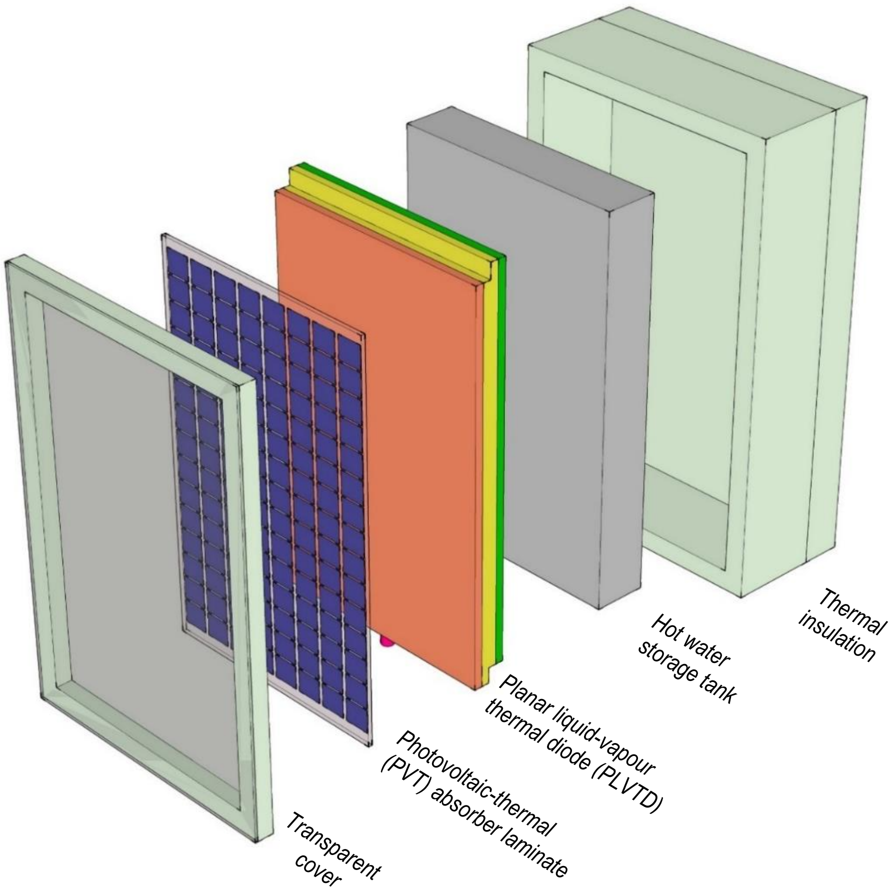

Figure 18 – Key components of the PVT-PLVTD-ICS solar collector prototype

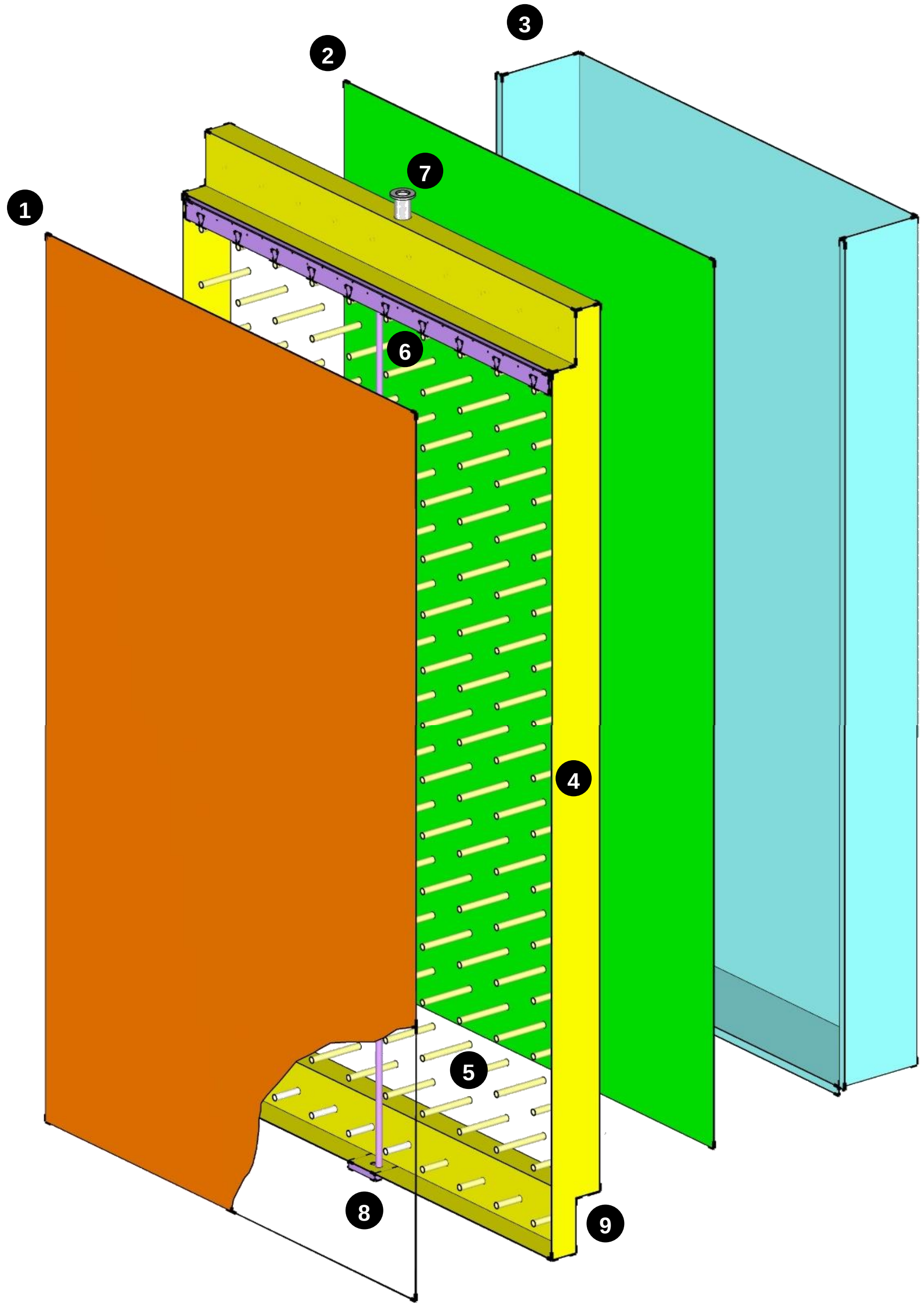

1) Absorber-Evaporator plate (12 thermocouples bonded to front surface to measure temperature T_1)
2) Condenser-tank plate (12 thermocouples bonded to rear surface to measure temperature T_2)
3) Water storage tank back, sides and base (5 submerged thermocouples measuring T_3)
4) Sidewalls forming the top, bottom and sides of the PLVTD envelope
5) Array of tubular struts forming internal structure
6) Evaporator wetter distributer and diffuser nozzle
7) Spigot for vacuum pump connection and working fluid injection
8) Evaporator wetter pump mounting plate
9) Working fluid reservoir with thermal break separating from condenser plate (3 thermocouples bonded to base to measure T_L)
10) Insulation around tank and sides of PLVTD (omitted from illustration for clarity)

Figure 19 – Exploded view of the PLVTD and water tank

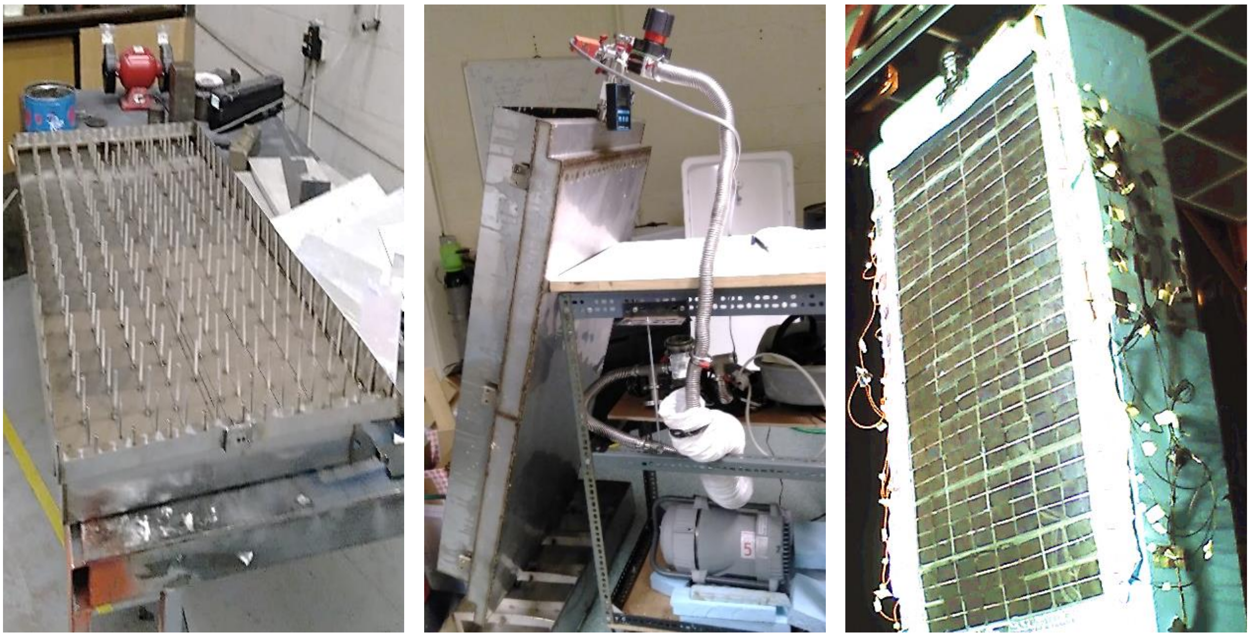

Figure 20 – Photographs of steelwork fabrication (a); leak testing (b); prototype complete with PV/T absorber surface and insulation (c)

5.2 Experimental methodology

The experimental methodology largely follows the precedents set by Smyth et al. (2015b & 2019) whereby the PVT-PLVTD-ICSSWH prototype is exposed to constant vertical plane solar irradiance for 6 hours to simulate a daytime solar heat collection period and is then left to cool overnight for 18 hours. Details of the experimental procedure are described thoroughly by Pugsley et al. (2016 and 2017). The prototype was fitted with 50 thermocouples (details as per Table 4, locations as per Figure 19) to enable spatial temperature variations throughout the various components to be monitored. Approximately half of the thermocouples were bonded to the outer surfaces of the PLVTD to measure evaporator and condenser plate temperatures (T_1 and T_2) and the working fluid liquid temperature (T_L). These thermocouples were covered by foam strips to shield them from unintended influences such as incident solar radiation on T_1 and direct contact with convecting water at T_2. Most of the remaining thermocouples were submerged in the water tank to measure the thermal store temperature (T_3) or distributed around the prototype to measure local ambient temperatures (T_a). All thermocouples were connected to a datalogger (Delta-T devices DL2e) which was configured to monitor continuously and record average temperatures at 5 minute intervals. Initial tests were undertaken to determine thermal conductance of the insulated water storage tank and PLVTD sidewalls by covering the evaporator plate with 300mm of insulation, filling the tank with water at 70°C, and measuring the time taken to cool to T_a=23°C room temperature. Measurement results suggested residual heat loss of U_{3a}=1.1W·m^{-2}·K^{-1} over an area of A_{3a}=2.3m^2 decreasing with time to U_{3a}=0.6W·m^{-2}·K^{-1} as the tank temperature reduced towards ambient. After removing the 300mm insulation, the prototype was then positioned in front of a large vertically oriented solar simulator (Zacharopoulos et al., 2009) and measurements of solar irradiance across the absorber-evaporator plate were made for several different light source setpoints (G=870, 610 and 370W·m^{-2} with ±10% uniformity over the whole surface) using a calibrated pyranometer (Kipp & Zonen CM4). Multiday tests were then undertaken with the prototype exposed to each irradiance setpoint for several consecutive days. One multiday test (see time history on Figure 24) was undertaken with the transparent cover in place but the majority (Figures 21 to 23) were undertaken with it removed. The storage tank temperature (T_3) change with time (t) was used to calculate the instantaneous thermal power (q_3) and hence the instantaneous heat flux through the thermal diode (q_{12}/A_p according to Equation 24) allowing for PLVTD surface area (A_p=0.98m^2), specific heat capacity of water (c_p=4180 J·kg^{-1}·K^{-1}) and the mass of water contained in the tank (m_3=100kg).

$$\frac{q_{12}}{A_p} = \frac{q_3}{A_p} = \frac{m_3\, c_p\, \Delta T_3}{A_p\, \Delta t} \qquad \textbf{Equation 24}$$

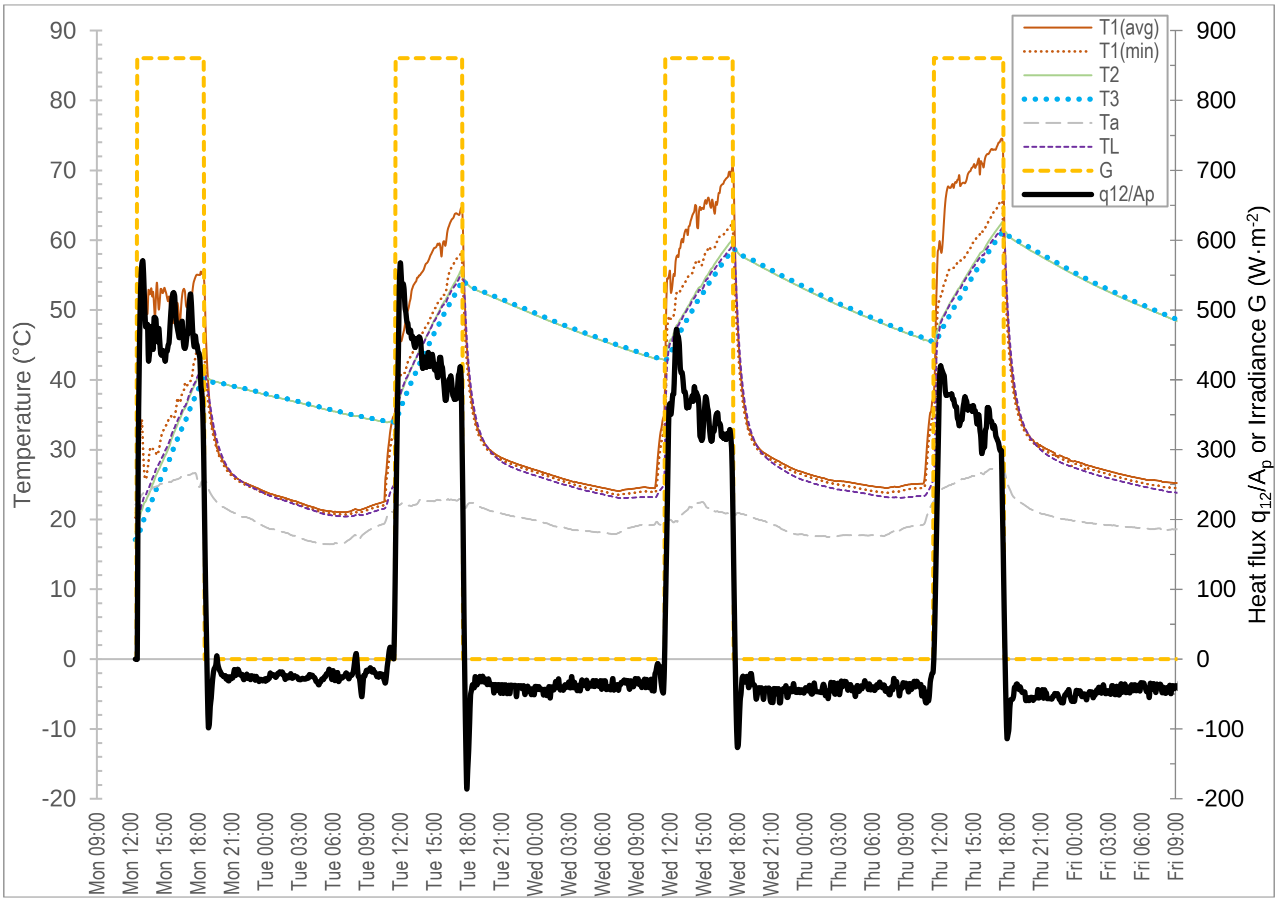

Figure 21 – Temperature and heat flux time history results for tests under high irradiance without absorber transparent cover

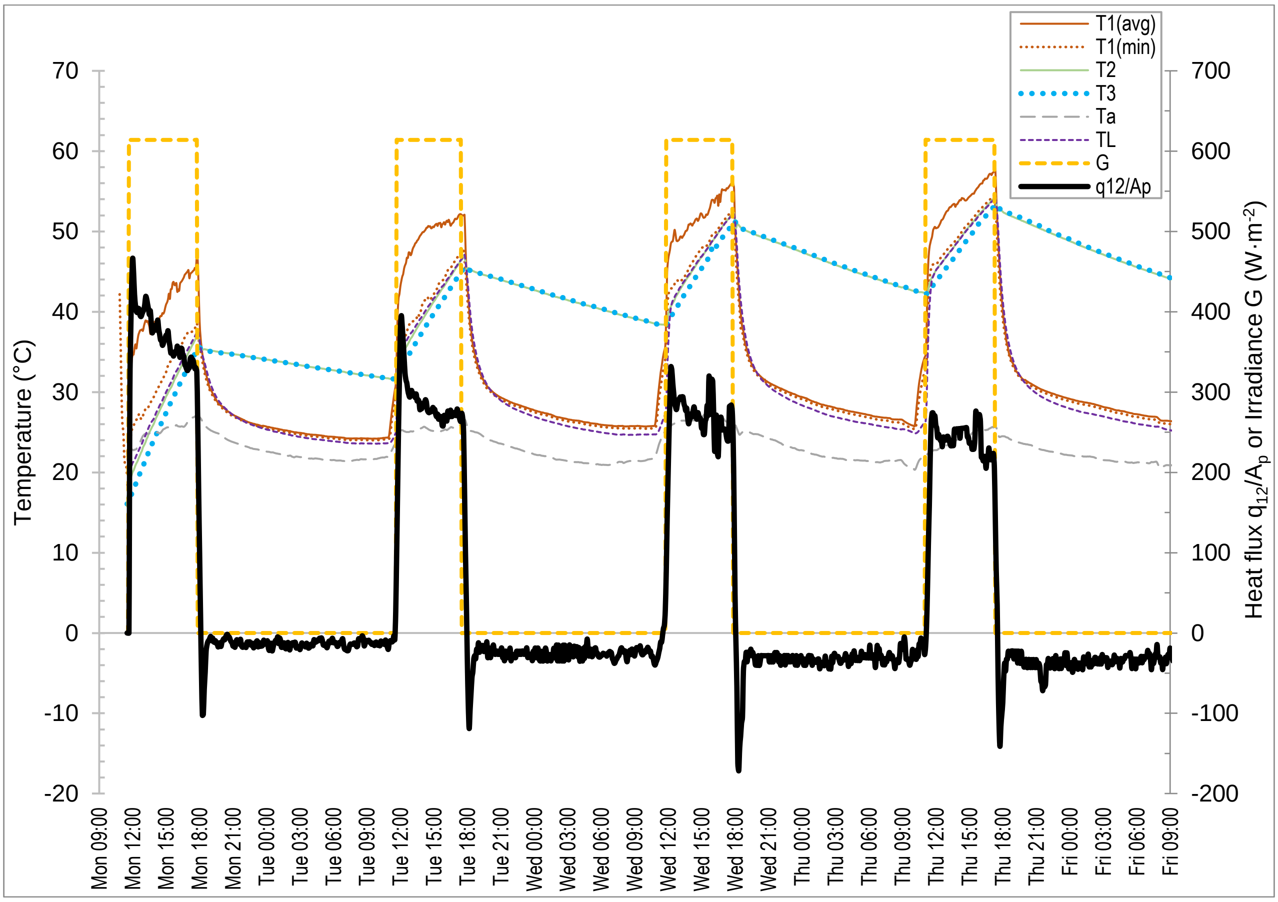

Figure 22 – Temperature and heat flux time history results for tests under medium irradiance without absorber transparent cover

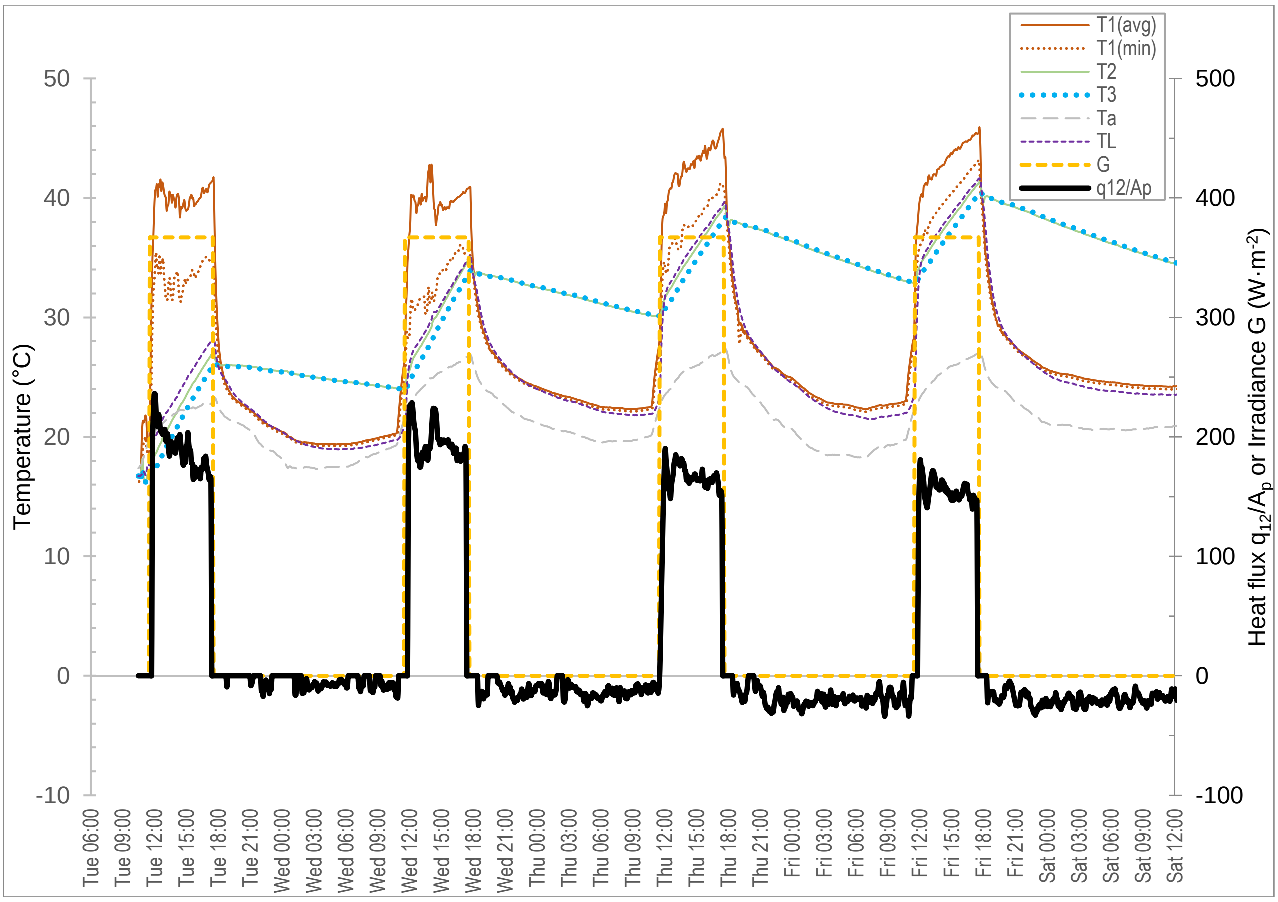

Figure 23 – Temperature and heat flux time history results for tests under low irradiance without absorber transparent cover

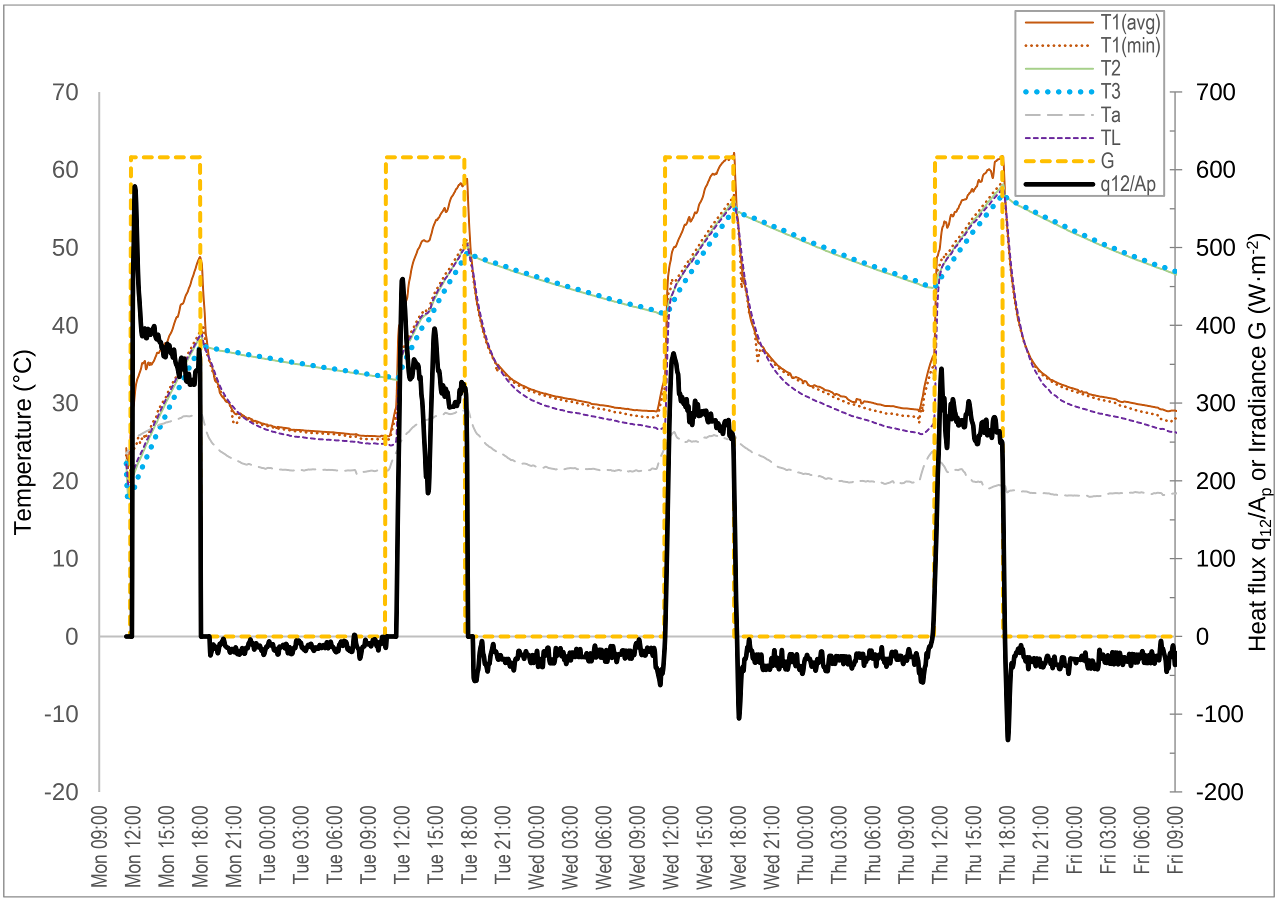

Figure 24 – Temperature and heat flux time history results for tests under medium irradiance with absorber transparent cover

5.3 Results

The PLVTD's diodic behaviour is evident on Figures 21 to 24. Forward mode occurs when the prototype is exposed to irradiance (G) which causes the absorber-evaporator plate temperature (T_1) to rise and for heat flux ($50<q_{12}/A_p<600$ W·m^{-2}) to be transmitted to the condenser-tank plate (T_2) across the plate-to-plate temperature difference ($3<\Delta T_{12}<30$°C) causing a steady increase in water storage tank temperature (T_3). Reverse mode occurs when irradiance ceases (G=0) causing the absorber-evaporator plate temperature to fall below that of the condenser-tank plate ($5<-\Delta T_{12}<25$°C) and for a steady heat loss flux ($15<-q_{12}/A_p<60$ W·m^{-2}) to develop causing a steady decrease in T_3. Distinct transients are apparent on Figures 21, 22 and 24 (medium and high irradiance tests) during forward-to-reverse mode switching which causes temporarily high heat loss fluxes (up to $-q_{12}/A_p\approx150$W·m^{-2}) to occur immediately following each solar simulator switch-off event. These transients are caused by unwanted reverse mode latent heat transfer which occurs when residual liquid on the condenser-tank plate flashes off causing vapour to flow across the cavity and condense on the absorber-evaporator plate. The phenomenon is typically sustained for about half an hour at a steadily decreasing rate until the condenser-tank plate eventually becomes dry causing latent heat transfer to cease.

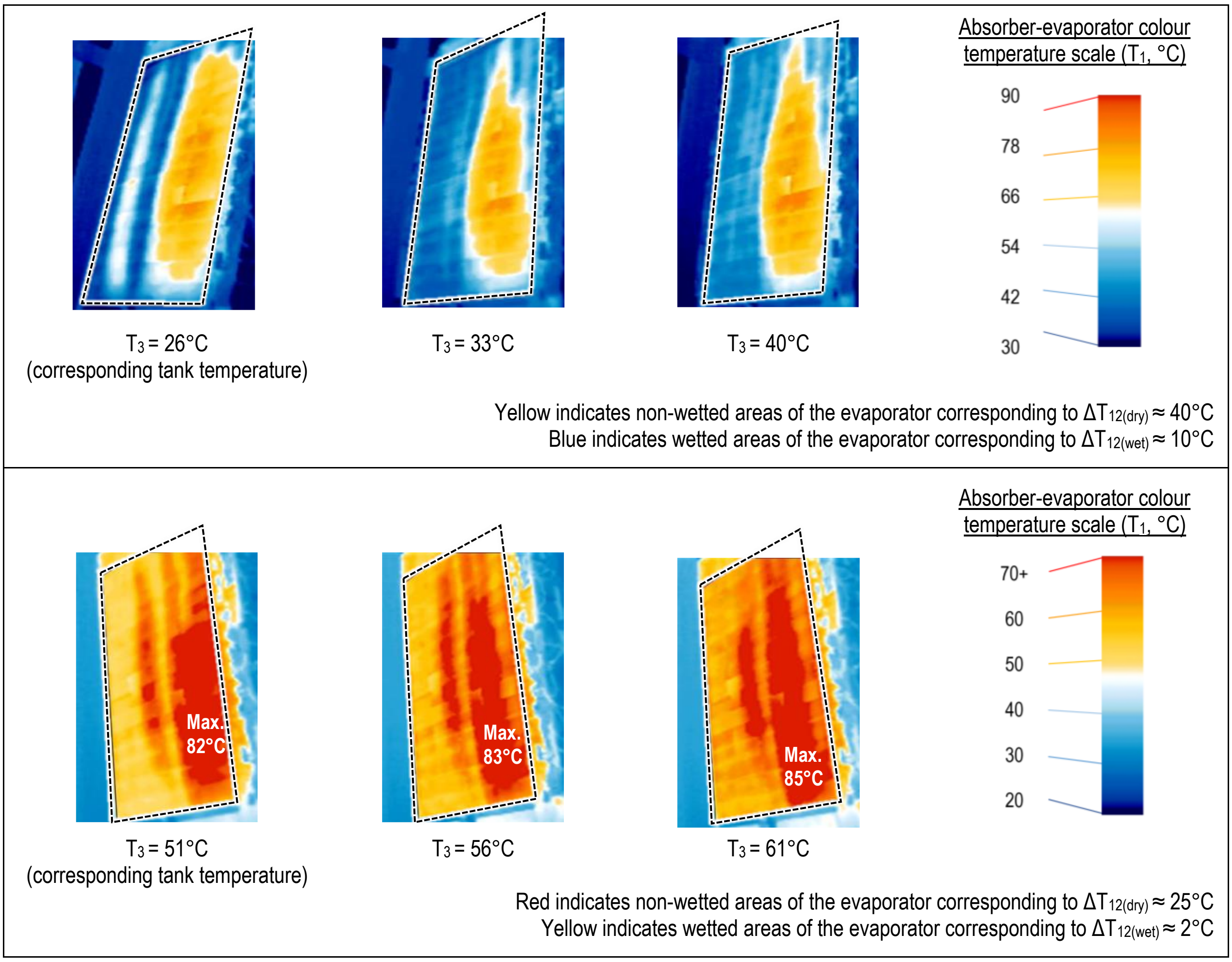

Figure 25 – Infrared thermographic images of the absorber-evaporator plate during high irradiance tests

A thermographic camera (Testo 875-1i) was used to evaluate absorber-evaporator plate temperature uniformity (see Figure 25) with the primary aim of ascertaining the effectiveness of the evaporator wetting mechanism. During forward mode operation, dry areas of the evaporator will be much hotter than the wetted areas owing to lack of latent heat removal. Image analysis using specialist software (Testo SuperResolution) enabled wetted proportions of the evaporator ($A\%_{wet}$) to be estimated. Only ~10% appears to be fully wetted at low temperatures ($T_3 \approx 15°C$) but this increases to ~75% at $T_3 \approx 45°C$, seemingly due to improved spreading/adhesion to the evaporator surface as fluid viscosity and surface tension reduce with increasing temperature. Evaporator dry-out was observed to occur during high temperature and high irradiance conditions, seemingly caused by evaporator wetter pump malfunction (audible noise and reduced current draw). Possible reasons for the malfunction include cavitation (fluid vapourising on the pump impeller) and lack of liquid in the working fluid reservoir (more fluid exists as vapour when operating at high temperatures). Detailed inspection of >100 thermographic images (Pugsley, 2017) suggests that the degree of apparent evaporator wetting correlates reasonably well with the condenser temperature according to the relation $A\%_{wet} \approx -0.086(\mathrm{T}_2)^2 + 7.2(\mathrm{T}_2) - 80$ (valid for $15<T_2<65$). Wetted region temperatures (Figure 25) typically correspond to minimum absorber-evaporator plate temperatures recorded by the datalogged thermocouples ($T_{1(min)}$ on Figures 21-24). Reverse mode thermal conductances (U_r) are presented on Figure 26 with reference to average PLVTD operating temperature $T_{12}=(T_{1(avg)}+T_2)/2$. Reported results are raw datapoints calculated using Equations 1 and 23 with plate-to-plate temperature difference derived from plate spatial averages ($\Delta T_{12}=T_{1(avg)}-T_2$). Measured results for quasi-steady state conditions (typically $U_r \approx 1.6 W \cdot m^{-2}K^{-1}$ at low temperatures increasing to $U_r \approx 1.9 W \cdot m^{-2}K^{-1}$ at high temperatures) are very similar to model predictions ($1.7<U_r<2.5$ $W \cdot m^{-2}K^{-1}$ on Figure 17). Forward-to-reverse mode switching transients caused by the abrupt loss of input heat flux associated with solar simulator switch-off are clearly apparent on Figure 26 as vertical steaks with magnitudes in the range $0.5<U_r<278 W \cdot m^{-2}K^{-1}$ which have been excluded from the quasi-steady state dataset. These transients illustrate the PLVTD’s forward-to-reverse mode switching behaviour whereby the flashing of residual condensate temporarily causes unwanted latent heat transfer in the reverse direction until condenser dry-out occurs and reverse mode heat transfer behaviour reaches the quasi-steady state (typically after a period of between 30 and 90 minutes).

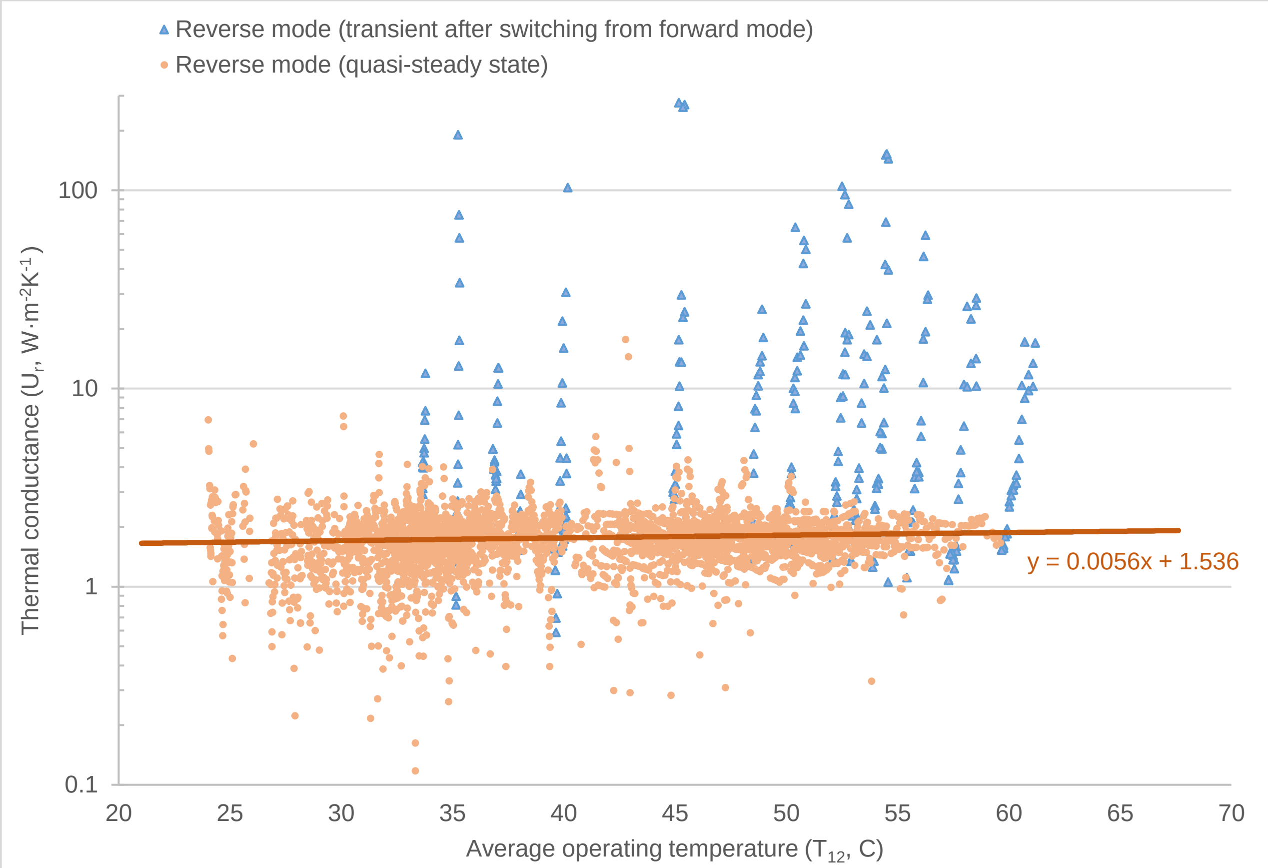

Figure 26 – Thermal conductances across the PLVTD in reverse mode

Forward mode thermal conductance measurement results (U_f) are presented on Figure 27 and compared to four example predictions from the model (red datapoints which corresponding directly to red datapoints highlighted on Figures 15 & 16). Measured thermal conductances would have ideally been derived according to Equations 1 and 24 based on the measured thermal power flowing through the PLVTD (q_{12}), the average plate-to-plate temperature difference ($\Delta T_{12}=T_1-T_2$), and the overall PLVTD plate area (A_p), as was the case for the reverse mode results reported on Figure 26. However, owing to aforementioned issues concerning non-uniform evaporator wetting, the forward mode results reported on Figure 27 have been calculated based on the minimum plate-to-plate temperature difference $\Delta T_{12(min)}=T_{1(min)}-T_2$ and the estimated heat transfer area $A_p{\cdot}A\%_{wet}$ (estimated using the $A\%_{wet} \approx -0.086(T_2)^2 + 7.2(T_2) - 80$ relation determined from the thermographic analysis) to enable non-wetted parts of the evaporator to effectively be ignored. Owing to significant scatter in the dataset, and the inherent limited ability to exert independent control over PLVTD heat flux and plate temperatures during solar simulator tests, thermal conductances have been reported as group average values calculated by sorting the dataset into $q_{12}/A_p \pm 50 W \cdot m^{-2}$ and $T_2 \pm 3°C$ bins (as denoted by the horizontal bars on Figure 27) enabling trends to be identified.

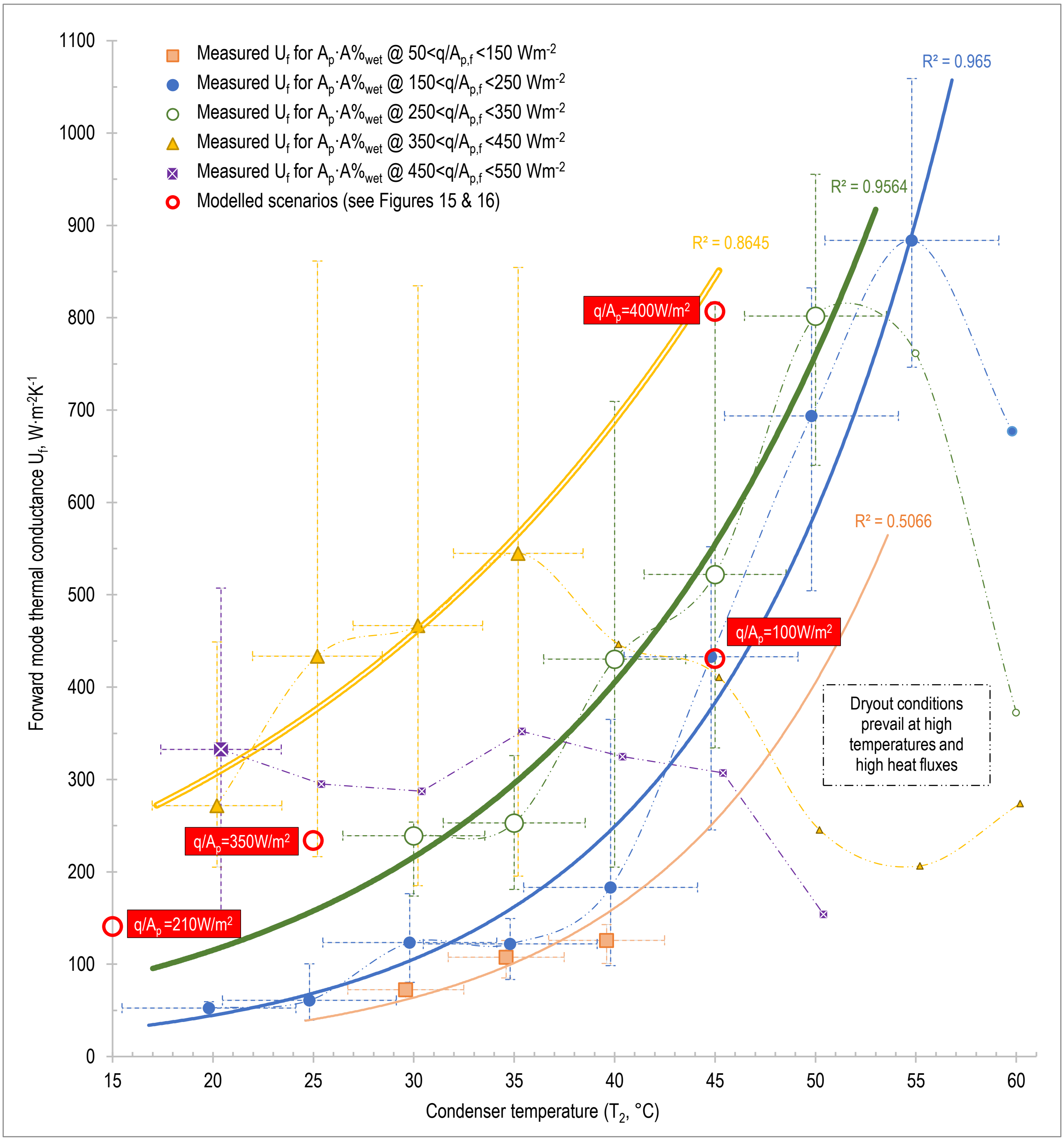

Figure 27 – Measured forward mode thermal conductances (wetted areas only) compared to four modelled operating scenarios

Thermal conductances increase from $U_f \approx 50$ W·m^{-2}K^{-1} at low temperatures and low heat fluxes up to $U_f \approx 900$ W·m^{-2}K^{-1} at the highest reliably measurable temperatures and heat fluxes. Results for $T_2 > 55$°C at $q_{12}/A_p > 200$W·m^{-2}, $T_2 > 50$°C at $q_{12}/A_p > 300$W·m^{-2}, $T_2 > 35$°C at $q_{12}/A_p > 400$W·m^{-2}, and almost all data for $q_{12}/A_p > 500$W·m^{-2} were affected by evaporator dry-out and are therefore excluded from calculated trends. Comparison with the four modelled datapoints indicates good correspondence at $T_2 = 45$°C for $q_{12}/A_p = 350$W/m^2, $T_2 = 25$°C for $q_{12}/A_p = 400$W/m^2 and $T_2 = 25$°C for $q_{12}/A_p = 210$W/m^2 but suggests the prototype performs worse than expected at $T_2 = 45$°C for $q_{12}/A_p = 100$W/m^2. The model suggests that performance at low temperatures and low heat fluxes is determined primarily by vapour mass flow dynamics (thermal resistance R_{ec}) which may have been adversely affected by evaporator plate temperature non-uniformities (see Figure 25). It must be remembered that results reported on Figure 27 represent thermal conductances associated with wetted areas of the evaporator only. Calculated true overall forward mode performances evaluated for the whole PLVTD plate area (A_p, inclusive of non-wetted parts of the evaporator) typically ranged from $U_f \approx 10$W·m^{-2}K^{-1} at low temperatures up to $U_f \approx 85$W·m^{-2}K^{-1} at high temperatures as reported by Pugsley et al. (2016 and 2017).

Trends exhibited by the measured thermal conductances are summarised on Figure 28 along with the corresponding diodicities (calculated according to Equation 2). Maximum diodicity occurs at the highest condenser temperatures ($\varsigma = 99.9\%$ at $T_2 = 60$°C) where it is largely independent of heat flux. Diodicity is reduced at lower temperatures and exhibits strong dependency upon the forward mode heat flux such that relatively high diodicity ($\varsigma = 99.5\%$ at $T_2 = 20$°C) is maintained at $q/A \approx 400$ W·m^{-2} but this is significantly reduced ($\varsigma = 88.2\%$ at $T_2 = 20$°C) at $q/A \approx 100$ W·m^{-2}. The suggested targets of $\varsigma > 97\%$ for CCBE applications and $\varsigma > 99\%$ for BISTS/BIPV applications (refer to Section 2.2) appear to be achievable provided that the intended heating temperature is high enough ($T_2 > 25$°C for CCBE and $T_2 > 40$°C for BISTS) and available heat flux is q/A>250 W·m^{-2}, as would typically be the case. The aforementioned diodicities were calculated with reference to the forward mode thermal conductances for wetted areas of the evaporator only in order to represent what would occur in a PLVTD with uniform evaporator wetting. Calculated diodicites are notably lower (ς=72.5% at T_2=20°C, rising to ς=95.7% at T_2=60°C) when non-wetted parts of the evaporator are accounted for, which highlights the importance of ensuring uniform evaporator wetting.

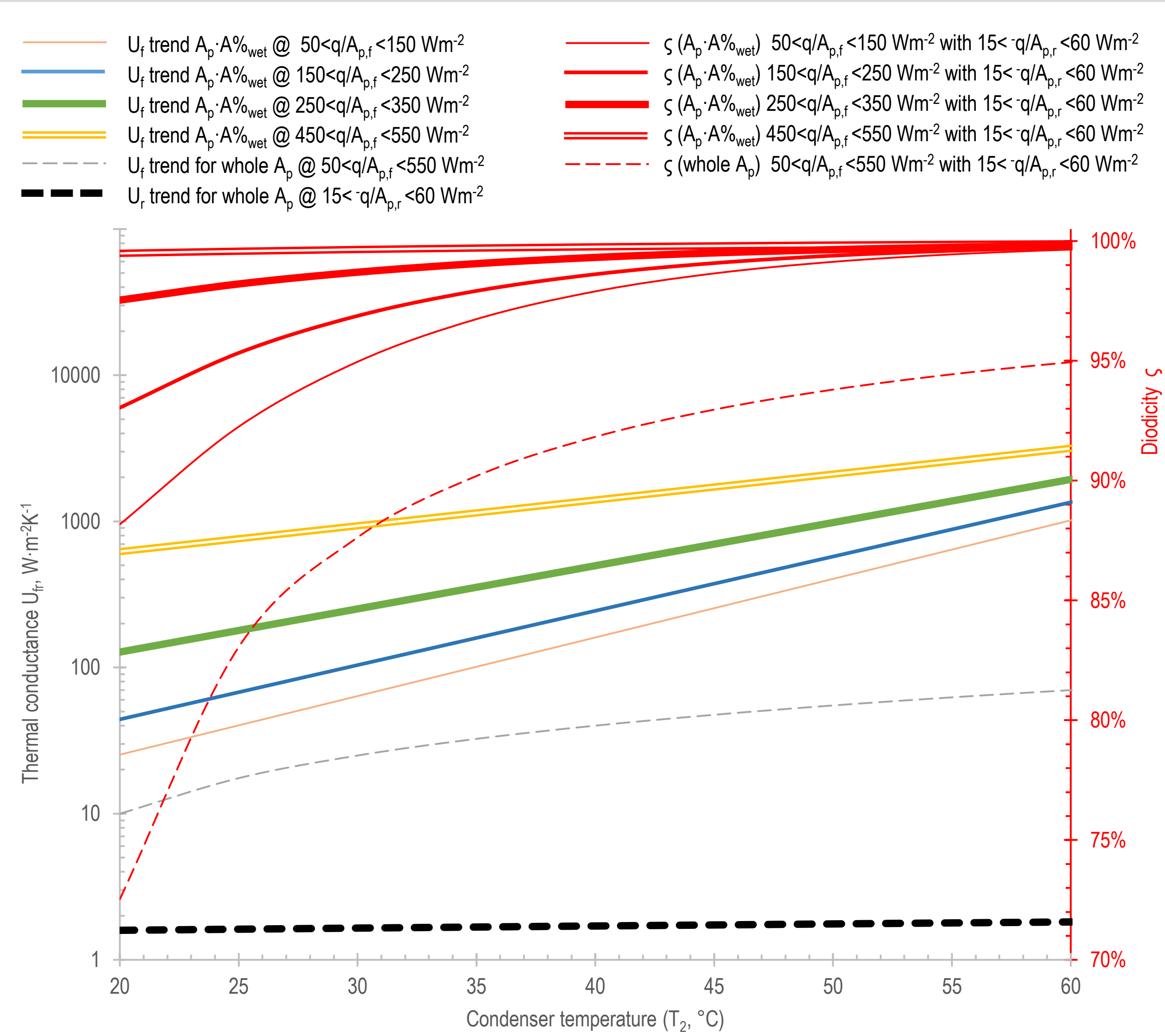

Figure 28 – Trends of measured thermal conductances and corresponding diodicity

5.4 Future improvements

Future PLVTD design development could investigate the use of superhydrophillic evaporator surfaces (Boreyko and Chen, 2013) or capillary wicks (Souliotis et al., 2011; Muhumuza et al., 2019), together with nozzle design and flow rate optimization to improve wetting uniformity. The large stainless steel PLVTD suffered more problems with wetting uniformity than the initial smaller aluminium prototype, partly because the wetter nozzle was difficult to fabricate accurately at a larger size (aperture width varied along the length and was wider than intended in several places) but also perhaps due to differing evaporator surface hydrophillicities. Preliminary investigations on evaporator wetter flow rates reported by Pugsley (2017) suggested that doubling M_L/y from 0.08 to 0.16 $kg{\cdot}m^{-1}\,s^{-1}$ more than doubled U_f in a stainless steel PLVTD with poor wetting uniformity, and likewise, halving to $M_L/y=0.04$ $kg{\cdot}m^{-1}\,s^{-1}$ reduced U_f by ~50%. The effect was less significant for the PLVTD with a uniformly wetted aluminium evaporator where varying flow rate in the range $0.03<M_L/y<0.07 kg{\cdot}m^{-1}\,s^{-1}$ influenced U_f by only ±25% relative to the $M_L/y=0.05 kg{\cdot}m^{-1}\,s^{-1}$ baseline. It may be possible to eliminate the need for a wetter pump (and its associated parasitic power needs) by employing a suitable capillary wick, thereby making the vertical PLVTD an entirely passive device akin to the horizontal PLVTD investigated Pugsley et al. (2019). A suitable wick would need to achieve capillary lift across the full height of the evaporator at a flow rate sufficient to prevent dry-out. This may necessitate reduction of evaporator plate height (z) which would also affect PLVTD aspect ratios. The model suggests that increasing cavity depth (x) improves reverse mode performance by increasing thermal resistances R_v, R_w and R_s whilst also improving forward mode performance by decreasing R_{ec}. However, reducing aspect ratio (z/x) to make the PLVTD less slender has the opposite effect. Future PLVTD research and development should investigate transient behaviour in more detail. It should be possible to reduce unwanted reverse mode latent heat transfer (transients occurring after forward-to-reverse mode switching) by increasing condenser plate hydrophobicity (coatings or surface treatments) to minimise the amount of residual condensate clinging to the plate surface. Results also indicate a degree of performance lag during reverse-to-forward mode switching which is probably associated with the thermal masses (evaporator plate and working fluid) that must be heated to enable evaporation to occur. Total thermal mass can be reduced by minimizing evaporator plate thickness (x_{pe}), minimizing the amount of vapour contained in the cavity (m_v) and minimizing the amount of liquid held in the working fluid reservoir (m_L). Unfortunately, each of these approaches have knock-on effects on other PLVTD design aspects. For example, reducing x_{pe} will reduce plate strength and increase requirements for internal structural support (reduced d_{ss} and increased N_s) resulting in worsened U_s thermal bridging. Reducing m_v requires cavity dimensions (particularly x) to be minimized which impairs reverse mode performance. The degree to which m_L can be reduced is constrained by the need to avoid dry-out during high temperature operation (ie when m_v is highest). The small aluminium PLVTD which contained $m_{Lv}/yz=1.7kg/m^2$ suffered fewer dry-out problems than the larger stainless steel PLVTD which contained only $m_{Lv}/yz=0.9kg/m^2$. Investigations by Pugsley (2017) found that increasing working fluid quantity to $m_{Lv}/yz=1.1kg/m^2$ in the stainless steel PLVTD reduced occurrence of pump malfunction and apparent evaporator dry-out.

6 Conclusions

Theoretical and experimental investigations were undertaken to examine behaviour of a vertical Planar Liquid Vapour Thermal Diode (PLVTD) with a pumped falling film evaporator wetter and its application in Climate Control Building Envelopes (CCBE) and Integrated Collector-Storage Solar Water Heaters (ICSSWH).

- **Theoretical model development:** The horizontal PLVTD model proposed by Pugsley et al. (2019) was augmented by introducing falling film evaporation and condensation, vapour convection in vertical and tilted rectangular enclosures, an iteration methodology for evaluating working fluid temperatures, and expressions accounting for non-condensable gas effects.

- **Model validation for vertical orientation scenarios:** Forward and reverse mode thermal conductances of a small (A_p=0.15m^2 x=22mm) vertical aluminium PLVTD were measured and compared against model predictions. The model predicts reverse mode performance accurately (U_r=12W·m^{-2}K^{-1}) across the range of operating conditions tested (ΔT_{12}=20°C and 25<T_2<65°C) and also reliably predicts forward mode performance (U_f≈400 W·m^{-2}K^{-1}) for heat fluxes and condenser temperatures (T_2=33±4°C and 200<q/A<1000 W·m^{-2} corresponding to 0.5<ΔT_{12}<2.5°C) in the range of interested for CCBE and ICSSWH applications. The trend for proportionally increasing conductance (175<U_f<730 W·m^{-2}K^{-1}) with increasing temperature (15<T_2<60°C for fixed ΔT_{12}=4.5±1.5°C) is successfully predicted and appears to be related to vapour viscosity and its influence on the working fluid vapour flow resistance (R_{ec}). The highest recorded thermal conductance was U_f≈1200 W·m^{-2}K^{-1} at T_2≈55°C with ΔT_{12}≈2.2°C corresponding to q_{HC}/A_p≈2800 W·m^{-2}.
- **Model interrogation examining parametric design influences:** The influence of PLVTD parametric design variables such as dimensions, orientation, temperature and heat flux was examined. Vertical PLVTDs achieve lower vapour convection thermal resistances (R_v and R_{ec}) than horizontal PLVTDs giving them worse reverse and better forward mode performances, especially when cavity depths are large (x>50mm, q/A>50W/m^2, T_2>25°C). Reverse mode performance is sensitive to cavity depth, especially when the cavity is small (x<40mm) and behaviour is dominated by gaseous conduction and thermal bridging through sidewalls/structure. Forward mode performance depends on temperature, heat flux and dimensions, with high temperatures, high heat

fluxes, large cavity depths ($x \approx 150$mm) and high aspect ratios ($z/x>10$) being generally preferable for vertical and tilted PLVTDs.

- **Testing of a large PLVTD integrated into a solar collector:** The model was used to develop the design of a large-scale prototype PLVTD ($A_p=0.98$m^2 and $x=70$mm) which was fabricated from 0.9mm stainless steel sheet and integrated into a novel PLVTD-ICSSWH hybrid solar collector with 100L water storage tank. Multiday tests consisting of consecutive 6-hour heating and 18-hour cooling cycles using a solar simulator ($G=870$, 610 and 370W·m^{-2}) were undertaken to characterise PLVTD behaviour under quasi-steady heat fluxes of $50<q/A<600$ W·m^{-2} in forward mode ($3<\Delta T_{12}<30$°C) and $15<-q/A<60$W·m^{-2} in reverse mode ($5<-\Delta T_{12}<25$°C) for condenser temperatures ranging from $15<T_2<60$°C. Reverse mode thermal conductances increased slightly with increasing temperature in the range $1.6<U_r<1.9$W·m^{-2}K^{-1} as predicted by the model. Transient heat loss fluxes (up to $-q/A \approx 150$W·m^{-2}) were observed during forward-to-reverse mode switching representing unintended reverse mode latent heat transfer associated with flashing of residual condensate. Forward mode thermal conductances (considering wetted parts of the evaporator only) ranged from $U_f \approx 50$ W·m^{-2}K^{-1} (at $T_2=20$°C and $q/A<100$ W·m^{-2}) up to $U_f \approx 900$ W·m^{-2}K^{-1} at higher temperatures and heat fluxes. Most results were in good agreement with the modelling predictions. Non-uniform evaporator wetting was observed to be problematic, especially at low temperatures. Evaporator dry-out occurred under certain conditions (notably for $q_{12}/A_p>500$W·m^{-2} and $T_2>55$°C). Provided that uniform evaporator wetting can be accomplished, results indicate that target diodicities ($\varsigma>97\%$ for CCBE and $\varsigma>99\%$ for BISTS/BIPV applications) can be achieved during operation at relevant temperatures and heat fluxes.

It is anticipated that study findings, together with subsequent research inspired by the proposed parametric design approach, will have significant impacts in the context of the climate crisis by enabling development of new components and systems for Net Zero Energy Buildings. Future PLVTD design development work should target improvements in evaporator wetting (eg superhydrophillic surfaces, capillary wicks, wetter nozzle design, and flow rate optimization) and dimensional optimizations with regard to real-life application scenarios. Further research investigating the transient behaviour of PLVTDs should be undertaken with the aim of quantifying and reducing unwanted transient effects associated with thermal mass (eg superhydrophobic condensers, optimization of working fluid quantity and cavity depth).

Acknowledgements

This research was enabled in its early stages by studentship funding support from the Northern Ireland Department for the Economy. The work was subsequently progressed with funding support from SolaForm Ltd and was completed as part of the "SolaNetwork" project funded by the UKRI Engineering and Physical Sciences Research Council (EP/T004819/1). The authors would also like to thank networking support funded by the European Union FP7 COST Action TU1205 "Building Integration of Solar Thermal Systems" and for the helpful contributions of reviewers prior to publication.

Nomenclature

Latin symbols

A	Surface area [m^2]
$A\%_{wet}$	Percentage of evaporator plate wetted by working fluid
c_p	Specific heat capacity at constant pressure [$J\cdot kg^{-1}\, K^{-1}$]
d	Distance [m]
D	Mass diffusivity [$m^2\cdot s^{-1}$]
g	Acceleration due to gravity (g=9.81$m\cdot s^{-2}$ on earth at sea level)
G	Solar irradiance [$W\cdot m^{-2}$]
h_{Lv}	Latent heat of liquid-vapour phase change [$J\cdot kg^{-1}$]

k	Thermal conductivity [$W \cdot m^{-1} K^{-1}$]
k^*	Complex thermal conductivity with sensible & latent components [$W \cdot m^{-1} K^{-1}$]
K_{sf}	Nucleate boiling surface constant
L	Characteristic dimension of Nusselt number [m]
M	Mass flow rate [$kg \cdot s^{-1}$]
n_{sf}	Nucleate boiling surface exponent
N_S	Number of struts in structural support array
Nu	Nusselt number
P	Pressure [Pa]
Pr	Prandtl number
q	Thermal power [W]
R	Thermal resistance [$K \cdot W^{-1}$]
Ra	Rayleigh number
Ra*	Modified Rayleigh number accounting for pressure-driven vapour flow
Re	Reynolds number
Sc	Schmidt number
t	Time [s]
T	Temperature [°C] except for Equation 10 which uses absolute [K]
U	Thermal conductance or heat transfer coefficient [$W \cdot m^{-2} K^{-1}$]
v	Kinematic viscosity [$m^2 \cdot s^{-1}$]
X	Mole fraction of working fluid in mixture with non-condensable gas
x	Distance along an axis which is parallel to the PLVTD depth [m]
y	Distance along horizontal axis perpendicular to PLVTD depth [m]
z	Distance along an axis which is perpendicular to x and y axes [m]

Greek and other symbols

ε	Emissivity
μ	Dynamic viscosity [$kg \cdot m^{-1} s^{-1}$]
$\mathcal{M}$	Molecular weight [$g \cdot mol^{-1}$]
$\mathcal{R}$	Universal gas constant (8.314 $J \cdot mol^{-1} K^{-1}$)
ϑ	Thermal diffusivity [$m^2 \cdot s^{-1}$]
ΔP	Pressure difference [Pa]
ΔT	Temperature difference [°C]
ς	Diodicity [%]
σ	Surface tension [$N \cdot m^{-1}$]
β	Coefficient of volumetric expansion [K^{-1}]
ρ	Density [$kg \cdot m^{-3}$]
χ	Stefan Boltzmann constant (5.67 x 10^{-8} $Wm^{-2}K^{-4}$)
θ	Tilt angle relative to horizontal [°]

Subscripts

1	Plate 1 which is the evaporator in forward mode
2	Plate 2 which is the condenser on forward mode
3	Thermal storage water tank
12	Between (or average of) the two plates
a	Ambient environment
B	Back of plate
c	Condenser, condensate or condensation

cr	Critical (angle)
C	Cold water feed or cooled return
CH	Cooling plate or cooling water circuit
D	Edge of plate
e	Evaporator, evaporation or evaporator liquid film
ec	Between (or average of) the evaporator and condenser surfaces
f	Forward mode
h	Horizontal orientation
H	Hot water feed or heated return
HC	Heating plate of heated water circuit
L	Working fluid liquid state property
l	Losses to ambient environment
L1	Liquid on the evaporator
L2	Liquid on the condenser
LcS	Liquid working fluid (condensate) flowing from condenser to reservoir (sump)
LSe	Liquid working fluid flowing (pumped) from reservoir (sump) to evaporator
LeS	Liquid working fluid (run-off) flowing from evaporator to reservoir (sump)
Lv	Latent property of working fluid at the liquid-vapour saturation point
LvL	Liquid-vapour-liquid transition
ncg	Non-condensable gas
Nu	Nucleate boiling
p	Plate
r	Reverse mode
R	Radiative component
Ra	Natural convection determined by Rayleigh number
Re	Forced convection determined by Reynolds number
s	Structural element(s) such as internal support struts
sf	Evaporator plate surface condition
ss	Between two adjacent struts (centre-to-centre distance)
sw	Strut tube wall (thickness)
sxy	Between the xy-sidewall and the closest strut (distance along the z-axis)
sxz	Between the xz-sidewall and the closest strut (distance along the y-axis)
trans	Transition Rayleigh number ($Ra_{trans}=5x10^6$)
v	Working fluid vapour state property
V	Vertical orientation
w	Sidewalls of the PLVTD
X	Mixture of working fluid and non-condensable gas
x	In the direction parallel to the PLVTD depth
y	In the direction of the horizontal axis perpendicular to PLVTD depth
z	In the direction of the axis which is perpendicular to x and y axes

References

Agathokleous, R., Barone, G., Buonomano, A., Forzano, C., Kalogirou, S., Palombo, A. (2019). Building façade integrated solar thermal collectors for air heating: experimentation, modelling and applications. Applied Energy 239 (2019) 658–679

Aguilar, F., Aledo, S. Quiles, P. (2016). Experimental study of the solar photovoltaic contribution for the domestic hot water production with heat pumps in dwellings. Applied Thermal Engineering 101, 379–89

Ascione, F., De Masi, R., Rossi, F., Ruggiero, S., Vanoli, G. (2016). Optimisation of building envelope design for nZEBs in Mediterranean climate: Performance analysis of residential case study. Applied Energy 183 (2016) 938-957

Avanessian, T. & Hwang, G. (2018). Thermal diode using controlled capillary in heterogeneous nanopores. International Journal of Heat and Mass Transfer 124 (2018) 201–209

Baïri, A., Zarco-Pernia, E., García de María, J. (2014). A review on natural convection in enclosures for engineering applications. The particular case of the parallelogrammic diode cavity. Applied Thermal Engineering 63 (2014) 304-322

Beausoleil-Morrison, I., Kemery, B., Wills, A., Meister, C. (2019). Design and simulated performance of a solar-thermal system employing seasonal storage for providing the majority of space heating and domestic hot water heating needs to a single-family house in a cold climate. Solar Energy 191 (2019) 57–69

Ben-Abdallah, P and Biehs, S. (2013). Phase-change radiative thermal diode. Applied Physics Letters 103 (19)

Berge, A., Hagentoft, C., Wahlgren, P., Adl-Zarrabi, B. (2015). Effect from a Variable U-Value in Adaptive Building Components with Controlled Internal Air Pressure (6th International Building Physics Conference, IBPC 2015). Energy Procedia 78 (2015) 376–381

Bilardo, M., Fraisse, G., Pailha, M., Fabrizio, E. (2019). Modelling and performance analysis of a new concept of integral collector storage (ICS) with phase change material. Solar Energy 183 (2019) 425–440

Blet, N., Lips, S., Sartre, V. (2017). Heats pipes for temperature homogenization: A literature review. Applied Thermal Engineering 118 (2017) 490–509

Borello, D., Corsini, A., Delibra, G., Evangelisti, S., Micangeli, A. (2012). Experimental and computational investigation of a new solar integrated collector storage system. Applied Energy 97 (2012) 982–989

Boreyko, J. & Chen, C. (2013). Vapor chambers with jumping-drop liquid return from superhydrophobic condensers. International Journal of Heat and Mass Transfer 61 (2013) 409–418

Boreyko, J., Zhao, Y., Chen, C. (2011). Planar jumping-drop thermal diodes. Applied Physics Letters 99, 234105

Buonomano, A., Calise, F., Palombo, A., Vicidomini, M. (2016). BIPVT systems for residential applications: An energy and economic analysis for European climates. Applied Energy 184 (2016) 1411–1431

Calise, F., d'Accadia, M, Figaj, R., Vanoli, L., (2016). A novel solar-assisted heat pump driven by photovoltaic/thermal collectors: Dynamic simulation and thermoeconomic optimization. Energy 95, 346-66

Cengel, Y., Boles, M., (2006). Thermodynamics an Engineering Approach, 5th Edition. McGraw-Hill, New York.

Charisi, S. (2017). The Role of the Building Envelope in Achieving Nearly-Zero Energy Buildings (International Conference on Sustainable Synergies from Buildings to the Urban Scale, SBE16). Procedia Environmental Sciences 38 (2017) 115 – 120

Chen, K., Chailapo, P., Chun, W., Kim, S., Lee, K. (1998). The Dynamic Thermosiphon of a bayonet-type thermal diode. Solar Energy 64 (4–6) 257–263

Chen (2012). Patent Application for Thermal Diode Device and Methods. US2012/0012804 Al

Collins, R. & Fischer-Cripps, A. (1991). Design of Support Pillar Arrays in Flat Evacuated Windows. Australian Journal of Physics 1991 (44) 545-63

Corcione (2003). Effects of the thermal boundary conditions at the sidewalls upon natural convection in rectangular enclosures heated from below and cooled from above. International Journal of Thermal Sciences 42 (2003) 199–208.

Cui, H., Overend, M. (2019). A review of heat transfer characteristics of switchable insulation technologies for thermally adaptive building envelopes. Energy & Buildings 199 (2019) 427–444

De Beijer, H. (1998). Product development in solar water heating. Renewable Energy 5 (1998) 201-204

Deng, J., O'Donovan, T., Tianc, Z., King, J., Speake, S. (2019). Thermal performance predictions and tests of a novel type of flat plate solar thermal collectors by integrating with a freeze tolerance solution. Energy Conversion and Management 198 (2019) 111784

Dos Santos Bernardes, M. (2014). Experimental evidence of the working principle of thermal diodes based on thermal stress and thermal contact conductance – Thermal semiconductors. International Journal of Heat and Mass Transfer 73 (2014) 354–357

Drosou, V., Tsekouras, P., Oikonomou, T., Kosmopoulos, P., Karytsas, C. (2014). The HIGH-COMBI project: High solar fraction heating and cooling systems with combination of innovative components and methods. Renewable and Sustainable Energy Reviews 29 (2014) 463–472

Dupeyrat, P., Menezo, C., Rommel, M., Henning, H. (2011). Efficient single glazed flat plate photovoltaic-thermal hybrid collector for domestic hot water systems. Solar Energy 85, 1457-68

Faiman, D., Hazan, H. and Laufer, I. (2001). Reducing the Heat Loss at Night from Solar Water Heaters of the Integrated Collector-Storage Variety. Solar Energy, 71 (2) 87-93

Fang, X. and Xia, L. (2010). Heating performance investigation of a bidirectional partition fluid thermal diode. Renewable Energy 35 (2010) 679–684

Fang, Y., Hyde, T., Arya, F., Hewitt, N., Eames, P., Norton, B., Miller, S. (2014). Indium alloy-sealed vacuum glazing development and context. Renewable and Sustainable Energy Reviews 37 (2014) 480–501

Ganguli, A., Pandit, A., Joshi, J. (2009). CFD simulation of heat transfer in a two-dimensional vertical enclosure. Chemical Engineering Research and Design 87 (2009) 711–27

Garnier, C., Currie, J., Muneer,T. (2009). Integrated collector storage solar water heater: Temperature stratification. Applied Energy 86 (2009) 1465–1469

Gerstmann, J. & Griffith, P. (1967). Laminar Film Condensation on the Underside of Horizontal and Inclined Surfaces. International Journal of Heat and Mass Transfer 10 (1967) 567-80.

Go, D. & Sen, M. (2010). Thermal Rectification Using Bulk Materials. ASME Journal of Heat Transfer 132 (12) 124502

Good, C., Andresen, I., Hestnes, A. (2015). Solar energy for net zero energy buildings – A comparison between solar thermal, PV and photovoltaic–thermal (PV/T) systems. Solar Energy 122, 986–96

He, W., Hong, X., Zhao, X., Zhang, X., Shen, J., Ji, J. (2015). Operational performance of a novel heat pump assisted solar façade loop-heat-pipe water heating system. Applied Energy 146 (2015) 371–38

Hu, Z., He, W., Ji, J., Hu, D., Shen, Z. (2017). Comparative study on the annual performance of three types of building integrated photovoltaic (BIPV) Trombe wall system. Applied Energy 194 (2017) 81-93

Idris, Y., Mae, M. (2017). Anti-insulation mitigation by altering the envelope layers' configuration. Energy and Buildings 141 (2017) 186–204

IEA – International Energy Agency (2018). Key World Energy Statistics 2018. Paris, France: IEA.

IEA/UN - International Energy Agency and the United Nations Environment Programme (2018). 2018 Global Status Report: towards a zero-emission, efficient and resilient buildings and construction sector. Paris, France: IEA for the Global Alliance for Buildings and Construction (GlobalABC). ISBN: 978-92-807-3729-5.

Inan, T., Basaran, T. (2019). Experimental and numerical investigation of forced convection in a double skin façade by using nodal network approach for Istanbul. Solar Energy 183 (2019) 441-452

Jin, Q., Favoino, F., Overend, M. (2017). Design and control optimisation of adaptive insulation systems for office buildings. Part 2: A parametric study for a temperate climate. Energy 127 (2017) 634-649

Kilaire, A., Stacey, M. (2017). Design of a prefabricated passive and active double skin façade system for UK offices. Journal of Building Engineering 12 (2017) 161-170

Kimber, M., Clark, W., Schaefer, L. (2014). Conceptual analysis and design of a partitioned multifunctional smart Insulation. Applied Energy 114 (2014) 310–319

Koenders, S., Loonen, R., Hensen, J. (2018). Investigating the potential of a closed-loop dynamic insulation system for opaque building elements. Energy & Buildings 173 (2018) 409–427

Kolodziej, A. and Jaroszynski, M. (1997). Performance of liquid convective diodes. Solar Energy 61 (5) 321–326

Li, S., Zhang, Y., Zhang, K., Li, X., Li, Y., Zhang, X. (2013). Study on performance of storage tanks in solar water heater system in charge and discharge progress (SHC 2013, International Conference on Solar Heating and Cooling for Buildings and Industry). Energy Procedia 48 (2014) 384–393 doi: 10.1016/j.egypro.2014.02.045

Li, X., Lin, A., Young, C., Dai, Y., Wang, C. (2019). Energetic and economic evaluation of hybrid solar energy systems in a residential net-zero energy building. Applied Energy 254 (2019) 113709

Masoso, O., Grobler, L. (2008). A new and innovative look at anti-insulation behaviour in building energy consumption. Energy and Buildings 40 (2008) 1889–1894

Mehdaoui, F., Hazami, M., Messaouda, A., Guizani, A. (2019). Performance analysis of two types of Solar Heating Systems used in buildings under typical North-African climate (Tunisia). Applied Thermal Engineering (AIP) https://doi.org/10.1016/j.applthermaleng.2019.114203

Menyhart, K., Krarti, M. (2017). Potential energy savings from deployment of Dynamic Insulation Materials for US residential buildings. Building and Environment 114 (2017) 203-218.

Mohamad, A. (1997). Integrated Solar Collector-Storage Tank System with Thermal Diode. Solar Energy 61 (3) 211-218

Muhumuza, R., Zacharopoulos, A., Mondol, J., Smyth, M. (2019a). Experimental study of heat retention performance of thermal diode Integrated Collector Storage Solar Water Heater (ICSSWH) configurations. Sustainable Energy Technologies and Assessments 34 (2019) 214–219

Muhumuza, R., Zacharopoulos, A., Mondol, J., Smyth, M., Pugsley, A., Giuzio, G., Kurmis, D. (2019b). Experimental investigation of horizontally operating thermal diode solar water heaters with differing absorber materials under simulated conditions. Renewable Energy, Volume 138, August 2019, Pages 1051-1064

O'Hegarty, R., Kinnane, O., McCormack, S. (2014). A Case for façade located solar thermal collectors. (International Conference on Solar Heating and Cooling for Buildings and Industry, SHC 2014). Energy Procedia 70 (2015) 103–110 doi: 10.1016/j.egypro.2015.02.104

Pei, W., Zhang, M., Li, S., Lai, Y., Jin, L., Zhai, W., Yu, F., Lu, J. (2017). Geotemperature control performance of two-phase closed thermosyphons in the shady and sunny slopes of an embankment in a permafrost region. Applied Thermal Engineering 112 (2017) 986–998

Pflug, T., Nestle, N., Kuhn, T., Siroux, M., Maurer, C. (2018). Modelling of facade elements with switchable U-value. Energy & Buildings 164 (2018) 1–13

Peterson, P. (1996). Theoretical basis for the Uchida correlation for condensation in reactor containments. Nuclear Engineering and Design 162 (1996) 301-306.

Poppi, S., Bales, C., Haller, M., Heinz, A. (2016). Influence of boundary conditions and component size on electricity demand in solar thermal and heat pump combisystems. Applied Energy 162 (2016) 1062–73

Pugsley, A., Mondol, J., Smyth, M., Zacharopoulos, A. & Di Mattia, L. (2016). Experimental characterisation of a flat panel integrated collector-storage solar water heater featuring a photovoltaic absorber and a planar liquid-vapour thermal diode. Proceedings of 11th ISES EuroSun Conference: Palma (Mallorca), Spain from 11 to 14 October 2016. Martinez, V. & Gonzalez, J. (eds.).

Pugsley, A. (2017). Theoretical and experimental analysis of a novel flat photovoltaic-thermal solar water heater with integrated energy storage via a planar liquid-vapour thermal diode. Ulster University PhD Thesis (uk.bl.ethos.713462) published July 2017.

Pugsley, A., Zacharopoulos, A., Mondol, J., Smyth, M. (2019). Theoretical and experimental analysis of a horizontal 1 Planar Liquid-Vapour Thermal Diode (PLVTD). International Journal of Heat and Mass Transfer 144 (2019) 11866

Qu, M., Chen, J., Nie, L., Li, F., Yu, Q., Wang, T. (2016). Experimental study on the operating characteristics of a novel photovoltaic/thermal integrated dual-source heat pump water heating system. Applied Thermal Engineering 94, 819–26

Quinlan, P. (2010). The Development of a Novel Integrated Collector Storage Solar Water Heater (ICSSWH) Using Phase Change Materials and Partial Evacuation. PhD Thesis, University of Ulster.

Reay, D., Kew, P., McGlen, R. (2014). Heat Pipes - Theory, Design and Applications (6th edition). London, UK: Butterworth-Heinemann (Elsevier). ISBN: 0080982794

Rhee, J., Campbell, A. Mariadass, A. and Morhous, B. (2010). Temperature stratification from thermal diodes in solar hot water storage tank. Solar Energy 84 (2010) 507–511

Roberts, N. & Walker, D. (2011). A review of thermal rectification observations and models in solid materials. International Journal of Thermal Sciences 50 (2011) 648-62.

Rupp, S., Krarti, M. (2019). Analysis Of Multi-Step Control Strategies For Dynamic Insulation Systems. Energy & Buildings (2019 AIP) doi.org/10.1016/j.enbuild.2019.109459

Schmidt, F., Henderson, R. and Wolgemuth, C. (1993). Introduction to thermal sciences – Thermodynamics, Fluid dynamics, Heat transfer (2nd ed.). London: John Wiley & Sons.

Singh, R., Lazarus, I., and Souliotis, M. (2016). Recent developments in integrated collector storage (ICS) solar water heaters: A review. Renewable & Sustainable Energy Reviews 54, 270-98

Smyth, M., Eames, P. and Norton, B. (1999). A comparative performance rating for an integrated solar collector/storage vessel with inner sleeves to increase heat retention. Solar Energy 66 (4) 291–303.

Smyth, M., Eames, P. and Norton, B. (2006). Integrated Collector Storage Solar Water Heaters. Renewable and Sustainable Energy Review 10 (6) 503-538

Smyth, M. (2015a). A solar water heater. Patent WO2010052010 held by Ulster University.

Smyth, M., Besheer, A., Zacharopoulos, A., Mondol, J., Pugsley, A., Novaes, M. (2015b). Experimental evaluation of a Hybrid Photovoltaic/Solar Thermal (HyPV/T) Façade Module. Proceedings EURO ELECS Conference 21-23 July 2015, Guimarães, Portugal.

Smyth, M., Quinlan, P., Mondol, J., Zacharopoulos, A., McLarnon, D., Pugsley, A. (2017). The evolutionary thermal performance & development of a novel thermal diode pre-heat solar water heater under simulated heat flux conditions. Renewable Energy 113 (2017) 1160-1167

Smyth, M., Quinlan, P., Mondol, J., Zacharopoulos, A., McLarnon, D., Pugsley, A. (2018). The experimental evaluation and improvements of a novel thermal diode pre-heat solar water heater under simulated solar conditions. Renewable Energy 121 (2018) 116-122

Smyth, M., Pugsley, A., Hanna, G., Zacharopoulos, A., Besheer, A., Savvides, A. (2019). Experimental performance characterisation of a Hybrid Photovoltaic/Solar Thermal Façade module compared to a flat Integrated Collector Storage Solar Water Heater module. Renewable Energy 137 (2019) 137-143

Sopian, K., Syahri, M., Abdullah, S., Othman, M.,Yatim, B. (2004). Performance of a non-metallic unglazed solar water heater with integrated storage system. Renewable Energy 29 (2004) 1421–1430

Souliotis, M., Quinlan, P., Smyth, M., Tripanagnostopoulos, Y., Zacharopoulos, A., Ramirez, M., Yianoulis, P. (2011). Heat retaining integrated collector storage solar water heater with asymmetric CPC reflector. Solar Energy 85 (2011) 2474–87

Souliotis, M., Papaefthimiou, S., Caouris, Y., Zacharopoulos, A., Quinlan, P., Smyth, M. (2017). Integrated collector storage solar water heater under partial vacuum. Energy 139 (2017) 991-1002

Stazi, F., Vegliò, A., Perna, C., Munafò, P. (2012). Retrofitting using a dynamic envelope to ensure thermal comfort, energy savings and low environmental impact in Mediterranean climates. Energy and Buildings 54 (2012) 350–362.

Stein, R., Cho, D., Lambert, G. (1985). Condensation on the underside of a horizontal surface in a closed vessel (CONF-850810-27). Argonne, Illinois, USA: Argonne National Laboratory. Available at: www.osti.gov/scitech/biblio/5207060

Traipattanakul, B., Tso, C., Chao, C. (2019). A phase-change thermal diode using electrostatic-induced coalescing jumping droplets. International Journal of Heat and Mass Transfer 135 (2019) 294–304

Tripanagnostopoulos, Y. and Souliotis, M. (2006). ICS Solar Systems with Two Water Tanks. Renewable Energy 29 (1) 13-38

Tsilingiris, P. (2008). Thermophysical and transport properties of humid air at temperature range between 0 and 100°C. Energy Conversion and Management 49 (2008) 1098–1110.

Twidell, J. & Weir, T. (2006). Renewable Energy Resources (2nd ed.) London: Taylor Francis. ISBN13:9-78-0-419-25330-3

Varga, S., Oliveira, A., Afonso, C. (2002). Characterisation of thermal diode panels for use in the cooling season in buildings. Energy and Buildings 34 (2002) 227-235

Villeneuve, T., Boudreau, M., Dumas, G. (2017). The thermal diode and insulating potentials of a vertical stack of parallelogrammic air-filled enclosures. International Journal of Heat and Mass Transfer 108 (2017) 2060–2071

Wong, M., Traipattanakul, B., Tso, C., Chao, C., Qiu, H. (2019). Experimental and theoretical study of a water-vapor chamber thermal diode. International Journal of Heat and Mass Transfer 138 (2019) 173–183

Yu, B., Li, N., Ji, J. (2019). Performance analysis of a purified Trombe wall with ventilation blinds based on photo-thermal driven purification. Applied Energy 255 (2019) 113846.

Zaitsev, D., Kabov, O. and Evseev, A. (2003). Measurement of locally heated liquid film thickness by a double-fiber optical probe. Experiments in Fluids 34 (6) 48–754.

Zhou, D., Gambaryan-Roisman, T. and Stephan, P. (2009). Measurement of water falling film thickness to flat plate using confocal chromatic sensoring technique. Experimental Thermal and Fluid Science 33, 273–283.

Ziapour, B., Palideh, V., Mohammadnia, A. (2014). Study of an improved integrated collector-storage solar water heater combined with the photovoltaic cells. Energy Conversion and Management 86 (2014) 587–594.

Appendix 1

Equations for evaluating vapour mass flow thermal resistance (R_{ec}) when the PLVTD contains a mixture of working fluid and non-condensable gases

It is widely recognised that non-condensable gases reduce rates of liquid-vapour-liquid heat transfer and the effect was noted by Boreyko & Chen (2013) during their thermal diode experiments. Cengel & Boles (2006) suggests that the non-condensable gases form a barrier layer near the condenser surface which imposes a resistance to the flow of vapour between the evaporator and the condenser. The resistance is highest when the vapour velocity is low and the non-condensable gas concentration is high. Stein et al. (1985) attempted to model the effect for condensation on the underside of a horizontal plate by considering mass diffusivity within the air-water gas mixture using a Sherwood number mass transfer approach (analogous to the Nusselt number heat transfer approach). A similar approach adopted by Peterson (1996) described the effect on a vertical condenser using its height as the characteristic dimension (L=z). Both models represent gas mixture (water vapour and non-condensable gas) as a barrier layer which covers the condenser surface. Water vapour produced at the evaporator must pass through the barrier layer prior to condensing.

Both the Peterson (1996) and Stein et al. (1985) models define the Rayleigh number according to Equation A1 in terms of the difference (ρ_{X2}-ρ_{X1}) between the density of the gas mixture near the condenser surface and the density of the gas mixture near the evaporator surface. The terms used in Equation A1 are the dimensionless Schmidt number ($\mu/\rho D$) which is the mass transfer equivalent of the Prandtl number, mixture densities (ρ_X), gravitational acceleration (g), characteristic dimension (L=x), average mixture viscosity (μ_X), and mixture mass diffusivity (D_X). Peterson (1996) suggests that the mixture densities can be evaluated using Equations A2 and A3 where the terms $\dot{\mathcal{M}}_v$ and $\dot{\mathcal{M}}_{ncg}$ are the respective molecular masses of water and the non-condensable gas. The terms X_{ncg1} and X_{ncg2} represent the mole fractions of non-condensable gas present in the mixture at the respective evaporator (T_1) and condenser (T_2) temperatures. The ambient temperature (T_a) is used as a convenient point of reference for determining the hypothetical saturated water vapour density (ρ_{LvXa}) which would occur at a total pressure ($P_{Xa}=P_{Lva}+P_{ncga}$) equal to the sum of the saturated water vapour and non-condensable gas partial pressures at the ambient temperature (T_a). The reference temperature T_{ref}=273.16 K is the freezing point of water in Kelvin. Stein et al. (1985) suggest that the mass diffusivity of a mixture of air and water vapour can be estimated with sufficient reliability using Equation A4 where the constants are given as $D_{ref}=2.2\times10^{-5}$ m^2/s and P_{atm}=100 kPa.

$$Ra^* = \left(\frac{\rho_X g L^3(\rho_{X2}-\rho_{X1})}{{\mu_X}^2}\right)\left(\frac{\mu_X}{\rho_X D_X}\right) = \frac{gL^3(\rho_{X2}-\rho_{X1})}{\mu_X D_X} \qquad \textbf{Equation A1}$$

$$\rho_{X1} = \frac{\rho_{LvXa}(T_a+T_{ref})}{(T_1+T_{ref})}\left[X_{ncg1}\frac{\dot{\mathcal{M}}_{ncg}}{\dot{\mathcal{M}}_v}\right] \qquad \textbf{Equation A2}$$

$$\rho_{X2} = \frac{\rho_{LvXa}(T_a+T_{ref})}{(T_2+T_{ref})}\left[1+X_{ncg2}\left(\frac{\dot{\mathcal{M}}_{ncg}}{\dot{\mathcal{M}}_v}-1\right)\right] \qquad \textbf{Equation A3}$$

$$D_X = D_{ref}\left(\frac{P_{atm}}{P_X}\right)\left(\frac{T_{12}+T_{ref}}{T_{ref}}\right)^{1.75} \qquad \textbf{Equation A4}$$

The thermal conductivity of the gas mixture (working fluid vapour plus non-condensable gases) involved in the liquid-vapour-liquid heat transfer process (k*) is defined according to Equation A5 where ϑ_X, D_x and k_x respectively are the thermal diffusivity, mass diffusivity, and thermal conductivities of the gas mixture and k_{XLv} is the latent heat thermal conductivity of the vapour defined by Equation A6 which is similar to Equation 18 with the addition of a term (ϕ_X calculated using Equation A7) describing the mole fraction ratio of the gas mixture.

$$k_X^* = k_X\left(\frac{D_X}{\vartheta_X}\right)^{1/3} + k_{XLv} \qquad \textbf{Equation A5}$$

$$k_{XLv} = \frac{{h_{Lv}}^2 P_X {\dot{\mathcal{M}}_v}^2 D_X}{\phi_X \dot{\mathcal{R}}^2 {T_{12}}^3} \qquad \text{Equation A6}$$

$$\phi_X = -1\left(\frac{\ln[(1-X_{ncg1})/(1-X_{ncg2})]}{\ln(X_{ncg1}/X_{ncg2})}\right) \qquad \text{Equation A7}$$

Numbers used in subscripts in Equations A1 to A7 denote whether properties should be evaluated at the evaporator (T_1) or condenser (T_2) temperature. Properties with no numbers in the subscript should be evaluated at the average operating temperature $T_{12}=(T_1+T_2)/2$. The subscripts v, ncg and X respectively refer to water vapour, non-condensable gas and the mixture of two fluids. Gas mixture properties ρ_x, μ_x, k_x, ϑ_X, X_{ncg} and X_v can be determined using Wilke's rule and other expressions presented by Tsilingiris (2008), which are reproduced in Table A1.

Table A1 – Equations for determining the properties of gas mixtures

Property	*Expression*
Density (ρ_X)	$\rho_X = \frac{P_{Lv} + P_{ncg}}{\dot{\mathcal{R}}(T + T_0)} \dot{\mathcal{M}}_{ncg} \left[1 - X_v \left(1 - \frac{\dot{\mathcal{M}}_v}{\dot{\mathcal{M}}_{ncg}}\right)\right]$
Dynamic viscosity (μ_X)	$\mu_X = \frac{(1-X_v)\mu_{ncg}}{(1-X_v)+X_v\Phi_{ncg-v}} + \frac{X_v \mu_v}{X_v+(1-X_v)\Phi_{v-ncg}}$
Thermal conductivity (k_X)	$k_X = \frac{(1-X_v)k_{ncg}}{(1-X_v)+X_v\Phi_{ncg-v}} + \frac{X_v k_v}{X_v+(1-X_v)\Phi_{v-ncg}}$
Specific heat capacity ($c_{p,X}$)	$c_{p,X} = c_{p,v} X_v \left(\frac{\dot{\mathcal{M}}_v}{\dot{\mathcal{M}}_v + \dot{\mathcal{M}}_{ncg}}\right) + c_{p,ncg} X_{ncg} \left(\frac{\dot{\mathcal{M}}_{ncg}}{\dot{\mathcal{M}}_v + \dot{\mathcal{M}}_{ncg}}\right)$
Ratio of mass diffusivity (D_X) to thermal diffusivity (ϑ_X)	$\frac{Pr_X}{Sc_X} = \frac{D_X}{\vartheta_X} = \frac{D_X \rho_X c_{p,X}}{k_X}$
Non-condensable gas mole fraction (X_{ncg})	$X_{ncg} = \frac{P_{ncg}}{P_{Lv}+P_{ncg}}$
Water vapour mole fraction (X_v)	$X_v = \frac{P_{Lv}}{P_{Lv}+P_{ncg}}$
Wilke's coefficients for non-condensable gas mixed with water vapour (Φ_{ncg-v} and Φ_{v-ncg})	$\Phi_{ncg-v} = 0.354 \left(1 + \frac{\dot{\mathcal{M}}_{ncg}}{\dot{\mathcal{M}}_v}\right)^{-0.5} \left[1 + \left(\frac{\mu_{ncg}}{\mu_v}\right)^{0.5} \left(\frac{\dot{\mathcal{M}}_v}{\dot{\mathcal{M}}_{ncg}}\right)^{0.25}\right]^2$
	$\Phi_{v-ncg} = 0.354 \left(1 + \frac{\dot{\mathcal{M}}_v}{\dot{\mathcal{M}}_{ncg}}\right)^{-0.5} \left[1 + \left(\frac{\mu_v}{\mu_{ncg}}\right)^{0.5} \left(\frac{\dot{\mathcal{M}}_{ncg}}{\dot{\mathcal{M}}_v}\right)^{0.25}\right]^2$